The spatiotemporal dynamics of human focal seizures

Jyun-you Liou

Submitted in partial fulfillment of the
requirements for the degree of
Doctor of Philosophy
under the Executive Committee
of the Graduate School of Arts and Sciences

COLUMBIA UNIVERSITY

2017

ABSTRACT

The spatiotemporal dynamics of human focal seizures

Jyun-you Liou

Spontaneous human focal seizures can present with a plethora of behavioral manifestations that vary according to the affected cortical regions; however, several key features have been consistently observed. During my doctoral studies, I applied both theoretical and experimental methods to study mechanisms underpinning these consistently seen dynamics. I first analyzed human intracranial EEG recordings, describing statistical methods for measuring their electrophysiological signatures. I next proposed several neurophysiological hypotheses that could explain seizure dynamics and verified them in rodent seizure models. Finally, a computational model was developed, successfully explaining how the complex spatiotemporal evolution of focal seizures emerges from simple neurophysiological principles.

In Chapter 1, the long-standing behavioral manifestations and the most up-to-date electrophysiology findings are reviewed. This section details the inspiration for the studies reported in the subsequent chapters.

In Chapter 2, I describe several statistical methods for estimating traveling wave velocities. I show most ictal discharges can be described as traveling waves whose velocities contain rich information about the stages of seizure evolution. I compare performance of various statistical methods and propose a robust approach to boost the quality of each method's estimation results.

In Chapter 3, I show how inhibition modulates seizure propagation patterns. Surround inhibition spatially restrains focal seizures and masks excitatory projections of ictal activities. When compromised, two patterns of seizure propagation emerge according to the position of inhibition defects relative to the ictal focus. I show that two distant ictal foci can communicate via physiological connectivity without any chronic rewiring processes – confirming the existence of long-range propagation pathways that could lead to epileptic network formation.

In Chapter 4, I show that thalamic inputs might be necessary for interictal epileptiform discharges (IEDs). The relative positions between IEDs and ictal foci indicate that surround inhibition, shown in the previous chapter, can be exhausted by repetitive exposure to ictal projections.

In Chapter 5, I propose a neural network model that can explain both long-standing behavioral observations of seizures and account for the most up-to-date electrophysiological recordings of spontaneous human focal seizures. The model relies on few assumptions, all of which are proved or supported in earlier chapters of this thesis. The model explains phasic evolution of seizure dynamics – how the commonly observed patterns arise from simple neurophysiological principles, as well as seizure onset subtypes, traveling wave directions and speeds. The model also predicts how spontaneous seizures might arise from synaptic plasticity. The chapter ends with a discussion of the model's implications and future work.

The thesis is organized in a way that each chapter can be read independently, with Chapter 5 summarizing the central theory spanning the whole study. Each chapter is also tightly linked to a clinically relevant question. In sum, the dissertation's goal is to provide an in-principle understanding of focal seizure dynamics. With rapid advancement of clinical and experimental tools, I believe this work provides a roadmap for future therapies for epilepsy patients.

TABLE OF CONTENTS

List of Charts, Graphs, Illustrations

Chapter 5

Chapter 1

Behavioral and electrophysiological findings concerning focal seizures

1.1 Clinical observations of focal seizures

Epilepsy is a chronic disorder that predisposes patients to epileptic seizures, which are transient occurrences of signs and/or symptoms due to abnormal excessive or synchronous neuronal activity (Fisher, Acevedo et al. 2014). Epilepsy imposes a high disease burden, affecting 0.5 to 1% of the U.S. population (Banerjee, Filippi et al. 2009). Despite of years of research, approximately one third of epilepsy patients are pharmacoresistant, i.e. they continue to experience seizures despite medical treatment (Berg 2009). Recurrent seizures are accompanied by extensive neurologic, psychiatric, and medical comorbidities, including early death. The annual mortality rate of patients with seizure disorders is three times higher than the mortality rate of the general population (Tsai 2005).

Focal seizures, defined as seizures starting in one area or side of the brain (Fisher, Cross et al. 2017), can present with a plethora of behavioral manifestations according to the affected brain regions. Descriptions of focal seizures' clinical presentations date back to ancient Mesopotamia. One source from 1000 BC Babylonian literature states – 'while the patient is sitting down, his eye moves to the side, a lip puckers, saliva flows from his mouth, and his hand, leg and trunk on the left side jerk like a newly-slaughtered sheep.' The ancient Chinese (Huang Di Nei Jing – Su Wen) also described evolution of focal seizures – 'it starts with rigid contraction, bending the patient's spine vigorously, later evolves into muscle and tendon twitches.' (Ni 1995). This ancient literature vividly describes clinical presentations of focal

seizures involving motor areas. It highlights seizure (ictal) activity gradually recruiting adjacent cortical regions, as well as transitioning from persistent (tonic) contraction of muscles into repetitive clonic muscle movements. In modern medicine, perhaps the most famous description came from Dr. John Hughlings Jackson, a 19th century English neurologist (York and Steinberg 2011). Now termed 'Jacksonian march', this manifestation of focal seizures progresses in a predictable pattern, from twitching, a tingling sensation, or weakness in a finger, a toe, or the corner of the mouth, then gradually propagates to the entire hand, foot or facial muscles in several seconds to minutes (Worthington 2007, York and Steinberg 2011, Extercatte, de Haan et al. 2015).

As adjacent cortical regions are progressively recruited, repetitive jerky (clonic) movements with a characteristic rhythmic fast-slow pattern can be observed. This commonly seen evolution pattern in motor seizures – stiffening of the corresponding body parts occurs first followed by periodic jerking – is termed the tonic-to-clonic transition (Mattson, Cramer et al. 1985). Seizures may further propagate to affect subcortical regions, resulting in loss of awareness (Motelow, Li et al. 2015). In some cases, the activity may even propagate further, influencing the contralateral hemisphere; this is termed secondary generalization (Fisher, Cross et al. 2017). Secondary generalization is a significant hazard to patient safety (Yoo, Farooque et al. 2014), as generalized seizures have been shown to be a significant risk factor for sudden unexpected death in epilepsy (SUDEP) (Hesdorffer, Tomson et al. 2012).

As seizures approach termination, the frequency of clonic movements typically slows down (Extercatte, de Haan et al. 2015). At seizure termination, the clonic jerking stops abruptly, corresponding with a cessation of the correlating electroencephalogram (EEG) discharges

simultaneously across the entire affected brain region. Various post-ictal abnormalities can ensue, depending on the severity, duration, regions of seizure invasion, etc. A well-known example of a post-ictal feature is 'Todd's paralysis' (or Todd's paresis), originally described by Irish neurologist Dr. Robert Bentley Todd, in which there is a transient focal weakness contralateral to the side of seizure origin. Similar impairments may occur in language function, vision, memory, general mental status, or other higher cortical functions (Pearce 1994, Gallmetzer, Leutmezer et al. 2004). Mood disorders, anxiety, and psychosis are also common postictal features. Other postictal effects include headache, migraine, cardiac arrhythmias, and disordered breathing. In extreme cases, death may occur due to postictal cardiorespiratory failure (Ryvlin, Nashef et al. 2013), despite resuscitation efforts.

While the characteristic dynamics of focal seizures – slow propagation, tonic-to-clonic transitions, and terminal slowing – are observable in certain seizure types, they are present also in seizures affecting non-motor areas (Devinsky 2004), and are more readily detected by EEGs (Anziska and Cracco 1977, Blumenfeld, Rivera et al. 2004, Kramer, Truccolo et al. 2012). Focal seizures have a spatially restricted EEG onset, although the exact size of initial involvement have been subject to vigorous debates (Smith and Schevon 2016). Propagation of epileptiform activity typically follows topological orders, although rapid propagation or appearance of wide-area onsets has led some to theorize that seizure onset may sometimes be distributed over a broad area (Kramer, Kolaczyk et al. 2008, Khambhati, Davis et al. 2016, Smith and Schevon 2016). Seizure EEGs evolve in frequency, amplitude, waveforms, etc. For example, low-voltage fast activity (LVFA), the most common EEG pattern during focal seizure onset (Perucca, Dubeau et al. 2014), typically evolves into periodic synchronous discharges in a few seconds. The evolution from asynchronous, chaotic electrical signals into synchronized patterns carries

3

similarity to behavioral tonic-to-clonic transitions. As seizures approach termination, dynamics

of epileptiform discharges undergo continuous change as inter-discharge intervals gradually

prolong (Anziska and Cracco 1977, Blumenfeld, Rivera et al. 2004, Kramer, Truccolo et al.

2012). Various EEG anomalies, ranging from slow delta waves to suppression patterns, can also

be seen during post-ictal periods (So and Blume 2010, Lamberts, Gaitatzis et al. 2013), which

may correspond with neurological symptoms and/or signs patients demonstrate immediately after

seizures.

1.2 Recent intraparenchymal multielectrode array recordings

Until the early 2000s, electrophysiology studies done in epilepsy patients mostly relied

on LFPs and their derived signals, including surface EEG, electrocorticography (ECoG), depth

electrodes (Noachtar and Remi 2009), and magnetoencephalography (MEG) (Stefan, Schneider

et al. 1990). LFPs encode rich information (Einevoll, Kayser et al. 2013); however, using them

to infer neuronal activity during seizures can be challenging. This is because LFPs are

dominated by synaptic potentials (Einevoll, Kayser et al. 2013, Mazzoni, Linden et al. 2015)

instead of the action potential signal itself. Synchronized neuronal firing can create widespread

LFPs via synaptic projections and large amplitude fluctuations by constructive interference,

which can mask local circuit signals and may be misleading. Also, EEGs only provide a limited

partial view of the activity of a whole neuronal population, reflecting radial dipole signals from

apical dendrites of pyramidal cells in upper cortical layers (Einevoll, Kayser et al. 2013). Lack

of methods that allow large-scale, direct observation of neuronal spikes limits our understanding

of seizure dynamics.

In recent years, the development of high-density, intra-cortical multi-electrode arrays has opened the possibility of directly observing spiking activity of hundreds of neurons during spontaneous human seizures (Waziri, Schevon et al. 2009, Schevon, Weiss et al. 2012). These unprecedented high-resolution recordings revealed neuronal dynamics that corresponded to the aforementioned seizure evolution features, summarized in Table 1.1 at the end of this chapter. Seizures appeared to start from a millimeter-scale cortical region, within which neurons fired intensely and asynchronously (Schevon, Weiss et al. 2012). The seizing region slowly expanded at measured speeds of ≤ 1 mm per second. This speed corresponds with the rate of progression of a Jacksonian march through the motor homunculus. The seizing region further expanded as the adjacent neurons were gradually recruited, forming a propagating, narrow (less than 1 mm) tonic-firing band (ictal wavefront). Inside the seizing region, the initially tonic-firing neurons gradually synchronized, and then transitioned into repetitive bursting, reminiscent of the longstanding tonic-to-clonic transition observed clinically. Importantly, the clear demarcation between the seizing region (ictal core) and its adjacency (ictal penumbra) was significantly blurred in LFP frequency bands, emphasizing the value of direct neuronal observation during seizures (Schevon, Weiss et al. 2012) (Figure 1.1).

Figure 1.1 Subdomains of ictal zones
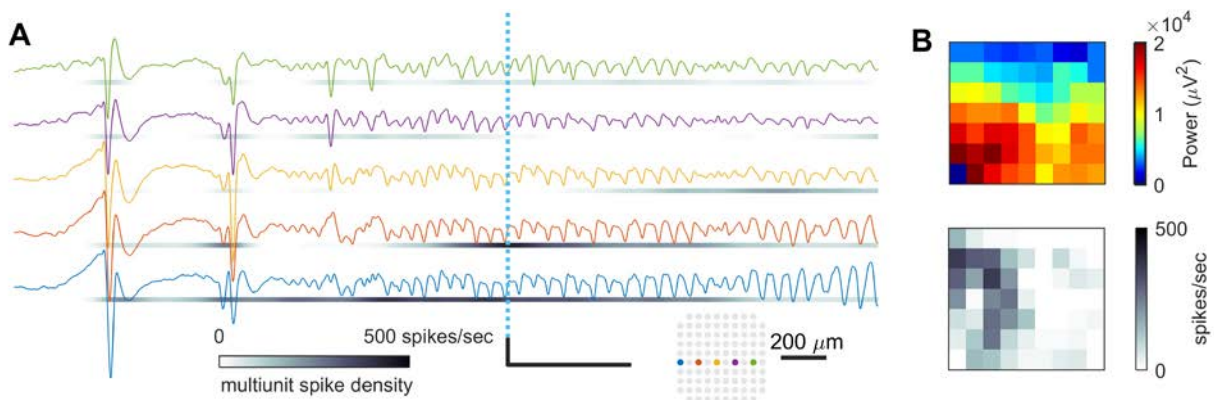
A) Recording of a seizure onset. Although epileptic LFP fluctuations can be observed in all five electrodes, only the left electrodes show intense multiunit firing. The right electrodes remain relatively silent (gray bars). Scale bars: 0.5 seconds, 0.5 mV. Multiunit spiking rate (density) was estimated by a 0.05-second wide Gaussian kernel. Colors of the LFP traces represented where they were recorded from the multielectrode array (inset map).

B) Distribution of LFP power and multiunit spiking rates at the time indicated by the vertical dotted line in Panel A. Contrast of LFP and multiunit spiking rate maps shows the distinction between the ictal core and penumbra. High LFP power can be observed across the array; however, only the left part (ictal core) shows significant multiunit firing. LFP power was calculated as signal variance within a 0.1-second window.

Within the ictal core, neuronal bursts arose sequentially in space, behaving like traveling waves (Smith, Liou et al. 2016, Liou, Smith et al. 2017). Our group provided evidence that they arise from the edge of the seizure territory, travelling backward into the ictal core with average speed 20 to 50 cm per second (Smith, Liou et al. 2016). Pre-termination neuronal dynamics also mimic large-scale patient behavior, showing progressively prolonged inter-burst intervals and progressive desynchronization (Kramer, Truccolo et al. 2012, Smith, Liou et al. 2016).

1.3 An in-principle approach toward understanding seizure dynamics

Is there a theory that can explain why focal seizures, despite their heterogeneity of clinical semiologies, etiologies, and origination sites, consistently demonstrate the same key dynamic elements? Given that they have been observed across a wide range of neocortical regions and etiologies, I believe the key features may originate from common neurophysiological principles that organize cortical circuits and control their excitability.
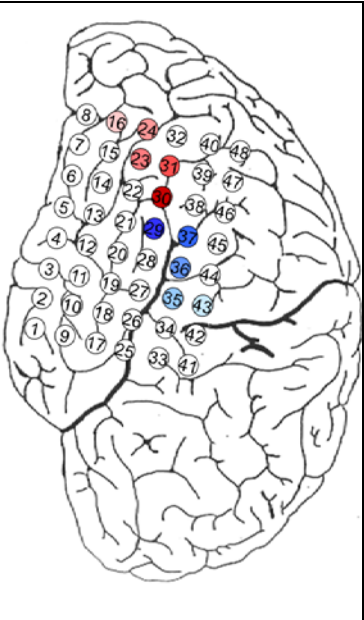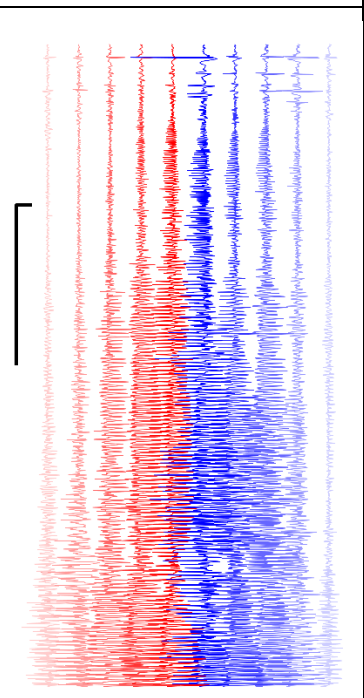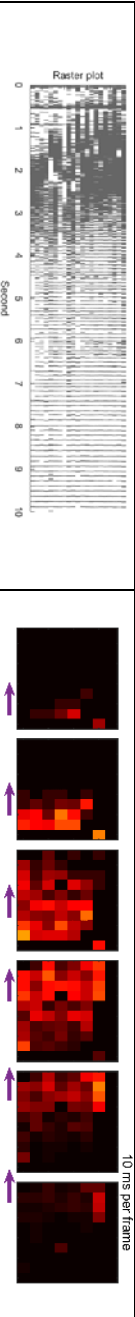
In my thesis research, I aim to provide a principled, physiological understanding of focal seizure dynamics, basing on the following hypotheses:
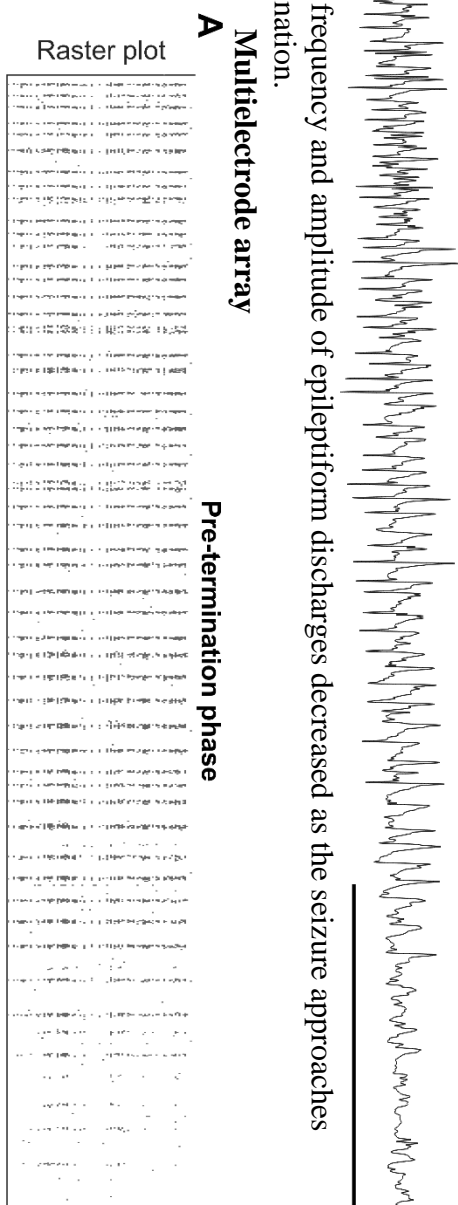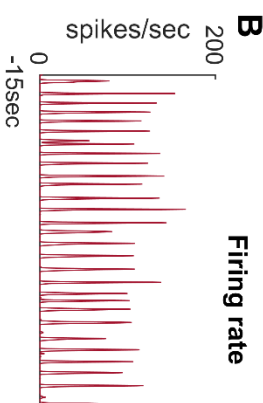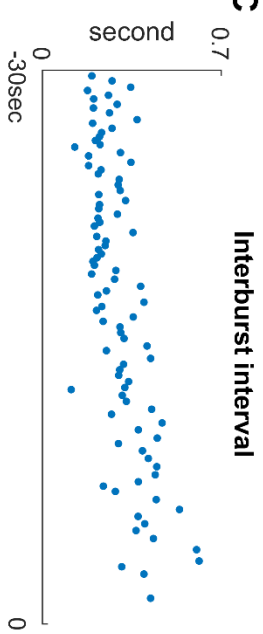
1. **Ictal core**. Neocortical focal seizure starts with a highly localized group of neurons firing excessively above physiological range.

2. **Center-surround effect**. Through recurrent excitation, neurons within ictal cores mutually enhance each other. However, in adjacent areas (ictal penumbra), massive synaptic barrages coming from the ictal core produce a net inhibitory effect on penumbral circuit activity.

3. **Exhaustion of inhibition**. Prolonged exposure to synaptic barrages coming from the ictal core compromises the inhibitory response in the ictal penumbra.

4. **Adaptation**. Intensive neuronal firing during seizures provokes multiple mechanisms to reduce individual neuronal and overall cortical excitability over various time scales.

This thesis is organized so that each chapter can be read independently, with Chapter 5 summarizing the central theory spanning the whole study. Each chapter is also tightly associated with a clinically relevant question. In the next chapter, I will start with an in-depth, statistical analysis of traveling wave velocities. In Chapter 3, I will demonstrate the center-surround effect in a rodent acute seizure model. The exhaustion of inhibition hypothesis will be supported in Chapter 4. Together with previous works (hypothesis 1 & 4) (Schevon, Weiss et al. 2012), in the final chapter, I will present a theory explaining the longstanding mystery of focal seizure dynamics.

Table 1.1 Comparison of clinical and electrophysiological findings of seizure dynamics.

Clinical observation	Electrophysiology
Gradual recruitment of new territory (e.g. Jacksonian march). - The abnormal motor/sensory experience progresses in a predictable pattern that follows cortical topology, e.g. from twitching of facial muscles at mouth angle, then marches, within one or two minutes, to neck, the ipsilateral hand, trunk, and finally the ipsilateral leg.	• **Electrocorticography** ECoG shows topologically sequential emergence of epileptiform discharges. Color indicates which subdural electrode the traces were recorded from. Right panel scale bars: 10 seconds & 0.5 mV • **Multielectrode array** Gradual expansion of seizure territory (< 1mm/sec).
Tonic-clonic transition Seizures that involve primary motor cortex stiffen the corresponding body parts first. A few seconds later, the constantly contracting muscles begin to spasm and jerk periodically.	• **Electrocorticography** (scale bar: 5 seconds, 0.5 mV) Low voltage fast activity (LVFA) Evolves into periodic discharges • **Multielectrode array** Notice the tonic firing ictal wavefront (the right most).

Neurons demonstrated transition from tonic firing to recurrent bursts (left subpanel), forming traveling waves propagating backward to the center (right subpanel).

- **Electrocorticography** (scale bar: 10 seconds, 0.5 mV)

Both frequency and amplitude of epileptiform discharges decreased as the seizure approaches termination.

- **Multielectrode array**

Panel A: Raster plot at seizure termination, notice interburst intervals gradually prolonged.
Panel B & C: Summarized statistics from Panel A.

Termination slowing

During the clonic phase, muscles flex then relax rapidly at first, but the frequency of the spasms gradually declines until they cease altogether.

For a multimedia version of clinical observations, please see (Extercatte, de Haan et al. 2015).

Chapter 2

Multivariate regression methods for estimating velocity of ictal discharges from human microelectrode recordings

Abstract

Objective. Epileptiform discharges, an electrophysiological hallmark of seizures, can propagate across cortical tissue in a manner similar to traveling waves. Recent work has focused attention on the origination and propagation patterns of these discharges, yielding important clues to their source location and mechanism of travel. However, systematic studies of methods for measuring propagation are lacking.

Approach. We analyzed epileptiform discharges in microelectrode array recordings of human seizures. The array records multiunit activity and local field potentials at 400-micron spatial resolution, from a small cortical site free of obstructions. We evaluated several computationally efficient statistical methods for calculating traveling wave velocity, benchmarking them to analyses of associated neuronal burst firing.

Main results. Over 90% of discharges met statistical criteria for propagation across the sampled cortical territory. Detection rate, direction and speed estimates derived from a multiunit estimator were compared to four field potential-based estimators: negative peak, maximum descent, high gamma power, and cross-correlation. Interestingly, the methods that were computationally simplest and most efficient (negative peak and maximal descent) offer non-inferior results in predicting neuronal traveling wave velocities compared to the other two, more

complex methods. Moreover, the negative peak and maximal descent methods proved to be more robust against reduced spatial sampling challenges. Using least absolute deviation in place of least squares error minimized the impact of outliers, and reduced the discrepancies between local field potential-based and multiunit estimators.

Significance. Our findings suggest that ictal epileptiform discharges typically take the form of exceptionally strong, rapidly traveling waves, with propagation detectable across millimeter distances. The sequential activation of neurons in space can be inferred from clinically-observable EEG data, with a variety of straightforward computation methods available. This opens possibilities for systematic assessments of ictal discharge propagation in clinical and research settings.

2.1 Introduction

2.1.1 Synchronization or sequential activation? The traveling wave controversy

A long-recognized hallmark of seizures is the epileptiform discharge, i.e. a high amplitude, low-frequency waveform associated with intense, synchronized burst firing (Faeth, Walker et al. 1954, Niedermeyer and Lopes da Silva 1982, Wong and Prince 1990, Badier and Chauvel 1995, Baumgartner, Lindinger et al. 1995, Alarcon, Garcia Seoane et al. 1997, Ebersole and Pedley 2003, Smith 2005, Daube, Rubin et al. 2009). Neuronal firing recorded from *in vitro* seizure models is activated sequentially in space (Golomb and Amitai 1997, Pinto, Patrick et al. 2005, Trevelyan, Baldeweg et al. 2007). Clinical EEG and ECoG recordings have shown cross-site timing delays consistent with traveling waves (Chervin, Pierce et al. 1988, Emerson, Turner et al. 1995, Smith, Liou et al. 2016). However, the broad fields of epileptiform discharges have also been attributed to distributed network mechanisms or distant field effects (Ebersole 1994, Ebersole 2000, Vinck, Oostenveld et al. 2011, Buzsaki, Anastassiou et al. 2012).

Investigation of the traveling behavior of epileptiform discharges has recently garnered increased attention. However, there is no consensus on the reliability or robustness of the statistical methods available for this purpose. Similar analyses of bioelectrical signals, such as cardiac QRS complexes, have been described (Bayly, KenKnight et al. 1998, Kay and Gray 2005, Mazeh, Haines et al. 2013), but these signals differ from epileptiform discharges in that morphology is preserved, propagation pathways are less complex, and the point of origin is generally known. Epileptiform discharges must be analyzed as single-trial data with uncertain event timing, further increasing noise content (Rubino, Robbins et al. 2006). Timing of epileptiform discharges is most often defined by the negative peaks of local field potential (LFP)

deflections (Emerson, Turner et al. 1995), but several other methods, such as LFP cross-correlation, have also been employed to study traveling wave phenomena (Mizuno-Matsumoto, Okazaki et al. 1999). Due to the diversity of measures, there is a need for systematic assessment of velocity estimation methods for epileptic brain signals.

In this chapter, we develop a series of multivariate linear regression methods to detect and characterize traveling waves in EEG signals, and apply these methods to a retrospective data set consisting of high-resolution microelectrode recordings from epilepsy patients. Because of the microelectrode array's small size (4 mm square) and placement in a homogenous brain area, assessments of discharge propagation are not susceptible to confounding effects of gyral anatomy. Here, we assess the performance of several different statistical optimization methods, benchmarking to a measure derived from multiunit data. Our goal is to provide a set of computationally efficient tools for measuring speed and velocity of epileptiform discharges, along with characterizing each measure's sensitivity and variability.

2.2 Statistical methods of ictal traveling wave identification and estimation

2.2.1 Data collection

Data were recorded from epilepsy patients undergoing chronic invasive EEG in preparation for surgical treatment (Schevon, Trevelyan et al. 2009, Schevon, Goodman et al. 2010, Schevon, Weiss et al. 2012, Weiss, Banks et al. 2013, Smith, Liou et al. 2016). All patients provided informed consent prior to study involvement. The Columbia University Medical Center and University of Utah Institutional Review Boards approved this research.

14

Patients in whom the microelectrode array implant site was invaded by at least one seizure, as described previously (Schevon, Weiss et al. 2012) were included in this study, in order to ensure that methods employing multiple frequency ranges could be tested. Epileptic discharges in seizing brain are accompanied by intense, synchronized bursts of multiunit firing and correspondingly increased high gamma activity, which are not present outside seizing brain areas. (Schevon, Weiss et al. 2012) The "Utah" style arrays used (Blackrock Microsystems Inc, Salt Lake City, UT) had 96 microelectrodes, configured in a 10 by 10 grid with 400 µm inter-electrode distance and 1 mm electrode length.

Multiunit activity was obtained by filtering the 30 kHz sampled raw signal with a 300 - 3000 Hz band-pass, 512-order, zero-phase shift FIR filter (window-based). Multiunit spikes were identified from negative peaks that crossed a detection threshold of four times the standard deviation of a baseline epoch consisting of the 20 seconds before seizure onset. A minimum refractory period of 1 ms was imposed to minimize the detection of noise overriding an action potential peak. Channels with visually evident paroxysmal artifact in the raw signal or high baseline multiunit background noise (>8µV) were excluded.

LFP data were obtained by downsampling to 1 kHz after applying an 8th order Chebyshev anti-aliasing filter (400 Hz low pass). This data was then split into low and high frequency data (< 50 Hz and 80-150 Hz) using 90th order zero phase-shift FIR filters. Instantaneous high gamma power was obtained using the Hilbert transform. All calculations were performed using in-house software (Matlab, Mathworks, Natick, MA).

2.2.2 Identification of ictal discharges

      Spike trains were constructed for each channel as a sum of Dirac functions, $\sum_i \delta(t_i)$, where t_i is the channel's detected multiunit timestamps (Brown, Kass et al. 2004), then convolved with a Gaussian kernel (S.D. = 20 ms) (Bokil, Andrews et al. 2010). Discharge timing was identified from peak firing rate averaged across channels, using a threshold of 7 spikes per second and at least 100 ms separation between neighboring peaks, based on the expected maximum duration of 200 ms for an epileptiform sharp wave (Ebersole and Pedley 2003). All electrical activity within 50 ms of a firing peak was considered part of the ictal discharge (Figure 2.1) (de Curtis, Jefferys et al. 2012, Fisher, Scharfman et al. 2014, Smith, Liou et al. 2016).

Figure 2.1. Ictal discharge detection and data set construction
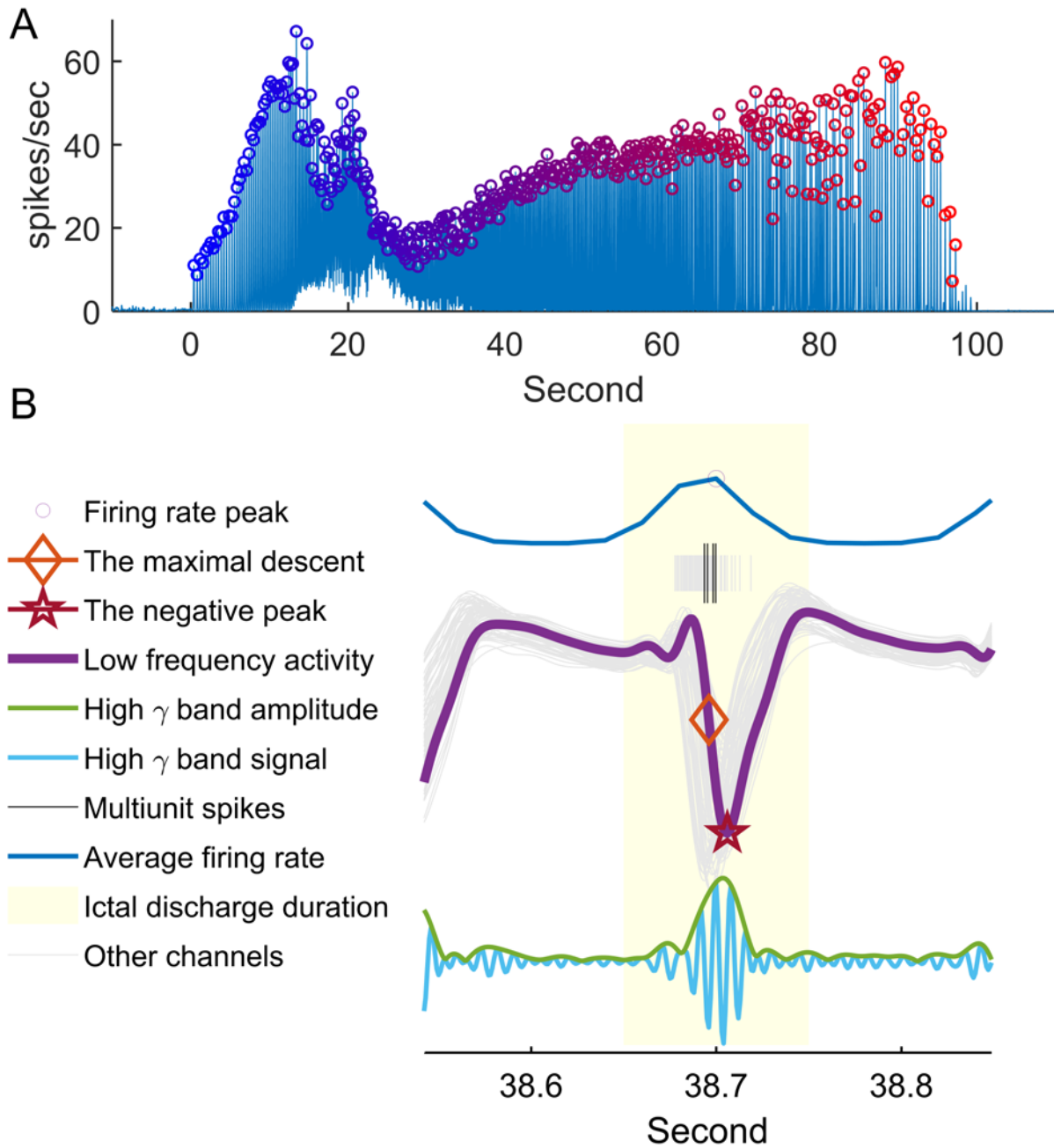
A) Detection of ictal discharges from instantaneous multiunit firing rate, averaged across
microelectrode array channels. The averaged firing rate is plotted relative to the time
from seizure onset (Patient A, seizure 3). Detection threshold was set to 7 spikes per

second. Each ictal discharge is marked with a circle with color gradient from blue to red, to show time relative to seizure onset. These same colors are used to show how traveling wave speed and direction changes with seizure progression in subsequent figures.

B) Illustration of the different discharge timing methods using data from a single channel. After detecting the peak firing time (circle), all electrical activity within 50 ms of the peak are associated with the same ictal discharge (light yellow). Multiunit spikes are shown in black, low frequency LFP in purple, and high γ activity in light blue. Matching colors are used to show timing of the negative peak (star), maximal descent (diamond), and filtered high gamma band signal, with the instantaneous amplitude (square root of high gamma power) trace shown in green.

2.2.3 Detection of ictal traveling waves and velocity estimation using multiunit spikes

Each multiunit spike was treated as a three-dimensional data point, (p_x, p_y, t), where p_x and p_y represented the spatial location in the 2-dimentional microelectrode array plane and t represented the event time. The data were subsequently fit to the Gaussian statistical model,

$$t \sim N(\boldsymbol{p}'\boldsymbol{\beta}, \sigma^2)$$

where $\boldsymbol{p} = \begin{bmatrix} p_x \\ p_y \\ 1 \end{bmatrix}$, and $\boldsymbol{\beta}$ and σ represented the inverse of velocity across recording sites and squared error in time, respectively. $\boldsymbol{\beta}$ (units: s/cm) was estimated by minimizing the squared error in the multivariate linear regression equation,

$$\widehat{\boldsymbol{\beta}} = (P'P)^{-1}P'T$$

where each row of the matrix P was the physical position of the recording microelectrode and the column vector T consisted of neural event timings. The entries of T corresponded to rows of matrix P (Kutner, Nachtsheim et al. 2004). An F-test with $\alpha = 0.05$ was used to test whether sequential multiunit firing across recording sites was present, versus the null hypothesis that multiunit spikes occur simultaneously, i.e. $\widehat{\beta_1} = \widehat{\beta_2} = 0$. The wave velocity was subsequently estimated by taking the pseudo-inverse of the first two entries of the estimator $\widehat{\boldsymbol{\beta}}$, $\widehat{\boldsymbol{V}} = pinv(\begin{bmatrix} \hat{\beta}_1 \\ \hat{\beta}_2 \end{bmatrix})$. Speed was taken as the L2 norm of the velocity estimator, $\hat{S} = |\widehat{\boldsymbol{V}}|$.

2.2.4 Field potential measures of discharge timing

A similar analysis was applied to ictal discharge timings determined from LFP data. Two

such methods were examined: negative peak, and the point at which the downward deflection is

steepest (maximal descent). The negative peak timing was selected as the minimum value in the

100 ms window assigned to each discharge. The time of maximal descent was defined as

$\underset{t}{argmin} \; \frac{\Delta L(t)}{\Delta t}$, where L is LFP voltage. Statistical testing for traveling wave classification was

done using McNemar's test with $\alpha = 0.05$.

2.2.5 Traveling wave velocity determined from high gamma power

High gamma band signal has been established as a useful index of population firing

(Nariai, Nagasawa et al. 2011, Ray and Maunsell 2011, Park, Lee et al. 2012, Weiss, Banks et al.

2013, Alvarado-Rojas, Valderrama et al. 2014). However, because of its fast oscillations, it is

difficult to specify a consistent single time point for each discharge. Therefore, instead of using

a point estimator, we used high gamma power during the period of the discharge (Figure 2.1).

Statistically, instantaneous high gamma power is represented by a tensor, $w(p_x, p_y, t)$, where p_x

and p_y are the physical positions of the recording electrodes, and t represents time. The temporal

delay information is then obtained by the equation,

$$\hat{\boldsymbol{\beta}} = (P'WP)^{-1}P'WT$$

where W is obtained by tensor vectorization and diagonalization, i.e. $W = diag(vec(w))$, and P

and T are defined as above, with each row corresponding to $vec(w)$. Shuffled data sets were

created by randomly permuting the positional information, p_x and p_y, of each channel 200 times

to test the null hypothesis, $\widehat{\beta_1} = \widehat{\beta_2} = 0$. The weighted sum of the residual squared error,

$\sum_{p_x, p_y, t} w(\boldsymbol{p}'\widehat{\boldsymbol{\beta}} - t)^2$, was then compared to the distribution of residual squared error of shuffled

data. A 5% significance threshold was used.

2.2.6 Traveling wave velocity determined from cross-correlation

Cross-correlation of LFP recordings from each pair of channels (i.e. channel i & j) was

used to measure their relative temporal delay. The timings of highest cross-correlation, $\Delta t_{i,j}$,

were fit into the following linear regression model.

$$\Delta t \sim N(\Delta \boldsymbol{p}'\boldsymbol{\beta}, \sigma^2)$$

where $\Delta \boldsymbol{p}_{i,j} = [p_{x_i} - p_{x_j} \quad p_{y_i} - p_{y_j}]$. The regression procedure was carried out similarly to

that in the multiunit regression method, except that the permutation test, rather than the F-test,

was used to test the null hypothesis, $\widehat{\boldsymbol{\beta}} = \boldsymbol{0}$, because $\Delta p_{i,j}$ were not statistically independent

observations.

2.2.7 Comparison between methods' estimation results

Ictal discharges classified as traveling waves by all tested methods were used for velocity

(i.e. speed and direction) comparisons. Because multiunit burst firing is presumed to be the

primary neural source of a seizure discharge, the multiunit estimator was chosen as a benchmark

for comparison with the LFP-based methods. The discrepancy in speed estimation was

calculated as $\Delta S_{LFP} = |\widehat{\boldsymbol{V}}_{LFP}| - |\widehat{\boldsymbol{V}}_{MUS}|$, where $\widehat{\boldsymbol{V}}_{LFP}$ and $\widehat{\boldsymbol{V}}_{MUS}$ were velocity estimates

calculated by each LFP-based method and the multiunit –based method respectively.

21

Discrepancy in direction estimation was calculated as $\Delta\theta_{LFP} = \cos^{-1}\frac{\widehat{V}_{LFP}\widehat{V}_{MUS}{}'}{|\widehat{V}_{LFP}||\widehat{V}_{MUS}|}$. Median and

inter-quartile ranges of ΔS_{LFP} and $\Delta\theta_{LFP}$ were reported. One-sample Wilcoxon signed-rank tests

were used to test for significant discrepancies in speed estimation for each method (null

hypothesis: $\Delta S_{LFP} = 0$). Friedman's tests were used for comparisons across LFP-based velocity

estimates ($\alpha = 0.05$).

2.2.8 Least absolute deviation (LAD) regression

We tested an alternative regression method using minimization of the absolute deviation

(LAD), reasoning that it would be less susceptible than least square error to the effect of outliers:

$$\widehat{\boldsymbol{\beta}}_{LAD} = \underset{\beta}{arg\,min} \sum_{p_x, p_y, t} w|\boldsymbol{p}'\boldsymbol{\beta} - t|$$

where $\boldsymbol{p} = \begin{bmatrix} p_x \\ p_y \\ 1 \end{bmatrix}$, $\widehat{\boldsymbol{\beta}}$ represents the regression coefficient, and w represents the weight associated

with each data point. Equal weighting (i.e. every w set to 1) was used for all estimators except

for the high gamma power method, where w was again set to instantaneous high gamma power.

For cross-correlation, $\boldsymbol{p}$ and t were substituted for $\Delta\boldsymbol{p}$ and Δt.

Numerically, the initial estimator, $\widehat{\boldsymbol{\beta}}$, was chosen as the least square estimator. Weights

were recursively readjusted (Holland and Welsch 1977) in order to minimize the absolute

deviation estimator as described by the following two equations.

$$U_{ii} = \sqrt{\frac{W_{ii}}{|(P\widehat{\boldsymbol{\beta}}_{old})_i - T_i|}}$$

22

$$\widehat{\boldsymbol{\beta}}_{new} = (P'UP)^{-1}P'UT$$

where W and U were both diagonal matrices, and i represents the matrix indices, scanning over

all possible p_x, p_y and t. The optimization algorithm's convergence criteria was set as

$\frac{|\widehat{\boldsymbol{\beta}}_{new} - \widehat{\boldsymbol{\beta}}_{old}|}{|\widehat{\boldsymbol{\beta}}_{old}|} < 10^{-4}$. Statistical significance was determined by comparing the residual absolute

deviation, $\sum_{p_x, p_y, t} w|\boldsymbol{p}'\widehat{\boldsymbol{\beta}} - t|$, to 200 spatially shuffled data sets, as described above.

2.2.9 Modeling low density spatial sampling

A subset of electrodes was randomly (uniformly) selected, to simulate decreased spatial

sampling density and increased inter-electrode distance. The LFP-based methods were then

applied to the reduced data set, and detection rate, change of direction ($\Delta\theta$) and speed (ΔS) were

compared to those obtained using the full data set. The robustness of each method was evaluated

by determining sensitivity for wave propagation and changes in velocity estimates. Friedman's

tests were employed to assess for consistent differences among methods across all sampling

densities.

2.3 Results

Two patients in our existing dataset met study inclusion criteria, with a total of five

seizures (Patient A with three seizures, and Patient B with two). Both microelectrode arrays

recorded from lateral temporal lobe sites (85 and 87 channels, respectively, for patients A and B).

A total of 1271 ictal discharges were detected (1029 and 242 for patients A and B, respectively).

Analysis results are summarized in Table 2.1.

Table 2.1. Features of ictal discharges in 5 seizures from two patients detected by least squares methods.

Patient	Episode	Duration (second)	# of ictal discharges	# of ictal discharges classified as traveling waves by					
				Multi-unit spikes method	The negative peak method	The maximal descent method	High gamma power method	Cross-correlation method	At least one method
A	1	58	264	141	179	191	177	209	249
A	2	73	318	143	216	246	227	260	307
A	3	99.5	447	369	349	388	335	408	438
B	1	30.58	92	75	84	85	73	88	92
B	2	34.93	150	82	142	144	122	140	149
Combined			1271	810	970	1054	934	1105	1244 (97.9%)

2.3.1 Estimating ictal traveling wave velocity by multiunit spikes

Sequential neuronal firing was identified from the spatiotemporal distribution of multiunit spikes recorded during ictal discharges.   In the example discharge (Figure 2.2A), the least squares regression technique revealed a corner-to-corner spread pattern (Figure 2.2Ai, blue to yellow, $\widehat{V}$ = [-18.2 13.8] cm/sec, F-test under null hypothesis $\beta_1 = \beta_2 = 0$, p $\ll$ 0.001). Traveling wave speed (22.9 cm/sec in this example) was determined from the slope of the propagation axis, determined by $\widehat{V}$, which revealed that neuronal bursting was sequentially activated (Figure 2.2Aii). For all detected ictal discharges, 810 out of 1271 (63.7%) met criteria for traveling waves (Table 2.1). The median speed was 35.5 cm/sec with interquartile range 22.9 to 47.2 cm/sec.

Consecutive ictal discharges were found to have more similar directions than temporally independent ones (circular correlation coefficient = 0.58, p $\ll$ 0.001). The velocity estimation results for Patient A, Seizure 3 are shown in Figure 2.2Aiii. In this example, traveling wave speed was greater for the last 25% of ictal discharges than for the first 25% (39.8 vs. 22.2 cm/sec, N = 111, Mann-Whitney U test, p $\ll$ 0.001), and their median directions shifted by 174 degrees (Median multi-sample test, p $\ll$ 0.001, N = 111). All seizures in Patient A showed significant acceleration and direction shift (median ΔS = 17.6 to 47.8 cm/sec, p $<$ 0.001; median $\Delta\theta = 146$ to 174 degrees, p $<$ 0.03.). The direction shift and speed increase match the expected effects of local seizure invasion (Smith, Liou et al. 2016), providing additional confirmation for the validity of the results.

Figure 2.2. Multiunit and LFP-based methods of determining speed and direction of ictal discharges
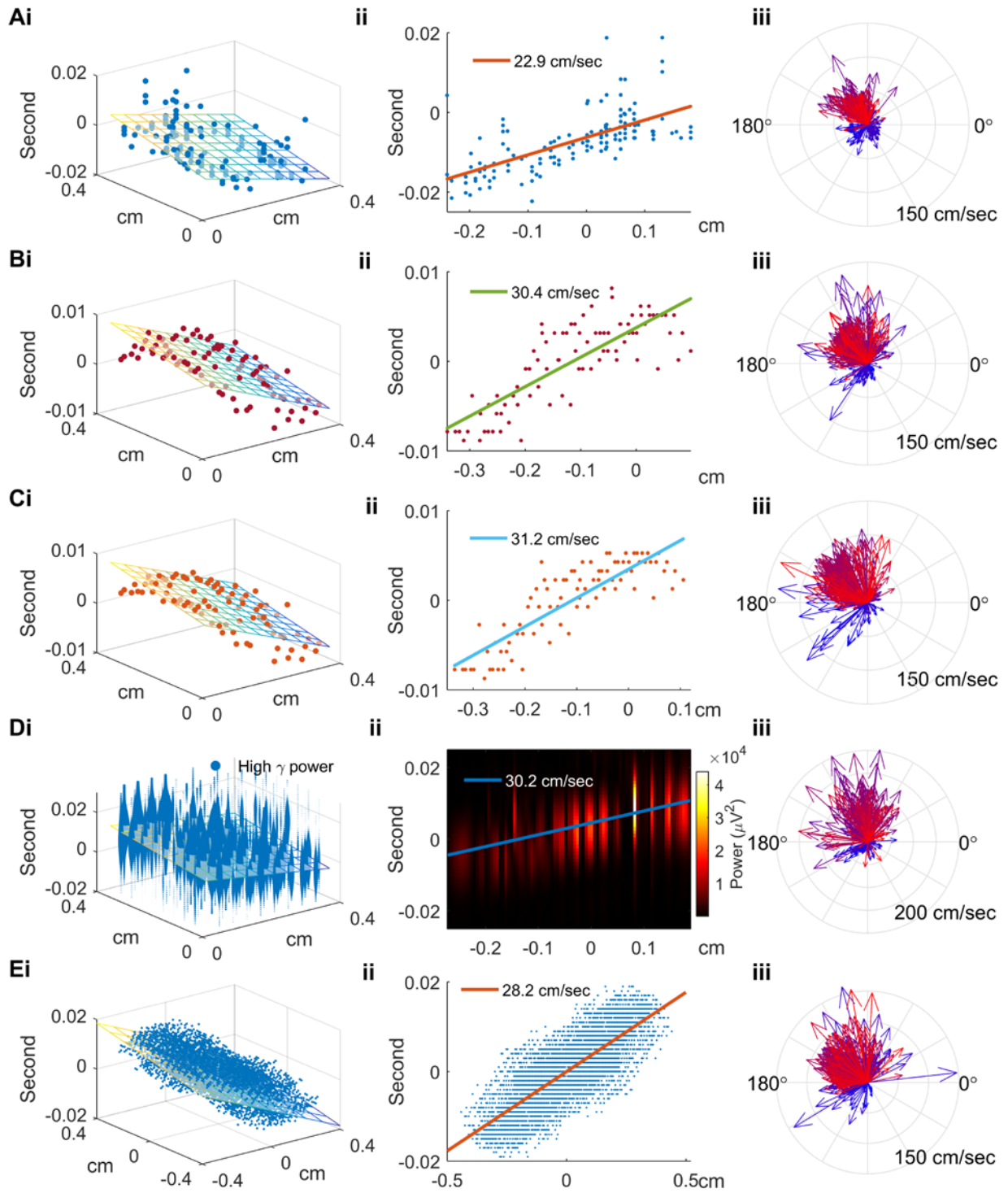
A) (i) Spatiotemporal distribution of multiunit spikes of the example ictal discharge from Figure 2.1B. The discharge is used for illustrative purposes for all figure panels' section 'i'. Physical locations and timings of multiunit spikes are scattered along the regression plane (F-test, $p \ll 0.001$). (ii) The projection of multiunit spike timings along the regression plane's gradient (propagation axis). Traveling wave speed, determined from the slope, is 22.9 cm/sec. (iii) Velocities of all discharges detected from Patient A, seizure 3, with temporal information color coded as in Figure 2.1A. The comparison of the first 25% (bluish) and the last 25% (reddish) ictal discharges illustrates the previously-reported pronounced direction shift and acceleration (see text for detailed statistics).

B) (i) Regression analysis for the example discharge using timings derived from the negative peak method. Least squares linear regression was applied to recover its propagation axis and speed (colored plane, activation sequence as blue to yellow). (ii) The projection along the propagation axis versus timings of the negative peaks. (iii) Similar to Aiii using the negative peak method applied to all discharges from Patient A, seizure 3. The speed increase and direction shift from early to late seizure periods are again seen.

C) Similar to Bi-iii, with timing determined using the maximal descent method.

D) Similar to Bi-iii and Ci-iii with timing determined using high gamma power. Panels i and ii show the sequential pattern of instantaneous high gamma power along the propagation axis (permutation test, $p < 0.005$). (Ei-iii) Similar to above, using the cross-correlation method (permutation test, $p < 0.005$).

2.3.2 Estimating ictal traveling wave velocity from low frequency activity

We next tested two LFP-based measures of ictal discharge timing: negative peak and point of maximal descent, both of which have been employed in prior studies (Viventi, Kim et al. 2011, Smith, Liou et al. 2016, Vanleer, Blanco et al. 2016). The spatiotemporal distributions of ictal discharge event timing, estimated by each method respectively, are shown in Figure 2.2B-C for the example ictal discharge used in Figure 2.2A. As with the multiunit spike method (Figure 2.2A), a corner-to-corner spread pattern was found using both methods (Figure 2Bi, $\widehat{V}$ = [-28.2 11.4] cm/sec, F-test p << 0.001; Figure 2.2Ci, $\widehat{V}$ = [-28.7 12.4] cm/sec, F-test p < 0.001.). Estimated traveling wave speed was 30.4 and 31.2 cm/sec, respectively.

We then applied both methods to the entire data set. Of the 1271 ictal discharges detected, 970 (76.3%) were classified as traveling waves using the negative peak method, and 1054 (82.9%) using maximal descent (Table 2.1). Median estimated speeds were 45.7 (range 27.5-61.7) and 51.8 (range 28.4-69.7) cm/sec using each method, respectively. Temporally correlated ictal discharges shared similar directions, as circular correlation coefficients of two consecutive traveling waves were 0.55 and 0.46, respectively (p << 0.001). Results from the example seizure (Patient A, seizure 3) are shown in Figures 2.2Biii and 2.2Ciii. Again, traveling wave speeds were found to be slower at the beginning of the seizure than at the end (negative peak: 21.8 versus 53.2 cm/sec, Mann-Whitney U test, p < 0.001; maximal descent: 29.2 versus 56.2 cm/sec, Mann-Whitney U test, p < 0.001, N = 111). The median direction also shifted as seen previously (negative peak: 89 degrees, median multi-sample test, p < 0.001; maximal descent: 94 degrees, median multi-sample test, p < 0.001, N = 111). Similar velocity changes were observed in Patient A's other seizures (negative peak: median $\Delta\theta$ = 89 to 137 degrees, p <

0.001; and median ΔS = 31.3 & 41.7 cm/sec, p < 0.001; maximal descent: median $\Delta\theta$ = 94 to 176 degrees, p < 0.001; median ΔS = 27.0 to 38.4 cm/sec, p < 0.001).

2.3.3 Estimating ictal traveling wave velocity using high gamma power

To provide an additional method that may translate to standard ECoG recordings, we next examined traveling wave propagation using high gamma (80 – 150 Hz) power. Figure 2.2D shows the temporal evolution of instantaneous high gamma power with its corresponding physical location for the example discharge. In agreement with previous observations, we found that high gamma power progressed sequentially from corner to corner of the microelectrode array (Figure 2.2Di). A regression plane that minimized weighted squared loss confirmed that this discharge exhibited the properties of a traveling wave ($\widehat{V}$ = [-24.0 18.3] cm/sec, shuffle test p << 0.001, $|\widehat{V}|$ = 30.2 cm/sec, Figure 2.2Di-ii).

We then estimated traveling wave velocity using high gamma power across the entire data set. Of the 1271 ictal discharges detected, 934 (73.5%) were classified as ictal traveling waves (Table 2.1). The median estimated speed was 51.1 (range 27.8 - 74) cm/sec. The circular correlation coefficient again showed continuously evolving wave directions (0.46, p << 0.001). Using the same seizure example as in the previous panels, Figure 2.2Diii again illustrates the increase in speed and the direction shift between the first and last 25% of ictal discharges (median speed 31.1 vs. 63.9 cm/sec, Mann-Whitney U test, p < 0.001; median direction change: 179 degrees, median multi-sample test, p < 0.001, N = 111). The acceleration and direction shift were seen in all Patient A's seizures (median $\Delta\theta$ = 135 to 179 degrees, p < 0.002; median ΔS = 31.0 to 34.7 cm/sec, p < 0.001).

2.3.4 Estimating ictal traveling wave velocity using cross-correlation

Cross-correlation, a commonly used bivariate method for estimating signal delays, has been applied to study ictal traveling waves (Kramer, Szeri et al. 2007, Kramer, Kolaczyk et al. 2008). Applying this method to our data produced results similar to the methods described above (Figure 2.2Ei, corner to corner pattern, $\widehat{V}$ = [-26, 11.1] cm/sec; 2Eii, $|\widehat{V}|$ = 28.2 cm/sec, F-test p < 0.001). The direction shift and acceleration in velocities in the early vs. late seizure periods for Patient A's three seizures were corroborated using this method (median ΔS = 33.0 to 39.8 cm/sec, p < 0.001; median $\Delta\theta$ = 34 to 168 degrees, p < 0.001), although the direction shift was less prominent in Seizure 3 (Figure 2.2Eiii, median direction change = 34 degrees, median multi-sample test, p < 0.001; median speed change: 35.4 cm/sec, Mann-Whitney U-test, p < 0.001, N =111).

2.3.5 Comparison of estimation results between LFP-based and multiunit methods

Next, we compared direction and speed estimates obtained with the tested methods, using ictal discharges that were classified as traveling waves by all four estimators (N=510, Figure 2.3). In our dataset, the negative peak and maximal descent methods yielded more similar results to those from the multiunit estimators than did the high gamma power and cross correlation methods (Figure 2.3, circles, Friedman's test for equal median $\Delta\theta$, p << 0.001; Friedman's test for equal median ΔS, p << 0.001).

Figure 2.3. Comparison of traveling wave velocities calculated using the different methods.
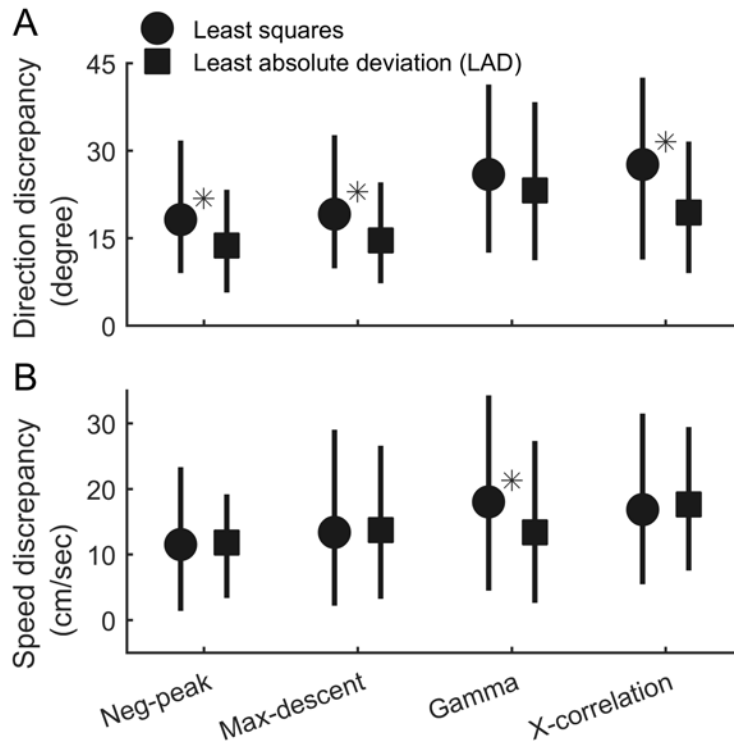
Estimation discrepancies between multiunit and LFP-based estimators are shown, comparing the

set of discharges that were classified as traveling waves by all methods. Results of the multiunit

estimators were used as the benchmark for comparison. For each of the four LFP-based

measures, median discrepancies compared with the multiunit estimator (circles & squares) and

interquartile ranges (error bars) are shown.

A) The negative peak and maximal descent methods gave results that were more similar to

the multiunit estimator than those of the high gamma power and cross-correlation

methods (circles, Friedman's test, N = 510, p < 0.001). Using LAD in place of least

squares regression tended to reduce direction discrepancies between all LFP-based and

multiunit estimators (comparison between circles and squares, in the order indicated by

the X axis, change of median $\Delta\theta$ = -4.4, -4.5, -2.8, -8.2 degrees, Mann-Whitney U-test: p = <<0.001, <<0.001, 0.189, <<0.001 from left to right. N = 510 versus 354). Asterisks indicate statistically significant differences between least squares and LAD methods (α=0.05).

B) Speed estimation again showed a similar pattern of results among the four LFP-based methods using least squares regression (circles) (Friedman's test, N = 510, p < 0.001). Adopting LAD regression did not increase the speed discrepancies with the multiunit estimator with the exception of the high gamma power method, where the discrepancy decreased (change of median ΔS = +0.3, +0.4, -4.6, +0.8 cm/sec, Mann-Whitney U-test: p = 0.64, 0.79, 0.008, 0.66 from left the right. N=510 versus 354).

2.3.6 Least absolute deviation (LAD) regression

We observed that speed estimation was particularly sensitive to extreme outliers. To address this issue, we changed the estimators' loss functions from least squares to absolute loss magnitude. As shown in Figure 2.3, LAD regression tended to reduce discrepancies between LFP-based and multiunit methods (Figure 2.3, squares, $N = 359$, see figure legends for statistical test results), without affecting the proportion of discharges classified as traveling waves (see Table 2.2 for detailed statistics).

Table 2.2. Least absolute deviation regression results

Patient	Episode	Duration (second)	# of ictal discharges	# of ictal discharges classified as traveling waves by					
				Multi-unit spikes method	The negative peak method	The maximal descent method	High gamma power method	Cross-correlation method	At least one method
A	1	58	264	99	211	211	170	175	260
A	2	73	318	96	284	269	197	212	313
A	3	99.5	447	319	422	386	291	348	443
B	1	30.58	92	73	79	82	58	47	90
B	2	34.93	150	84	141	144	88	125	149
Combined			1271	671	1137	1093	804	907	1255 (98.7%)

2.3.7 Simulating low spatial sampling density

Sparse sampling of large cortical areas is a common challenge in clinical recordings. We therefore tested the LFP estimators under reduced sampling densities, simulated by removing randomly-selected channels (Figure 2.4). As expected, the traveling wave detection rate declined with decreased channel density (Figure 2.4A), and the direction variability increased (Figure 2.4B). With regard to speed estimates, reducing spatial sampling density introduced both negative bias (Figure 2.4C) and variability (Figure 2.4D), with negative peak and maximal descent methods providing superior results.

Figure 2.4. Simulation of reduced spatial sampling.
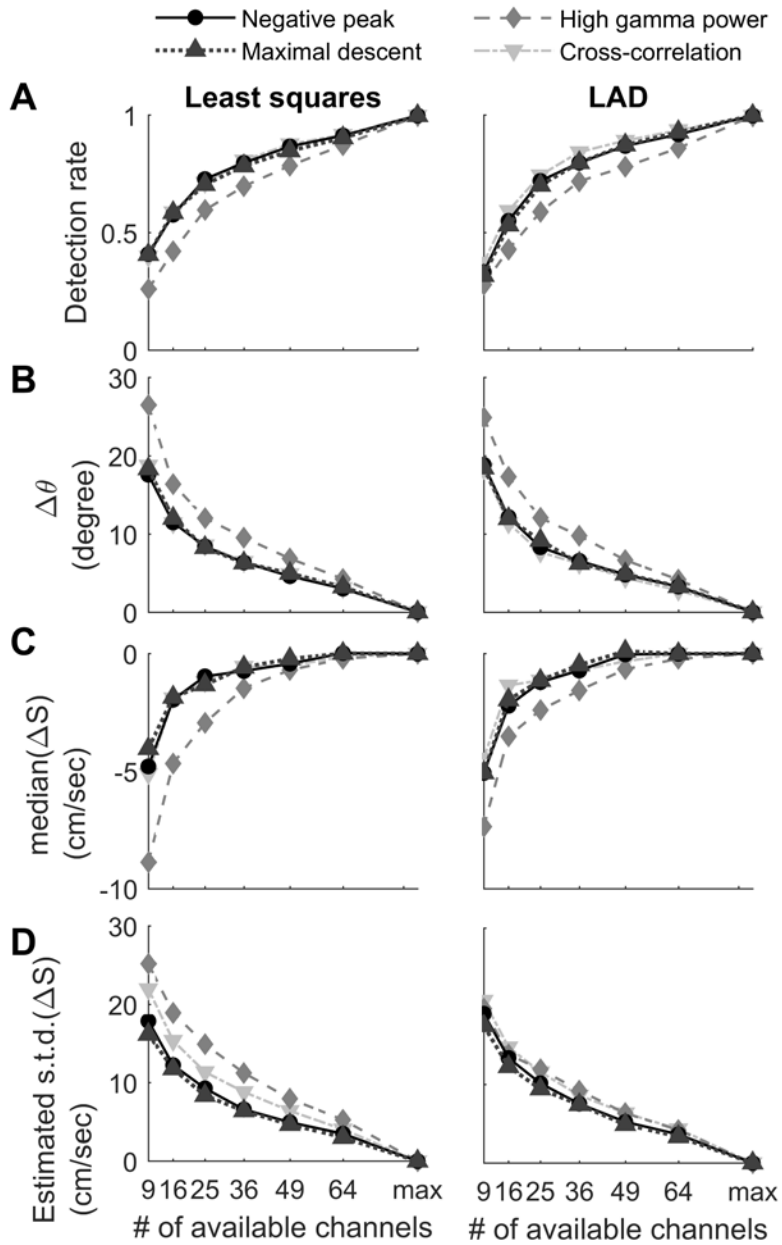
The performance of the four LFP-based estimators under reduced spatial sampling conditions were benchmarked against the same method's results under full sampling configurations (85 and 87 electrodes for Patient A and B respectively).

A) Unsurprisingly, the rate of detection of traveling wave behavior decreased with spatial sampling density. The high gamma power method consistently had lower detection sensitivity in all reduced spatial sampling conditions. (Friedman's test $p < 0.001$ in left and right subpanels).

B) Similar results were found for the direction calculation, with high gamma power methods appearing to be the least robust under reduced spatial sampling conditions. Friedman's tests: $p = 0.007$ (least squares, left) and 0.001 (LAD, right).

C) Low spatial sampling density introduced a negative bias in speed estimation, with the high gamma power method introducing the most severe negative bias. Friedman's tests: $p = 0.009$ (least squares, left) and 0.004 (LAD, right).

D) Standard error of speed estimation (robustly estimated by $\frac{median(|\Delta S|)}{0.6745}$) demonstrated that the maximal descent & negative peak methods had consistently better speed estimation results under reduced density conditions. (Both Friedman's test, $p < 0.001$.)

2.4 Discussion

We have shown that the majority of human ictal discharges in our dataset of five seizures exhibited characteristics of traveling waves at the high level of granularity (400 μm interelectrode distance) of the Utah microelectrode array, using a variety of measures applied to data across a range of frequencies. In our dataset, both the conceptually and computationally simple (negative peak and maximal descent) and complex (high-gamma power and cross-correlation) methods produced results similar to the multiunit estimator. As there is no established "ground truth" for a traveling wave's location in the case of epileptiform discharges, we selected the multiunit estimator as a benchmark because synchronized, intense neuronal bursts are the source of both LFP and multiunit spikes in seizing brain. We also found that adopting least absolute deviation (LAD) regression reduced discrepancies between LFP-based and multiunit methods.

We conducted the study with ictal discharges recorded with the Utah microelectrode array located within seizing brain territory for several reasons. First, the ictal discharges were accompanied by neuronal burst firing. This is not necessarily the case for discharges detected outside seizing brain territories, due to the effects of inhibitory restraint of pyramidal cell firing in non-recruited territories. We were thus able to use multiunit firing to compare the performance of several methods based on wideband or high frequency LFPs. Second, the placement of the array into a visualized cortical site free of anatomical irregularities minimized variations in physical inter-electrode distance. Finally, the fine resolution of the Utah array provided an excellent test of the traveling wave property, indicating that temporal delays could be discerned even over submillimeter distances.

Our findings suggest that virtually all ictal discharges, observed in clinical EEG and ECoG, propagate across the cortical surface, even when measured from within the boundaries of seizing brain. Evidence for traveling wave behavior of epileptiform discharges has been documented in several prior studies (Gotman 1983, Emerson, Turner et al. 1995, Alarcon, Garcia Seoane et al. 1997, Martin Miguel Mdel, Garcia Seoane et al. 2011, Gonzalez-Ramirez, Ahmed et al. 2015, Smith, Liou et al. 2016), including one in which discharges recorded simultaneously in ECoG and microelectrodes, and analyzed separately, demonstrated aligned propagation directions (Smith, Liou et al. 2016). This stands in contrast to the traditional view that the extended field of ictal discharges is a consequence of volume conduction from a spatially-constrained source, or alternatively that they arise simultaneously from a large cortical territory (Ebersole 1994, Ebersole 1997, Ebersole 2000, Wolters and de Munck 2007, David, Bastin et al. 2010, Kramer and Cash 2012). The impression of ictal discharges as large-area, simultaneous events is likely due to their high traveling speeds and the coarse time scale on which they are typically visualized. At the median speed of 35.5 cm/sec in our study (multiunit estimator, interquartile range 22.9 to 47.2 cm/sec), the delay across a one cm distance (the distance between electrodes on a standard ECoG grid) is only 28 milliseconds.

A number of studies have measured the temporal delay of epileptiform discharges in human scalp EEG, subdural (Alarcon, Garcia Seoane et al. 1997, Martin Miguel Mdel, Garcia Seoane et al. 2011) and microelectrode array (Gotman 1983, Emerson, Turner et al. 1995, Gonzalez-Ramirez, Ahmed et al. 2015, Smith, Liou et al. 2016) recordings. Various methods to measure propagation speed and direction have been proposed, from simple estimates based on the timing of signal extrema (Chagnac-Amitai and Connors 1989, Emerson, Turner et al. 1995, Alarcon, Garcia Seoane et al. 1997, Smith, Liou et al. 2016), to more complicated estimates,

such as coherence-based measurements (Gotman 1983), with wave speeds measured at 25-75 cm/sec. Propagation of stimulus-evoked waves has been estimated using the phase of beta oscillations with a microelectrode array similar to that used in this study (Rubino, Robbins et al. 2006). However, we did not include this method in our study as it was found to be too sensitive to the noise inherent in high-frequency, single-trial data (80-150 Hz) with uncertain event timing. Discharges induced by pharmacologically blocking GABA-A receptors travel at speeds of 10-25 cm/sec in rat and cat neocortex *in vivo* (Goldensohn and Salazar 1986, Chervin, Pierce et al. 1988, Ma, Zhao et al. 2013). Rodent brain slice studies reported wave speeds in the range of 5 to 10 cm/sec (Wadman and Gutnick 1993, Pinto, Patrick et al. 2005, Trevelyan, Baldeweg et al. 2007). Theoretical studies have shown that traveling waves in the speed range found in our study could emerge from over-excitable recurrent networks (Golomb and Amitai 1997). Chronic remodeling of axonal and white matter connections in the epileptic condition may explain the faster traveling wave speeds in the human recordings compared to acute animal *in vivo* studies (Isokawa 2000).

High gamma band signal is accessible from clinical recordings, and has been shown to be a surrogate marker of synchronized neuronal firing, particularly the intense burst firing characteristic of seizing brain (Manning, Jacobs et al. 2009, Ray and Maunsell 2011, Weiss, Banks et al. 2013). While this method was generally effective, it proved to be less robust under low spatial sampling conditions. The computationally expensive cross-correlation method did not outperform the simpler negative peak and maximal descent methods in our dataset, perhaps due to the effects of variations in LFP morphology across the recording areas. This result, however, does not exclude the possibility of conditions in which cross-correlation outperforms the simpler methods.

41

Replacing squared error with absolute deviation (Powell 1984) proved to be valuable in reducing the discrepancies between LFP-based and multiunit estimators. LFP-based methods approximating the results of multiunit estimators may allow the study of neuronal dynamics without requiring direct observation of multiunit band signals. More attention to developing sophisticated robust regression methods for evaluating the temporal evolution of epileptic activity may further improve the quality of speed and direction measurements (Rousseeuw and Leroy 2005).

Finally, all statistical models we proposed in this manuscript assume the traveling waves' speed and direction remained constant as the wave moved through the recording area. However, more complex traveling wave patterns, such as spiral waves, have been observed in seizing brains (Huang, Xu et al. 2010), and our group has documented shifts in both speed and direction due to propagation of the ictal wavefront, or the leading edge of seizing cortical territory (Smith, Liou et al. 2016). To discover complex wave patterns, statistical models that are more adaptive to local structures will be required. Further, the trade-off between variance (more adaptive models) and bias (simple models) should be customized according to the characteristics of datasets.

The methods tested here provide reasonable estimates for ictal traveling wave direction in clinically available frequency bands, thus opening up possibilities for assessing whether this information can help locate seizure origination sites, given the relationship of the traveling waves to the seizure generator. The increasing recent attention to large-scale networks in epilepsy highlights the potential value of this previously underutilized analysis method for EEG-based studies (Smith and Schevon 2016). Applying the methods developed here to animal seizure

models and clinical recordings can aid future investigations of ictal traveling waves, their

relationship to seizure generators, and their potential clinical utility.

2.5 Additional challenges and solutions

This section is optional for readers who are interested in theoretical explanation for speed estimation bias and advanced velocity estimation methods.

2.5.1 Positive bias of speed estimation

The model

$$T \sim N(P\beta, \sigma I^2)$$

If σ is already known, the estimator for β follows a multivariate Gaussian distribution.

$$\hat{\beta} \sim N((P'P)^{-1}PT, \sigma^2(P'P)^{-1})$$

Velocity in this method is the pseudoinverse of β excluding the constant term, which here we use the notation $\hat{\beta}_v$ to represent it. Consider a marginal distribution along the velocity axis, $\hat{\beta}_m$, which also has a normal distribution. Speed estimator, $\hat{s}$, is defined to be the inverse of distance from $\mathbf{0}$ at β plane, $\hat{s} = \frac{1}{\|\hat{\beta}_m\|}$. The problem is that the mean, $\langle \hat{\beta}_m \rangle$, diverges to $+\infty$.

Take expectation.

$$E[\hat{s}] = E\left[\frac{1}{\|\hat{\beta}_m\|}\right] = \int_{-\infty}^{+\infty} \frac{1}{\|\hat{\beta}_m\|} N\left(\mu_{\widehat{\beta}_m}, \sigma_{\widehat{\beta}_m}\right) d\widehat{\beta}_m$$

This integral $\to \infty$. Therefore, this estimator will always be positively biased.

Proof: 1) Let's see the following integral

$$\int_{-\infty}^{\infty} \frac{1}{|x|} \exp(-(x-\mu)^2) dx$$

Because both terms, $\frac{1}{|x|}$ and $\exp(-(x-\mu)^2)$ are non-negative. Therefore, only integrating it

within the neighborhood, $[-\epsilon, \epsilon]$, $\epsilon > 0$, will produce a smaller result than the original integrand.

$$\geq \int_{-\epsilon}^{\epsilon} \frac{1}{|x|} \exp(-(x-\mu)^2) dx$$

Then, using the knowledge that the image of exponential function is always positive and $\mu \neq \pm\infty$,

$$\geq \int_{-\epsilon}^{\epsilon} \frac{1}{|x|} \min_{[\epsilon, +\epsilon]} (\exp(-(x-\mu)^2)) dx$$

$$= \int_{-\epsilon}^{\epsilon} \frac{b}{|x|} dx$$

where b is an arbitrarily small positive constant. We therefore can take b out,

$$= 2b \int_{0}^{\epsilon} \frac{1}{x} dx$$

$$= +\infty$$

Therefore, in this regime, it is not possible to properly infer velocity because the inverse of $\hat{\beta}$ is

expected to be infinite. The result therefore guarantees $\langle \hat{s} \rangle = +\infty$.

If σ is unknown, then the distribution will be a t-distribution. The same problem still

exists because the integral does not converge. Therefore, I argue that the less the sample you

have, you are more deviant from the $\frac{1}{\beta}$. This explains why LFP-based methods are positively

biased (Figure 2.3), and the positive bias becomes more exaggerated when sampling density is

low (Figure 2.4).

There is another easier way to show speed estimator is positively biased by using Jensen's inequality. Within $(0, \infty)$, 1/x is a convex function. Therefore, consider the random variable $\left|\widehat{\beta_m}\right|$, by Jensen's inequality,

$$\langle \hat{s} \rangle = \left\langle \frac{1}{\left|\widehat{\beta_m}\right|} \right\rangle \geq \frac{1}{\left\langle \left|\widehat{\beta_m}\right| \right\rangle} = \frac{1}{\left|\beta_m\right|} = s$$

2.5.2 Kalman smoother for sparse spatial sampling challenge

In clinical practice, few intracranial EEG recordings are done by multielectrode arrays due to their limited spatial coverage and invasiveness. Instead, subdural electrode grids and strips are more commonly used. However, this creates a great challenge to estimate ictal traveling wave velocities. Inter-electrode distance of ECoG recordings is huge; minimally distance currently used in clinical practice is still 5 mm, significantly larger than inter-electrode distance of multielectrode arrays (0.4 mm). Limited spatial sampling is a great challenge for estimating traveling wave velocities (Figure 2.4). First, it reduces available data, making estimators uncertain and creating positive bias (see the previous section). Second, large cortical surface is required for obtaining enough data points; however, assuming traveling wave velocity is constant in a large cortical region can be invalid. Moreover, the distorted gyrus-sulcus anatomy can further invalidate the assumptions of linear regression methods.

Bayesian inferences can be applied to counteract the first two challenges. As shown in Figure 2.2, we have known ictal traveling waves do not flip randomly. While estimating an ictal discharge's direction, it is therefore reasonable to use the previous estimation result as prior

knowledge so that the number of electrodes required for estimating this episode can be reduced. Prior knowledge helps to ameliorate the challenge of low spatial density. By constraining current estimator with prior information, the estimator's confidence interval can be reduced, ameliorating challenge 1. Because less electrodes are required, the surface area of cortical region required for estimating traveling wave velocities is also reduced, ameliorating challenge 2.

Here, I propose a Kalman smoother-based approach, using expectation-maximization algorithm (Kalman 1960) to estimate traveling wave velocities under low spatial sampling density conditions. Specifically, for an ictal discharge episode (index n), the associated multiunit spike timings, listed in the column vector T_n, are statistically modeled as

$$T_n = N(P_n \beta_n, r_n I)$$

$$\beta_n = N(\beta_{n-1}, (\tau_n - \tau_{n-1})Q)$$

Where P_n is an $n_{MUS} \times 2$ matrix encoding electrodes' spatial information. r_n, a scalar, represents observation noise. β_n contains ictal discharge timing (the first entry) and information about traveling wave velocity (the second and third entries). Notice, for numerical stability reasons, I have demeaned the matrix P_n and vector T_n first. So the intercept of the regression plane is 0. β evolves continuously, since we have learned that traveling wave directions do not randomly flip. Therefore, β is modeled as a random walk process. τ is timing of discharge. The duration two ictal discharges are separated controls how similar the two velocities should be, controlled by the covariance matrix $(\tau_n - \tau_{n-1})Q$.

The algorithm starts with an initial guess of $\hat{r}_n$, $\hat{Q}$, and $\hat{\beta}_1$. Then, E-step can be done by Kalman smoother. Forward filter is done by the following steps

$$\hat{\beta}_{n+1} = A\hat{\beta}_n$$

$$\Sigma_{n+1} = \Sigma_n + (\tau_n - \tau_{n-1})\hat{Q}$$

Therefore, Kalman gain is

$$K = \Sigma_{n+1}P'_{n+1}\left(P_{n+1}\Sigma_{n+1}P'_{n+1} + r_{n+1}I\right)^{-1}$$

Update the $n+1$ discharge's estimator and estimator covariance

$$\hat{\beta}_{n+1} \leftarrow \hat{\beta}_{n+1} + K(T_{n+1} - P_{n+1}\hat{\beta}_{n+1})$$

$$\Sigma_{n+1} \leftarrow \Sigma_{n+1} - KP_{n+1}\Sigma_{n+1}$$

After reaching the last discharge, we next do backward filtering. First, we import Kalman filter estimator and covariance as the smooth estimators, $\hat{\beta}^S$, and their covariance, Σ^S, for every discharge n

$$\hat{\beta}_n^S \leftarrow \hat{\beta}_n$$

$$\Sigma_n^S \leftarrow \Sigma_n$$

Starting from the last discharge, we calculate backward gain,

$$L_n = \Sigma_n\left(\Sigma_n + (\tau_{n+1} - \tau_n)\hat{Q}\right)^{-1}$$

Now apply it to update the smooth estimators and covariance

$$\hat{\beta}_n^S \leftarrow \hat{\beta}_n + L_n(\hat{\beta}_{n+1}^S - \hat{\beta}_n)$$

$$\Sigma_n^S \leftarrow \Sigma_n + L_n\left(\Sigma_{n+1}^S - \left(\Sigma_n + (\tau_{n+1} - \tau_n)\hat{Q}\right)\right)L_n'$$

After finishing Kalman smoothing, we need to maximize expected log likelihood to update $\hat{r}_n$ and $\hat{Q}$. According to the property of normal distribution, we know

$$\langle \beta_n | T \rangle = \hat{\beta}_n^S$$

$$\langle \beta_n \beta_n' | T \rangle = \Sigma_n^S + \hat{\beta}_n^S \hat{\beta}_n^{S'}$$

$$\langle \beta_n \beta_{n+1}' | T \rangle = \hat{\beta}_n \hat{\beta}_{n+1}^{S}{}' + L_n(\Sigma_{n+1}^S + (\hat{\beta}_n^S - \hat{\beta}_n)\hat{\beta}_{n+1}^{S}{}')$$

Bra-ket notation is used for expectation value.

By setting the derivative of expected log likelihood of this system to 0, we obtained the update rule.

$$\hat{Q} \leftarrow \frac{1}{N_d} \sum_{n=1}^{N_d-1} (\tau_{n+1} - \tau_n)^{-1} \langle \beta_{n+1} \beta_{n+1}' + \beta_{n+1} \beta_n' + \beta_n \beta_{n+1}' + \beta_n \beta_n' | T \rangle$$

$$\hat{r}_n \leftarrow \frac{1}{N_{s.n}} trace(T_n T_n' - T_n \hat{\beta}_n^{S}{}' P_n' - P_n \hat{\beta}_n^S T_n' + P_n \left(\hat{\beta}_n^S \hat{\beta}_n^{S}{}' + \Sigma_n^S \right) P_n')$$

Where N_d is total number of ictal discharges; $N_{s.n}$ is the number of multiunit spikes affiliated with ictal discharge n.

Figure 2.5 shows the comparison between full electrode, 9-electrode condition, and rescued estimation results from Kalman smoother based on multiunit spikes. Clearly, the direction error is significantly reduced.

Figure 2.5 Kalman smoother improves estimation quality under sparse spatial sampling condition.
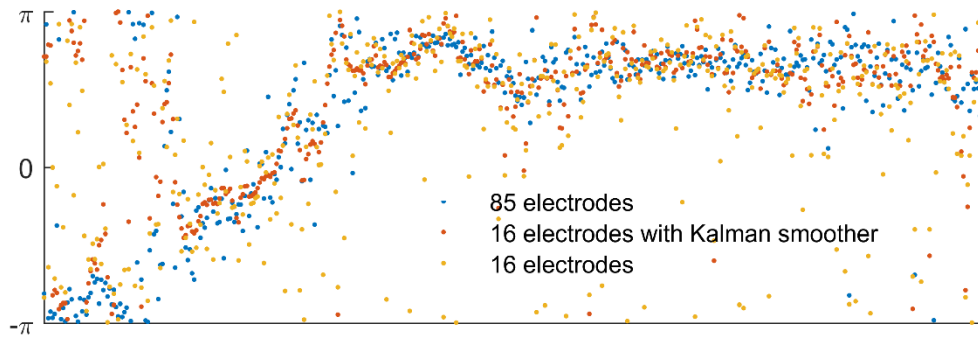
The sample seizure shown in Figure 2.2. Circular correlation coefficients between full-electrode configurations versus smoothened 16-electrode configuration: 0.45. Circular correlation coefficients between full-electrode configurations versus raw 16-electrode configuration: 0.35. Shuffle-test: $p < 0.01$.

This algorithm can be easily extended to any point process-based ictal traveling wave estimation methods.

Chapter 3

Role of inhibitory control in modulating of focal seizure propagation

Abstract

Focal seizure propagation is classically thought to be spatially contiguous, as exemplified by Jacksonian march. However, propagation through epileptic network – a collection of disparate epileptic nodes – has also been observed. Here, we used multielectrode array, wide field calcium imaging, and two-photon calcium imaging to study focal seizure propagation pathways. 4-Aminopyridine (4-AP) injection in rodent neocortex induced a small ictal focus (2-3 mm), electrographically similar to human spontaneous focal seizures. Despite of its focality, neuronal bursts within the focus were associated with hemisphere-wide LFP fluctuations and paralbumin-positive interneuron activity in distant regions (4 mm). Globally compromising this inhibitory response by bicuculline surface application resulted in classical contiguous propagation; whereas, focal bicuculline injection could result in ictal events with two physically disparate foci. Multifocal ictal events were demonstrated. Two dynamically distinct ictal foci could be induced by focal bicuculline injection, indicating pathological, chronically altered cortico-cortical connectivity may not be required for epileptic network formation. Our study suggested both classical and epileptic network propagation could both arise from inhibition defect. Variation in cortical topology may explain the preferred pathway in various cases.

3.1 Introduction

3.1.1 Classical contiguous seizure propagation versus epileptic network formation

The topology of seizure propagation has long been debated, and is believed to depend on factors such as cortical connectivity and underlying pathology. Classically, seizures are thought to spread to physically contiguous regions, expanding in a sequential manner through progressive recruitment of adjacent cortical circuitry (Figure 3.1A). This progression manifests clinically during the well-known Jacksonian march(Extercatte, de Haan et al. 2015), has been extensively documented in animal models, both in vivo and in vitro(Bikson, Fox et al. 2003, Pinto, Patrick et al. 2005, Trevelyan, Sussillo et al. 2006, Trevelyan, Sussillo et al. 2007), and was recently demonstrated in spontaneous human seizures(Schevon, Weiss et al. 2012, Smith, Liou et al. 2016). In contrast to this classical view, propagation through 'epileptic networks' – presumed pathological connections of dispersed cortical regions (Figure 3.1B) – has also been recently proposed and supported by both imaging and intracranial low-frequency EEG studies(Kramer, Eden et al. 2010, Luo, An et al. 2014, Khambhati, Davis et al. 2016). These observations raise unanswered questions such as how neural activity in disparate cortical regions synchronizes, whether pathological connectivity is required, and precisely how epileptic activity propagates through long-range cortico-cortical connections.

Epileptiform discharges during focal seizures can be observed at a significantly larger spatial scale than its neuronal substrates. This has been traditionally ascribed to a passive volume conduction process. However, analysis of in vivo human microelectrode recordings demonstrate that epileptiform discharges are generated by synaptic barrages emanating from a small ictal core(Schevon, Weiss et al. 2012, Weiss, Banks et al. 2013). Detailed in vitro brain

slice studies have shown that in normal tissue, a fast, strong inhibitory conductance prevents the distributed synaptic activity from triggering ictal activity(Trevelyan, Sussillo et al. 2006, Trevelyan, Sussillo et al. 2007), and evidence of the same process has been detected in humans(Schevon, Weiss et al. 2012). The in vivo 4- aminopyridine (4-AP) model has also suggested widespread projections from a localized ictal event, as shown by its large-scale subthreshold excitatory propagating waves and neurovascular coupling effect(Bahar, Suh et al. 2006, Ma, Zhao et al. 2009, Zhao, Ma et al. 2009, Zhao, Nguyen et al. 2011, Ma, Zhao et al. 2013). Given the electrographic similarity of 4-AP ictal events to human neocortical-onset seizures, the area of bursting cells, i.e. the 4-AP ictal core, should also be significantly smaller than the region demonstrating epileptiform discharges. However, relevant evidence is still lacking.

Here, we assess the effects of ictal activity projection at varying cortical distances, as well as inhibitory responses using multielectrode arrays, wide field calcium imaging, and two-photon calcium imaging of interneurons in the acute rodent in vivo 4-AP model, using bicuculline methiodide (BMI) to block GABA-A activity at varying distances from the core. We hypothesize that strongly excitatory synaptic projections arise from the ictal core and are distributed widely, but are normally masked by local inhibitory responses. Sites in which inhibitory responses are compromised allow the seizure to jump to distant sites, therefore providing a substrate for the formation of physically disparate ictal cores. This provides a plausible mechanism for observed large-scale epileptic network behavior during human seizures(Smith and Schevon 2016). It also suggests that seizure propagation can proceed via two topologically distinct patterns that both depend on the inhibition breakdown process: one

involving slow (< 1 mm/sec), contiguous spread and the other operating across large distances at

much greater speeds, on the order of several cm/sec.

Figure 3.1. Two patterns of focal seizure propagation.
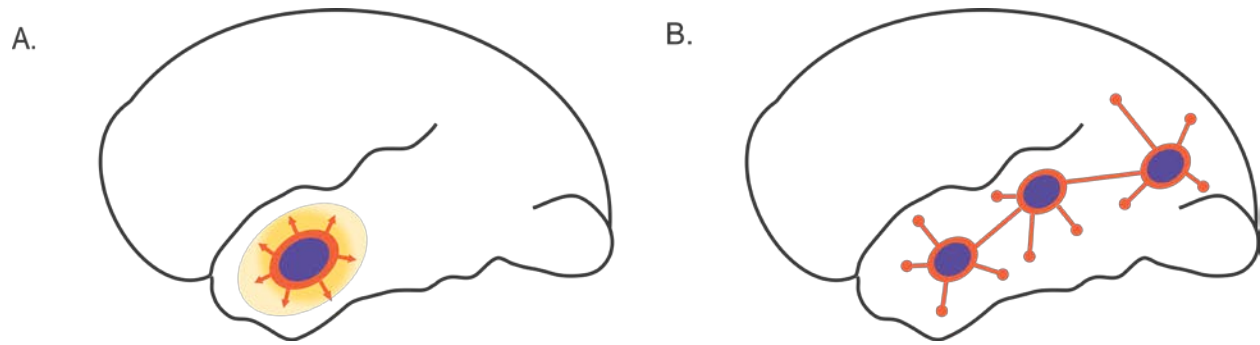
A) Classical, Jacksonian-like seizure propagation. The purple zone is the ictal core,

   surrounded by the ictal wavefront (orange), slowing expansion toward adjacent cortical

   circuitry. The yellowish gradient surrounding the core represents the 'ictal penumbra',

   area that receives massive synaptic barrages but has not been recruited into the ictal core.

B) The epileptic network. Several ictogenic zones (purple) are connected with synaptic

   projections. Propagation of focal seizure activity are thought to flow through those

   connected areas and may establish new ictal zones, as marked by the orange dots, through

   pathological connections.

3.2 Material & Methods

All experimental procedures were approved by either the Weill Cornell Medical College or Columbia University Animal Care and Use Committee following the National Institutes of Health guidelines. Three experimental modalities are used in this study – multielectrode array recording, wide-field calcium imaging, and two-photon calcium imaging. The corresponding experimental procedures and analyses are listed below.

3.2.1 Multielectrode array recording in 4-AP acute rodent seizure model

Animal preparation. Adult male Sprague–Dawley rats (200–350 g) were anesthetized with isoflurane in 70% N_2:30% O_2, 4% induction, and 1.5–2% maintenance. Body temperature was maintained at 37 °C with a regulated heating blanket (Harvard Apparatus, Holliston, MA). The heart rate, pO_2, and the end tidal carbon dioxide ($EtCO_2$) were carefully monitored with a small animal capnography (Surgivet, Waukesha, WI) and were sustained throughout the experiment (heart rate: 250–300 pulse/minute, $pO2 > 90\%$, $EtCO_2 \sim 25$–28 mmHg). The exposed brain was covered with cotton balls socked with artificial cerebrospinal fluid (ACSF) to preserve cortical moisture.

Array configuration. Two types of multielectrode arrays were used in this study. The first type, used for unilateral (left) hemisphere recording, was configured into a 10 by 10 grid with 400 µm interelectrode distance (Blackrock Microsystems Inc, Salt Lake City, UT). The second type, used for bilateral hemisphere recording, was configured into two separate 10 by 5 grids with 400

μm interelectrode distance. Both types of arrays were implanted into the cortex with a 0.5 mm

pneumatic implanter (Blackrock Microsystems Inc, Salt Lake City, UT)(Rousche and Normann

1992). The grids' anterior edges met the animal's somatosensory cortices (Figure 3.2A). In the

bilateral array experiment, the long side (10 electrodes) was aligned anterior-posteriorly, and

each grid was used for each hemisphere. Reference electrodes were placed subdurally, distal to

recording sites, and dynamically selected to minimize reference artifacts.

Array Signal recording. Raw electrical signal was digitally sampled at 30 kHz with 16-bit

precision (range ±8 mV, resolution 0.25 μV). Raw data was subsequently separated into two

frequency bands: multiunit activity (MUA, 500 to 3000 Hz or 300 to 3000 Hz, visually selected

for better signal-to-noise ratio, 512th order zero-phase shift, window-based FIR filter) and LFP

(500 Hz low-pass, 90th order, zero-phase shift, window-based FIR filter). The LFP band was

further down-sampled to 1 kHz. Both bands were visually reviewed. Channels with noise

amplitude (estimated as $median(|V(t)|)$/0.6745) more than 8 µV in MUA band or excessive

paroxysmal artifacts were discarded(Quiroga, Nadasdy et al. 2004).

Multiunit spike detection & firing rate estimation. Multiunit spikes were detected from the

MUA band by a threshold crossing method(Quiroga, Nadasdy et al. 2004). Each channel's

detection threshold was set to be -5 s.d. of the channel's background noise (estimated from a 2-

minute baseline recording). Detection refractory period was set to be 1 ms, to minimize

detection of multiple peaks due to noise. Channels that failed to detect more than 1 multiunit

spike per minute were also excluded.   For each channel, instantaneous multiunit firing rates

were estimated by convolving its spike train with Gaussian kernels, sampled every 1 ms(Bokil,

Andrews et al. 2010, Shimazaki and Shinomoto 2010, Smith, Liou et al. 2016). Two types of

Gaussian kernels were used in this study: a 10-ms s.d. Gaussian kernel for capturing rapid multiunit firing fluctuations and a 1-second s.d. kernel for slow change of average firing rates.

Seizure model. 4-Aminopyridine (4-AP, Sigma-Aldrich, 15 mM, 500 nL), a potassium channel blocker, was injected at the anterior edge of the array in the left somatosensory cortex, targeting 300–500 μm below the cortical surface through a glass microelectrode using a Nanoject II injector (Drummond Scientific, Broomall, PA)(Pongracz and Szente 1979, Rutecki, Lebeda et al. 1987, Avoli, de Curtis et al. 2016, de Curtis and Avoli 2016) after a 2-minute baseline recording. The 4-AP dose was increased to 1000 nL if electrographic seizures were not observed in the next 20 minutes of recording. 30 to 60 minutes after the first electrographic seizure, bicuculline methiodide (BMI, Sigma-Aldrich, 5 mM), a GABA-A receptor antagonist, was introduced either by bath application (left hemisphere) or focal injection (500nL, 300–500 μm depth at left visual cortex or right somatosensory cortex). Neural dynamics were recorded for another 30 to 60 minutes following BMI injection.

Ictal activity detection and quantification. The line-length feature of LFP was used to quantify ictal activity and facilitate systematic and objective ictal event detection(Esteller, Echauz et al. 2001, Guo, Rivero et al. 2010). For each channel, line-length was calculated for 1-second moving windows (step size: 1 ms). Periods that had more than 3 channels demonstrating greater than 3 times more line-length than the baseline and lasted for more than 5 seconds were considered as ictal event candidates, which were further visually reviewed to exclude artifacts. The onset and offset of ictal events were adjusted manually to encompass all epileptiform discharges. Furthermore, two ictal events were required to be at least 20 seconds apart temporally to be considered two isolated episodes(Ma, Zhao et al. 2009, Zhao, Ma et al. 2009,

Zhao, Nguyen et al. 2011). The periods between two consecutive ictal events are defined as interictal periods. For each ictal event, the ictal center is defined as physical location of the electrode where we detected the highest line-length.

Multiunit spike-LFP coupling. We used spike-triggered averaging to investigate the association between multiunit firing and LFP dynamics of the entire region sampled by microelectrodes (Schwartz, Pillow et al. 2006, Eissa, Tryba et al. 2016). Multiunit spikes which were detected within 1 mm from the ictal center were combined to create the spike train used for averaging.

Cross-correlation of multiunit spike trains. Cross-correlation between binned spike-trains (1 ms resolution) was used to determine the temporal relationships between any two spike trains. The timing of peak cross-correlation, $\Delta t_{a,b} = \underset{\tau}{\mathrm{argmax}}\, C_{a,b}(\tau)$, was defined as the temporal delay between two channels, a and b.

Cluster analysis of multiunit spike trains. Non-negative matrix factorization was applied to study the clustering phenomenon of ictal dynamics(Lee and Seung 1999, Hutchins, Murphy et al. 2008). During each ictal event, each channel's instantaneous multiunit firing rate was determined by convolution with a 10-ms s.d. Gaussian kernel. The resultant time series were aligned in rows and assembled into a data matrix, A, where $A_{i,j}$ is the instantaneous firing rate of channel i at time j. The matrix, A, consisting of all non-negative entries, was further factorized into two non-negative matrices, $A \approx WH$. The latent dimensionality, k, was chosen to be 2, or the number of epileptogenic drugs we injected. The interaction between the latent dynamics were further investigated using the cross-correlation method.

3.2.2 Wide field calcium imaging in 4-AP acute rodent seizure model (this paragraph is partially contributed by Dr. Hongtao Ma)

Calcium dye loading and fluorescence measurement. The calcium indicator Oregon Green 488 BAPTA-1 AM (OGB-1, Life Technologies, Grand Island, New York) was employed for recording of neural activity. Convection enhanced delivery (CED) was employed to bulk load the entire neocortex with OGB-1(Ma, Zhao et al. 2014). In brief, 50 µg of OGB-1 was diluted in 5 µL of DMSO-F127 then in 50 µL of ACSF. 8 µL of OGB-1 solution was injected in the neocortex, via a glass electrode (50-100 µm opening) placed ~1 mm below the brain surface, at the speed of 100 nL/min, using a micro-pump (WPI, Sarasota, Florida). A CCD camera (Dalsa camera in Imager 3001, Optical Imaging, Rehovot, Israel) using a tandem lens (50 × 50 mm) arrangement was focused 300–400 μm below the cortical surface. A 470±10 nm LED was employed as the illumination source for calcium-sensitive dye and illumination was directed using fiber-optic light guides. A 510 nm long-pass filter was placed before the camera to prevent calcium illumination contamination, while permitting calcium dye signal.

Calcium imaging analysis. Data were analyzed by customized MATLAB functions. Calcium images were convolved with a spatial Gaussian kernel ($\sigma = 3$ pixels) to increase signal-to-noise ratio. The signal changes were calculated as dF/F, where F was the baseline illumination when no epileptiform discharges were noticed and dF was the signal change during epileptiform activity as identified by the LFP. A 1 Hz high-pass filter was applied to the calcium imaging data to remove the calcium signal from glial cells.

A seed trace initiated correlation method(White, Bauer et al. 2011) was employed to calculate the spatial spread of neuronal activity. Briefly, a seed trace was selected from a small region of interest (ROI) from the 4-AP and BMI injection sites. The correlation coefficients between the seed trace and trace from every individual pixel in the surrounding image were calculated. A heat map was generated using the correlation coefficient (CC) at each pixel.

3.2.3 Two photon-calcium imaging in PV-Cre x GCaMP6F mice (this paragraph is contributed by Dr. Michael Wenzel)

Animal preparation, seizure model, and ictal event detection. PV-Cre mice (RRID:IMSR_JAX:017320) were crossed with LSL-GCaMP6F(Chen, Wardill et al. 2013) mice (RRID:IMSR_JAX:024105), resulting in GCaMP6F expression specifically in parvalbumin (PV) positive interneurons. Animals were anesthetized and their physiological conditions were maintained similarly to protocols described in previous sections. Two craniotomies over the left hemisphere were created – one (visual cortex) for 4-AP (15 mM, 500 nL) injection and the other (somatosensory cortex, 4 mm away from 4-AP injection site) for imaging.

Image collection. Calcium imaging of GCaMP6F positive interneurons was performed using a two-photon microscope (Bruker; Billerica, MA) and a Ti:Sapphire laser (Chameleon Ultra II; Coherent) using a 25x objective (water immersion, N.A. 1.05, Olympus). GCaMP6F was excited with a laser wavelength of 940 nm, fluorescence emission was collected through a 535nm (green) filter (Chroma, Bellows Falls, VT). Resonant galvanometer scanning and image acquisition (frame rate 30,206 fps, 512 x 512 pixels, 150-200 µm below the pial surface) were controlled by Prairie View Imaging software.

Image analysis. Regions of interest (ROIs) were registered manually to target GCaMP6F-expressing PV(+) interneurons using ImageJ (National Institute of Mental Health, Bethesda, MD.). To minimize cell signal contamination by surround neuropil fluorescence changes, we applied ROI shrinkage (Radial subtraction of 1 pixel from somatic ROI)(Hofer, Ko et al. 2011). Individual cell fluorescence was calculated as the average across all pixels within the ROI. Then, we calculated relative changes in fluorescence (F) as $\frac{\Delta F(t)}{F_0} = \frac{(F(t)-F_0)}{F_0}$, where F_0 represents the mean of the lowest 25% of values within a 500-frame window centered around each value F(t). Finally, to minimize tissue pulsation artifacts in the extracted traces, individual traces were filtered with a 2-second LOWESS smoothing envelope.

Ictal events – PV interneuron activity coupling. LFP, recorded from a glass micropipette (2-5 MΩ, AgCl wire in isotonic PBS solution) 100 µm beneath the pial surface near the 4-AP injection site, were used for ictal event detection. A reference electrode was positioned over the contralateral frontal cortex. LFP signals were amplified by a Multiclamp 700B amplifier (Axon Instruments, Sunnyvale, CA), low-pass filtered (300 Hz, Multiclamp 700B commander software, Axon Instruments), digitized at 1000 Hz (Bruker) and recorded using Prairie View Voltage Recording Software along with calcium imaging. Ictal events were inspected visually. Specific ictal onset time was determined by searching the turning point of initial negative DC-shift:

$$t_{onset} = \underset{\tau}{\operatorname{argmin}} \ddot{V}(\tau).$$

To calculate time lags between individual ictal onsets (measured by LFP within the seizure initiation site) and the respective time of local PV population recruitment at the FOV (distance to initiation site ca. 4 mm), we derived an average calcium transient of all imaged PVs in the FOV

and calculated the first derivative ('slope'). Then, we defined either the maximum slope (1st derivative) or maximum curvature (2nd derivative) of the population calcium transient during each peri-ictal onset window (centered around the time point of the electrographic seizure onset) as the time point of PV population recruitment. Eventually, the lag was calculated as $\Delta t_{seizure} = t_{calcium} - t_{LFP}$

3.3 Results

3.3.1 Focal 4-AP injection induced spatially constrained ictal events

Figure 3.2A shows the experimental setup. Injecting 15mM, 500 nL 4-AP into

somatosensory cortex of adult Sprague-Dawley rats induced focal ictal activity (Figure 3.2B-C).

LFPs with maximal line length (the ictal center) were detected at the area where 4AP was

injected (Figure 3.2B, anterior-right corner of the array). At the same region, multiunit unit

firing rate increased (Figure 3.2C). Both LFP activity and multiunit firing rates decayed with

increasing distance from the injection site, although the area showing increased multiunit firing

rate was more sharply contrasted. This indicates that the 4-AP model of focal epilepsy is well-

defined and limited to a small area adjacent to the injection site. During ictal events, similar to

human focal seizures(Merricks, Smith et al. 2015), the waveforms of multiunit spikes near the

ictal center were distorted (light blue arrows in Figure 3.2C); whereas waveforms of multiunit

spikes detected distally were preserved (yellow arrows in Figure 3.2C), indicating regional

differences. The spatial extension of the LFP activities remained spatially stable during

repetitive ictal events (Figure 3.2D). Overall, both LFP activity and multiunit firing rates

decreased with increasing distance from the 4-AP injection site in all experiments (Figure 3.2E

& 3.2F). Beyond the spatial extent of the seizure focus, LFP recordings showed increased line

length (Figure 3.2E), yet the average multiunit firing was not significantly greater than baseline

(Figure 3.2F, see legends for detailed statistics).

63

Figure 3.2 Multielectrode array recordings demonstrating focal nature of 4-AP ictal events
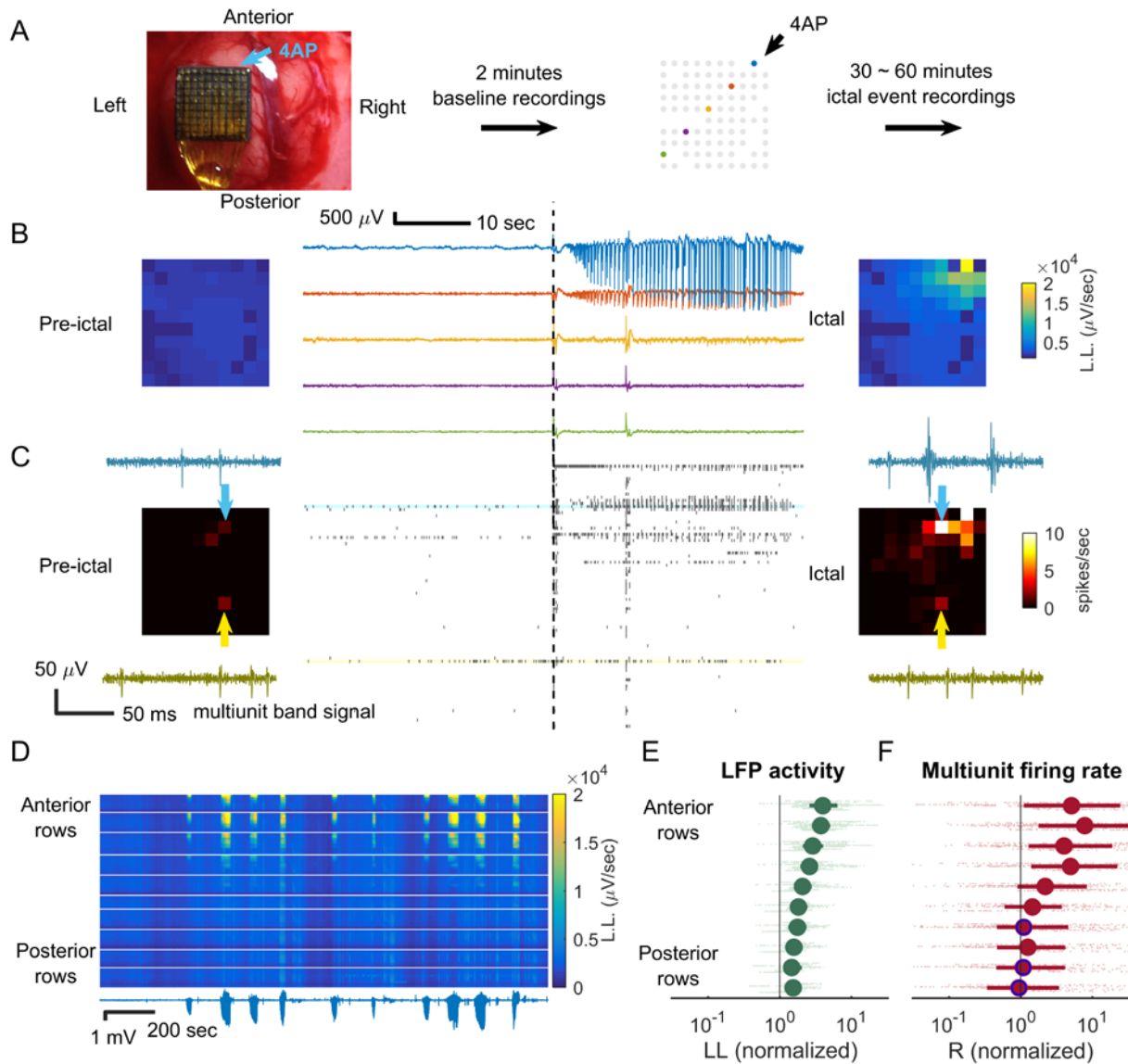
A) Experiment setup. The multielectrode array (96 electrodes, arranged in a 10 by 10 grid, with orthogonal interelectrode spacing of 400 microns) was implanted in the left hemisphere. A two-minute baseline recording was obtained.   4-AP was the injected at the anterior border (upper right corner) to induce ictal events. Missing squares denote

non-recording electrode sites. Five microelectrodes are highlighted with a color code corresponding to traces shown in ensuing panels.

B) Sample LFP recordings of pre-ictal (left) and ictal (right) periods after 4AP injection. The line length (LL) measure is used in corresponding color spectrum plots to show the spatial layout of ictal field activity. Note the focality of the event.

C) Raster plot of multiunit firing during pre-ictal (left) and ictal (right) periods. The time axis (horizontal) aligns with Panel B. Average multiunit firing rates are shown in the corresponding heat maps. The multiunit band signal of sample channels (light blue and yellow) are showed in the subpanels. Note the focality of the event.

D) Repetitive ictal events from one animal are shown. Ictal activities were similarly spatially distributed - concentrated at the anterior region sampled by the multielectrode array. Lower trace: LFP recording from the ictal center (highest line length). In the corresponding color map, each row represents one channel, arranged according to distance from the anterior edge of the microelectrode array. Activity is denoted by line-length averaged over 5 second windows.

E) Quantification of ictal activities along the anterior-posterior axis (8 animals, 150 ictal events, marker: median, error bar: interquartile range). For each ictal event, the average line-length of each channel, divided by its baseline line length, is plotted along the horizontal axis and the electrode's physical position, anterior-posteriorly, is plotted along the vertical axis. Each animal's data are plotted with minor vertical offsets to facilitate visualization. Green markers and error bars represent the electrode row-specific median and interquartile ranges of the 150 ictal events. During ictal events, LFP activities showed general increase (for each row, sign test under null hypothesis $LL_{ictal\ events} =$

$LL_{baseline}$: p<0.001) with clear anterior-posterior gradient (Spearman's correlation coefficient between a channel's anterior-posterior position and its line-length during ictal events: 0.59, 8 animals, N=8909, p $\ll$ 0.001).

F) Quantification of multiunit firing rate along the anterior-posterior axis (8 animals, 150 ictal events). Panel presentation conventions were adopted from Panel E. The anterior channels showed significant multiunit firing rate increase (sign test under null hypothesis $R_{ictal\ events} = R_{baseline}$: p<0.001) but not the posterior channels (markers with blue rims, p = 0.26, 0.07, and 0.53 from anterior to posterior respectively). Spearman's correlation coefficient again confirmed the existence of anterior-posterior gradient of (ρ=0.31, 8 animals, N=3915, p $\ll$ 0.001).

3.3.2 Wide-field calcium imaging confirmed 4AP ictal event's focal nature

Multielectrode array studies are limited in spatial sampling (4 by 4 mm) and resolution (400 microns). To overcome these limitations, we used wide-field calcium imaging to obtain a comprehensive, high-resolution spatial map of neural activity during ictal events (Figure 3.3A-C). Wide-field calcium imaging revealed a similar focal onset and limited spread of calcium activity around the area of the 4-AP injection (Figure 3.3B). A sharp demarcation of neural activity occurred roughly 2-3 mm from the injection site, providing a real-time map of the evolving ictal focus (Figure 3.3D). Notice here we injected 4-AP in visual cortex instead of somatosensory cortex, which confirmed 4-AP ictal event's focal nature is regionally invariant.

Figure 3.3 Wide field calcium imaging confirmed focal nature of 4AP ictal events.

(Contributed by Dr. Hongtao Ma)
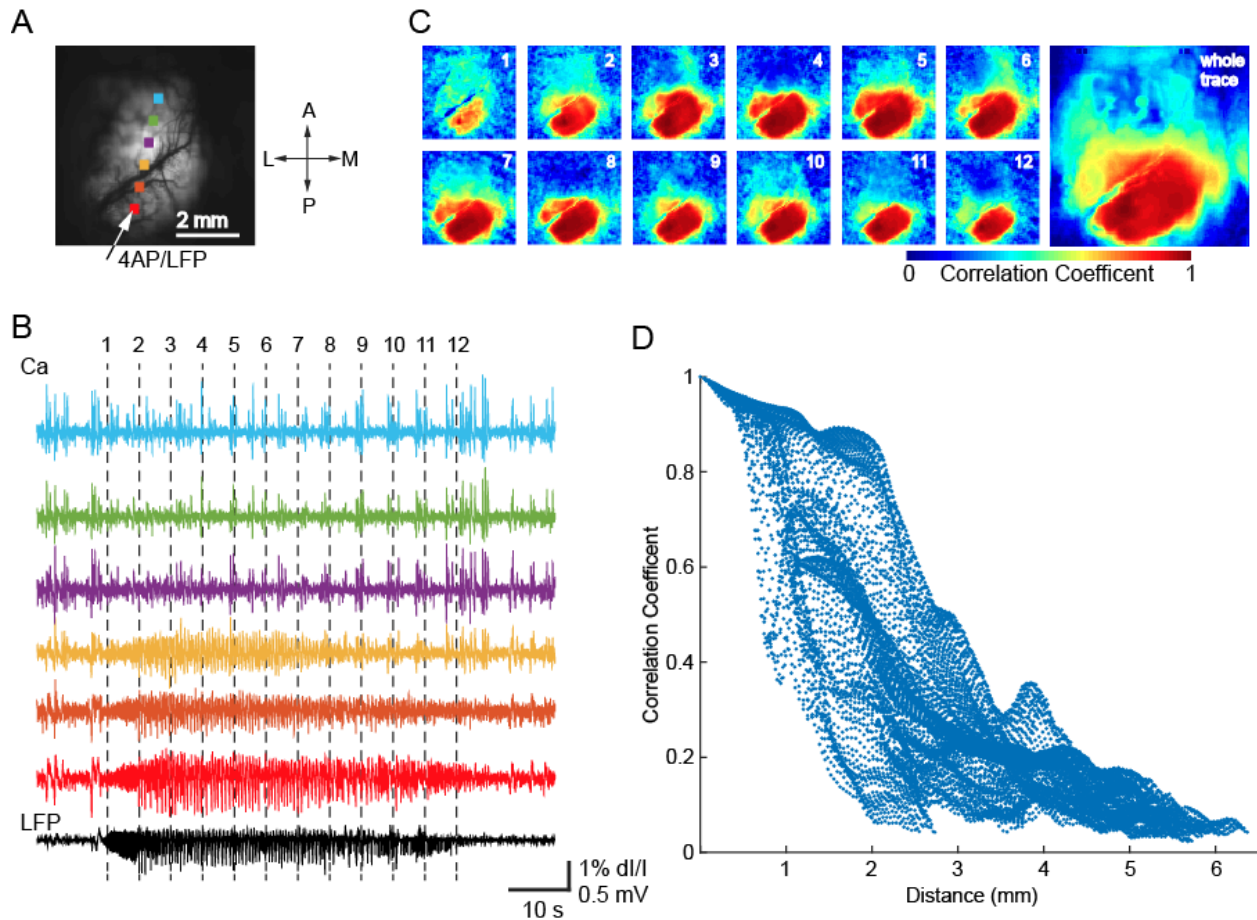
A) The field of view. The arrow at the bottom left corner shows the location of 4AP/LFP electrode. Six color dots show the locations of the regions of interest (ROIs) where the calcium traces are shown in Panel B.

B) The LFP (black, bottom trace) and calcium fluorescence (colored traces above, 1 Hz high pass) during an ictal event. 12 vertical dotted line showed 12 different time points during the ictal event evolution, which are used to generate the maps in Panel C. Notice the bottom 3 traces (proximal) show a similar waveform as the LFP recording; whereas the

top 3 traces (distal) showed intermittent bursting neural activity that were dissociated from the LFP.

C) The spatiotemporal evolution of the calcium activity during an ictal event. Left: The color maps showed the seed-initiated correlation coefficient maps during 12 different time points. Note the focal onset and limited spread of the calcium signal with high correlation coefficient around the 4-AP electrode, supporting the focal nature of 4-AP ictal events. Right: The color map of seed initiated correlation coefficient map of the whole trace.

D) Graph of the Pearson correlation coefficient between each pixel's calcium fluorescence and the LFP tracing based on the distance of each pixel from the location of the LFP electrode. Note a sharp decreased of calcium signal that occurs around 2-3 mm from the 4AP injection.

3.3.3 Hemisphere-wide, distance-dependent LFP responses

The focal nature of 4-AP ictal events provided the opportunity to investigate neural responses at various distances from the focus. During 4-AP ictal events, multiunit firing near the ictal center (≤1 mm) was associated with LFP fluctuations both locally and distally (Figure 3.4A). Spike-triggered averaging (Figure 3.4B) demonstrated distance dependence with respect to polarity and temporal delay. Electrodes proximal to the ictal center ($\leq 1mm$) showed large negative LFP deflections which peaked shortly after multiunit firing bursts (Figure 3.4B, blue traces; median peak times: 4.3 ms, interquartile range: 3.5 to 5.4 ms; Figure 3.4C, blue arrows). Distally (> 4mm), there were positive deflections with prolonged delays (Figure 3.4B, green traces; median peak times: 17.6 ms, interquartile range: 14.9 to 18.9 ms; Figure 3.4C, red arrows). The distance-dependent polarity switch (Figure 3.4D, left subpanel, blue to red arrows) and temporal delay (Figure 3.4D, right subpanel, blue to red arrows) were observed across experiments (8 animals, 150 ictal events).

Figure 3.4 Multiunit activities inside the ictal focus were associated with hemisphere-scale, distance-dependent LFP responses.
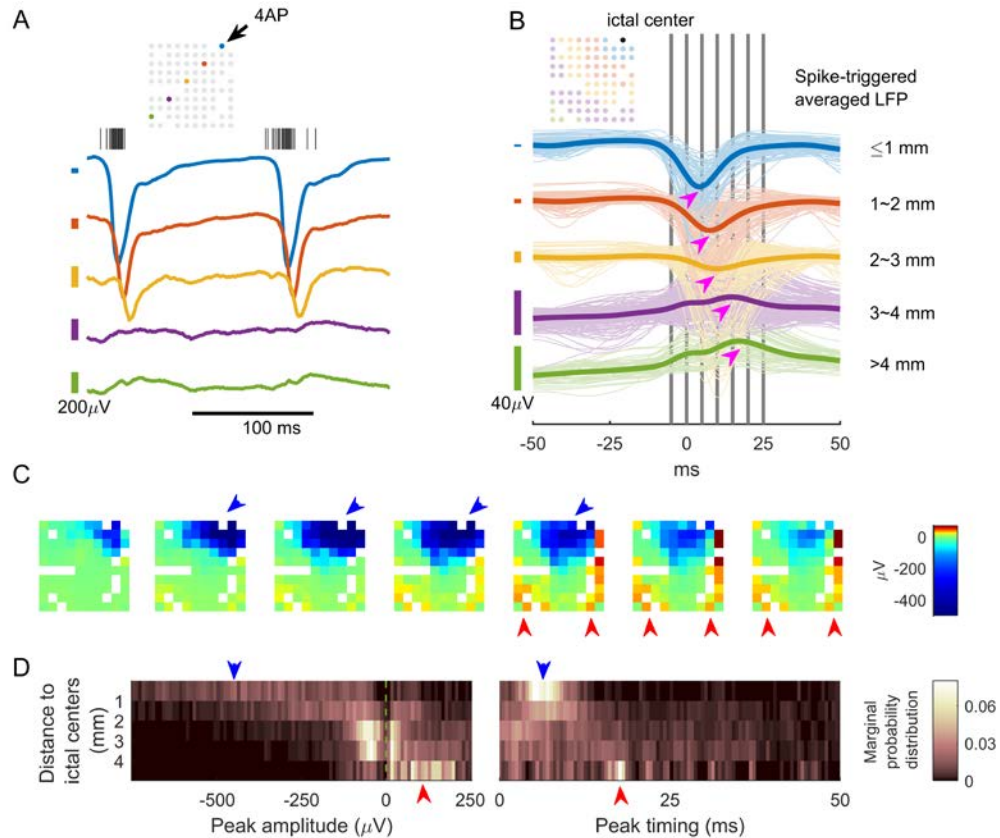
A) Sample LFP traces with ictal multiunit activity. Traces are scaled according to the vertical scale bars at the left side. The centers of the scale bar are the isoelectric points for traces that have the same color. The LFP trace colors indicate where they were recorded from, as shown in the array schematic.

B) Spike-triggered LFP in one animal, averaged over 11 ictal events. Colors are used to mark LFP traces' distance from the ictal center. The thick lines are the average of traces with similar colors. Notice the sequential increase of temporal delay of peak response and the switch of polarity (magenta arrows) as distance increases. Blue traces median temporal delay, measured as the timing of the negative peaks: 4.3 ms (3.5 to 5.4 ms, n =

88). Green traces median temporal delay, measured as the timing of the positive peaks: 17.6 ms (14.9 to 18.9 ms, n = 55). U-test comparing the median between the two groups showed $p \ll 0.001$. Vertical gray bars are used to indicate the timing of the frames in Panel C.

C) The spatiotemporal evolution of spike-triggered averaged LFP. Each frame's time is indicated by Panel B's vertical gray bars from left to right sequentially. Large negative LFP deflections were found near the ictal center (blue arrows) whereas positive LFP deflections were found distal to the ictal center, and with increased/different temporal delay (red arrows).

D) Summary of spike-triggered averaging studies in 8 animals, 150 ictal events. For each channel during each ictal event, the spike-triggered LFP's global extremum (where the signal deviated from isoelectric point the most) was recorded. The search range for global extrema was limited within the causal part of the signal (0 to +50 ms). Data were grouped by distance and their extrema's distribution were shown in the heat maps (N = 1131, 1506, 2263, 1515, and 346 from proximal to distal groups). Left subpanel: distribution of extrema value, notice the switch of polarity (Probability of detecting a negative peak = 0.93*, 0.75*, 0.58*, 0.45, 0.14*, sign test, α=0.05). Right subpanel: distribution of peak timing, notice the temporal delay (median: 6.9, 8.7, 10, 14.9, 17.5 ms, Kruskal–Wallis test $p < 0.001$).

3.3.4 Parvalbumin(+) interneurons may contribute to surround inhibition effects (contributed by

Dr. Michael Wenzel)

We therefore confirmed that focal ictal events exert widespread, hemisphere-scale effects,

reflected in the associated LFP fluctuations. The observations of widespread, hemisphere-scale

LFP effects and the proximal-distal polarity flip led us to hypothesize that ictal activities exert

qualitatively opposite effects in distal compared to proximal neural tissues, and that the distal

effect is inhibition-dominant(Marshall, Li et al. 2016).   The greater distal temporal delay

suggests that a multi-synaptic pathway is involved, consistent with feedforward inhibition. To

test this hypothesis, we employed in vivo 2-photon calcium imaging to record the activity of

parvalbumin (PV) positive interneurons in the distal surrounding tissue during ictal events

(Figure 3.5). We selected PV(+) interneurons because of their strong inhibitory effect on

pyramidal neurons through proximal dendrite and soma projections(Markram, Toledo-Rodriguez

et al. 2004, Kepecs and Fishell 2014). Also, PV(+) interneurons have been reported to restrain

ictal propagation in acute brain slices(Cammarota, Losi et al. 2013, Sessolo, Marcon et al. 2015).

Upon 4-AP injection at visual cortices (to test regional invariance), the ictal events reliably

activated PV(+) interneurons in distal region (4mm away from injection site, Figure 3.5B-D).

The recruitment of distal PV(+) interneurons to electrographic ictal events occurred with little

temporal delay (Figure 3.5E-F, see legends for detailed statistics). The rapid response indicated

that PV(+) interneurons are activated through synaptic transmission instead of slow processes

such as extracellular ion diffusion. Overall, the observation of rapid PV(+) interneuron

activation supported our hypothesis that ictal events exert net inhibitory effects on surrounding

tissues.

Figure 3.5 In vivo two-photon sub-population calcium imaging shows rapid recruitment of distal PV(+) interneurons to ictal events. (Contributed by Dr. Michael Wenzel)
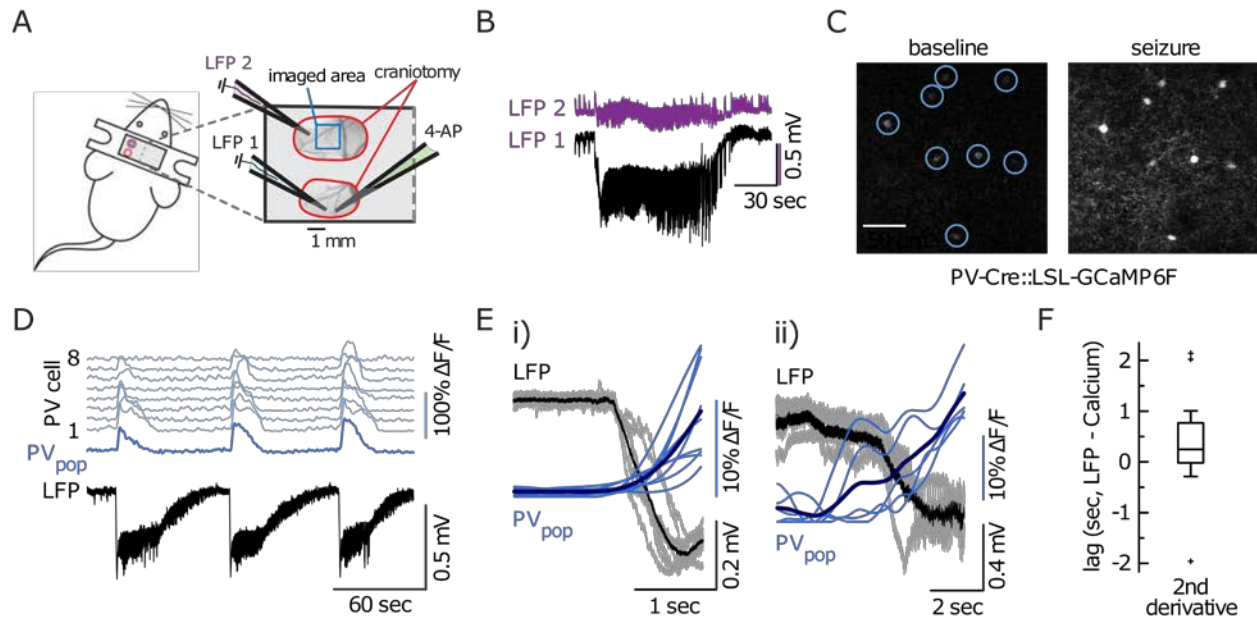
A) Experimental setup: Two craniotomies over left somatosensory and visual cortex, respectively; each craniotomy is encircled in red; imaging field of view (FOV) outlined in blue. In addition to PV(+) subpopulation imaging, experiments involved the insertion of either two or three glass micropipettes: one pipette containing 4-AP (green, 15mM, injection volume 500 nL), and one (injection site [LFP 1, light blue]) or two (injection site [LFP 1, light blue] plus imaging site [LFP 2, purple]) pipettes each containing a silver chloride silver for LFP recordings.

B) Two simultaneous LFP recordings (LFP 2 [purple] close by the imaging area, LFP 1 [black] proximal to 4-AP injection site). In line with experiments carried out in rats, there is a drastic reduction in amplitude and loss of DC-shift at the distal LFP electrode (inter-electrode distance ca. 4mm).

C) Representative 3 second average calcium images depicting 8 distal PVs during baseline (left) and during ictal onset (right). The increase in calcium is visible to the naked eye.

D) Calcium transients of the 8 PVs depicted in Panel C. Individual cells in light blue (top 8 traces), population average in dark blue. Simultaneous LFP recording near the 4AP injection site. Notice the consistent population recruitment across three consecutive ictal events.

E) Superposition of all electrographic ictal onsets and corresponding PV population calcium transients (blue, mean in dark blue) in two independent experiments (i=9 ictal events, ii=5 ictal events). Note the systematic relationship between the paroxysmal DC-shift in the LFP (ictal onset) and a clear rise in the PV population calcium signal.

F) Quantification of temporal PV population recruitment lag (distance to ictal initiation site ca. 4mm). PV onset time points were defined by maximum 2nd derivative of the calcium signal within the peri-ictal onset time window (which was determined electrographically). Box plot box depicts 25 – 75 %ile, horizontal bar within box represents the median (248.47 msec, interquartile range 786.44 msec; 2 animals, 14 ictal events). Outlier values are displayed as +.

3.3.5 Globally compromising inhibition causes contiguous ictal invasion

We subsequently tested the hypothesis that feedforward inhibition in the surrounding cortex is essential for preventing ictal propagation *in vivo*. We focused on pathways mediated by GABA-A conductance because of the short temporal delay shown in spike-triggered LFP studies is most consistent with GABA-A synaptic delay(Lopantsev and Avoli 1998, Uva, Librizzi et al. 2005, Avoli and de Curtis 2011, Pouille, Watkinson et al. 2013). To reduce GABA-A conductance, we first bathed the whole cranial window with 5mM bicuculline (BMI, a GABA-A receptor antagonist). As the BMI penetrated into the cortex, we observed that ictal events, originally well localized near the injection site (the first 3 events in Figure 3.6A-B, anterior-right corners), started to propagate outward (the later 3 events in Figure 3.6A-B, summarized in Figure 3.6C). By five minutes after BMI application (the right most episode), the ictal activity had invaded the entire area sampled by the microelectrode array. Notably, the morphology of the low-frequency LFP remained similar to the ictal events generated by 4-AP alone, as opposed to events triggered by focal BMI, which produces very high amplitude paroxysmal epileptiform discharges (Ma, Wu et al. 2004, Ma, Zhao et al. 2009, Geneslaw, Zhao et al. 2011) (also see later figures). Global BMI application also changed the multiunit activity pattern (Figure 3.6D). After BMI application, recording sites distant from the 4-AP injection site (lower rows of the raster plot), previously quiescent during ictal events, started to fire intensely during the ictal events but not between events. The pace of recruitment increased over time (green versus magenta box in Figure 3.6D; Figure 3.6E, left panel). The sequential detection of multiunit spikes confirmed the ictal activity originated from the focus (Figure 3.6E, right panel) and formed traveling waves spreading (Figure 3.6F) from the 4-AP injection site. In line with previous reports of ictal traveling waves in disinhibited rodent cortex(Chagnac-Amitai and Connors 1989, Pinto, Patrick

et al. 2005, Trevelyan, Baldeweg et al. 2007), cross correlation of spike trains showed the average speed of the outward traveling waves was 63 mm/sec (Figure 3.6G-I, 95% confidence interval: 61.6 to 64.4 mm/sec).

Figure 3.6 Globally reducing inhibition strength cause contiguous ictal invasion
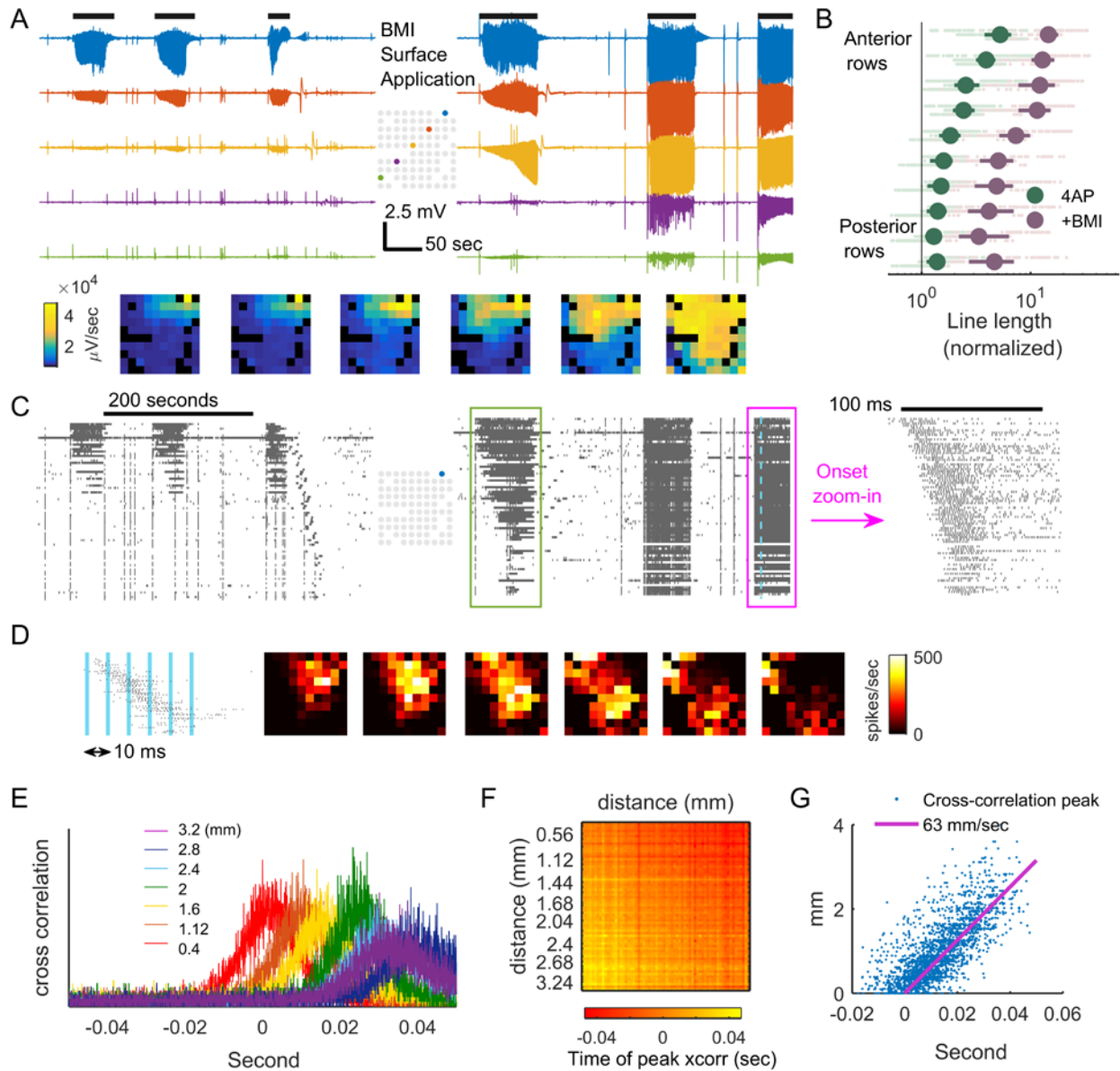
A) LFPs before (left) and after (right) BMI surface application. Horizontal black bars (upper

part of the panel) indicate ictal periods. The spatial distributions of ictal activities during

the 6 ictal events, measured in line-length, are shown in frames below sequentially.

B) Comparison of ictal activity (line length) before versus after BMI application. The

panel's conventions are analogous to Figure 3.2E. Each light green and red dot

represents data from one channel during one ictal event. Spearman correlation

coefficient between a channel's position anterior-posteriorly and its line-length during

ictal events after BMI application: 0.61. (3 animals, N = 1221, p << 0.001)

C) Multiunit activity before (left) and after (right) BMI surface application. Time is aligned

with Panel A. Data are sorted so that the upper rows of the raster plot correspond to

channels that are closer to the ictal center (blue electrode of the inlet map) and the lower

rows correspond to distal channels. Green box: the first ictal event after BMI application.

Notice the sequential recruitment of neurons from the 4-AP ictal center to distal areas.

The ictal event marked with magenta box is zoomed in. Notice the onset of the ictal

event with sequential recruitment from the 4-AP injection site, albeit at higher speed than

the one in the green box.

D) The spatiotemporal evolution of a sample multiunit burst during an ictal event. The blue

vertical bars indicate the timing of each frame. Notice the spread of the traveling wave

pattern radiating from the 4-AP ictal center.

E) Cross-correlogram of the spike train recorded from the 4-AP ictal center to other

channels during all ictal events (5 events) after BMI application. The colors indicate the

distance between the channel's distance from the 4-AP ictal center.

F) The results of pairwise cross-correlation. For each channel pair, horizontal and vertical

coordinates indicate each of the two channels' distance from the 4AP ictal center. Times

of peak cross-correlation are indicated by color. Only channels that have shown a stable

high average multiunit firing rate > 5 spike/sec are included here (66 channels).

G) Linear regression of data from Panel H. Linear regression model: $d_i - d_j = V * (t_i - t_j)$,

where i & j are channel indices, d is the distance from the 4AP ictal center, and V is

speed. Least squares regression shows V = 63 mm/sec, F-test p << 0.001, adjusted R-squared = 0.648 (66 channels, 2145 pairs).

3.3.6 Focally compromising inhibition revealed long range propagation pathways

The observations of a distant (> 4mm) LFP signal (Figure 3.2B, 3.2E, Figure 3.4) as well as triggered PV(+) interneuron activation activity (Figure 3.5) suggested a long-range excitation pathway that extended further than the ictal zone's multiunit bursting and correlated calcium activity. We sought to investigate this further using a solitary, distant, focal BMI injection (5 mM, 500 nL). After establishing the 4-AP ictal focus, injecting BMI at the diagonal corner (the maximal distance our multielectrode array could record, i.e. $4\sqrt{2}$ mm) resulted in propagation of ictal activity toward the site of the BMI injection (Figures 3.7A). In this animal (21 ictal events), we were able to discern two physically separate but temporally linked foci (Figure 3.7A, magenta box). Early during the sample ictal event (magenta box), the cortical territory between the two foci did not demonstrate multiunit bursting, indicating that they were not recruited into either seizure focus (Figure 3.7B, early frames). Instead, recruitment proceeded antidromically (posterior to anterior) with an average speed of 0.19 mm/sec (95% confidence interval: 0.17 to 0.21 mm/sec, 21 ictal events). The antidromic recruitment indicated that the BMI foci constituted a second ictal core instead of simply mirroring projections from the 4-AP ictal focus. The skipped, physically non-contiguous propagation pattern confirmed the existence of a long-range, epileptogenic excitatory pathway.

Figure 3.7 Existence of long-range ictal propagation pathway
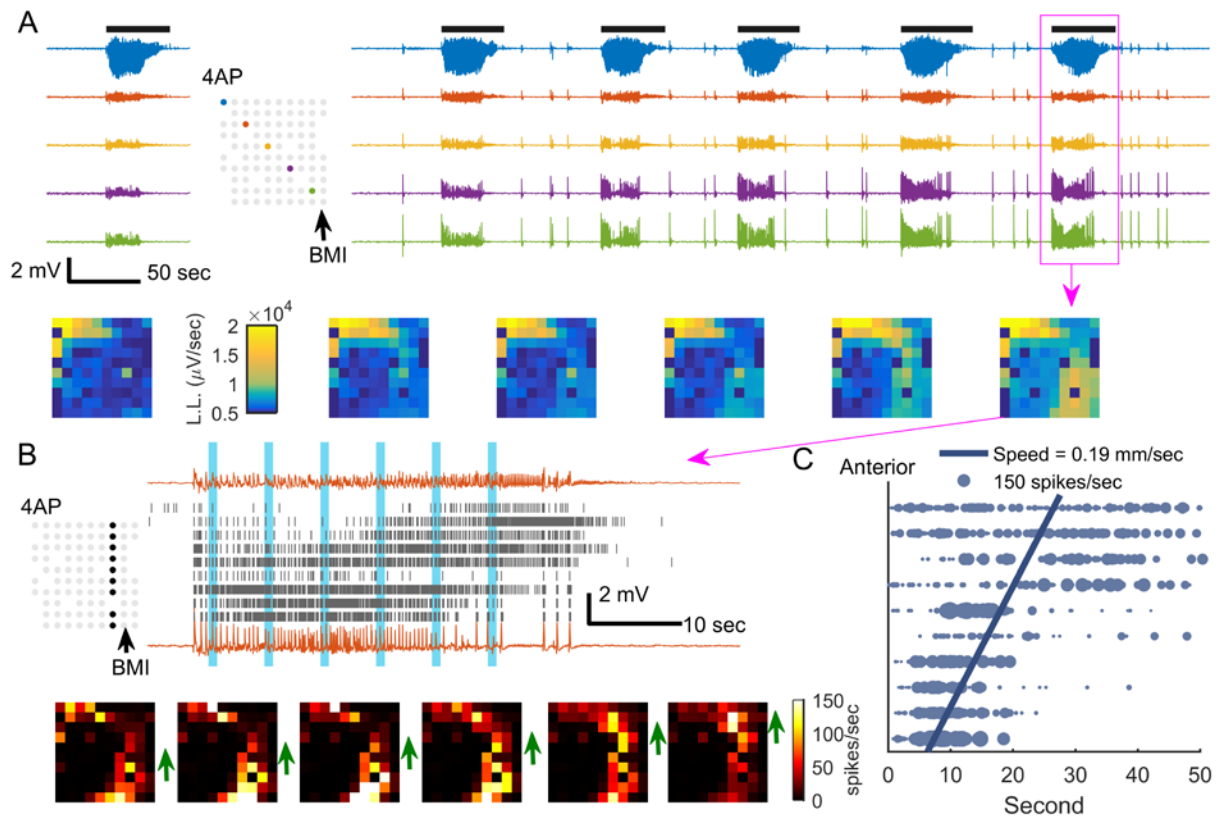
A) LFPs before (left) and after (right) BMI injection. Figure conventions are adopted from Figure 3.6A. Note that the ictal event at the BMI site is temporally linked with the 4-AP event but with quite a different electrographic morphology. Spatial distribution of ictal activities of each ictal event is shown in the frames sequentially. L.L.: line-length. Notice the two physically separate ictal foci.

B) Multiunit activity during the ictal event marked with a magenta box in Panel A. Each row of the raster was recorded from the electrode whose physical position is marked in the inlet map (upper: anterior electrodes; lower: posterior electrodes). The upper and lower traces are the LFP recorded from the most anterior and the most posterior electrodes of the marked electrode column respectively. Spatiotemporal evolution of

82

multiunit firing rates (1 sec Gaussian kernel for capturing expansion of ictal cores) are

showed in the frames whose timing are indicated by the vertical blue bars at the raster

plot. Green arrows indicate the propagation direction of multiunit activity.

C) Statistical analysis of anterior-posterior propagation of 4-AP ictal events after BMI

injection. The horizontal coordinates indicate when a channel achieved its maximal

firing rate (1 sec Gaussian kernel), and the vertical coordinates indicate its physical

position anterior-posteriorly. Each datum was plotted with a size that is proportional to

its maximum firing rate. Data from different animals are plotted with minor vertical

offsets. Linear regression model: $t = \beta_0 + \beta_1 x$. N=846, 1 animal, 21 ictal events, 95%

confidence interval: 0.17 to 0.21 mm/sec, F-test p $\ll$ 0.001, Adjusted R-squared = 0.343.

3.3.7 Multifocal integration and epileptic network formation

We next investigated interactions between the two separate ictal foci (Figure 3.7). Non-negative matrix factorization, an unsupervised clustering algorithm, demonstrated that two clusters of neuronal activity existed during the ictal events (1 animal, 21 ictal events, median residual squared error: 44%, interquartile range: 42.5 to 46.6%); each cluster had its spatial distribution near the 4-AP or BMI injection sites respectively (Figure 3.8A left subpanels). The 4-AP-cluster's neuronal dynamics (orange trace) showed complex interactions with the BMI-cluster (blue trace) – neuronal bursts at the BMI-cluster were able to trigger firing at the 4-AP cluster (blue box, right subpanels) and vice versa (red box). This 'ping-pong' effect had a short temporal delay, and the interaction of the two clusters occurred in both directions (Figure 3.8B). This may be described as an epileptic network with two physically separable nodes communicating along existing bidirectional excitatory pathways. The short signal delay between the two foci, 14 (red arrow) and 19 ms (blue arrow) respectively, is compatible with the delay time caused by an oligo-synaptic pathway.

Seizures with two dynamically distinct foci could also be observed by wide field calcium imaging. Using a similar experimental set-up, wide field calcium imaging demonstrated the existence of two dynamically distinct, yet linked foci. Although ictal events initiated at the same time, calcium dynamics only correlated with the immediately adjacent area corresponding with 2-3 mm focus (Figure 3.8C-D).

Figure 3.8 Multifocal ictal zones form connected epileptic network
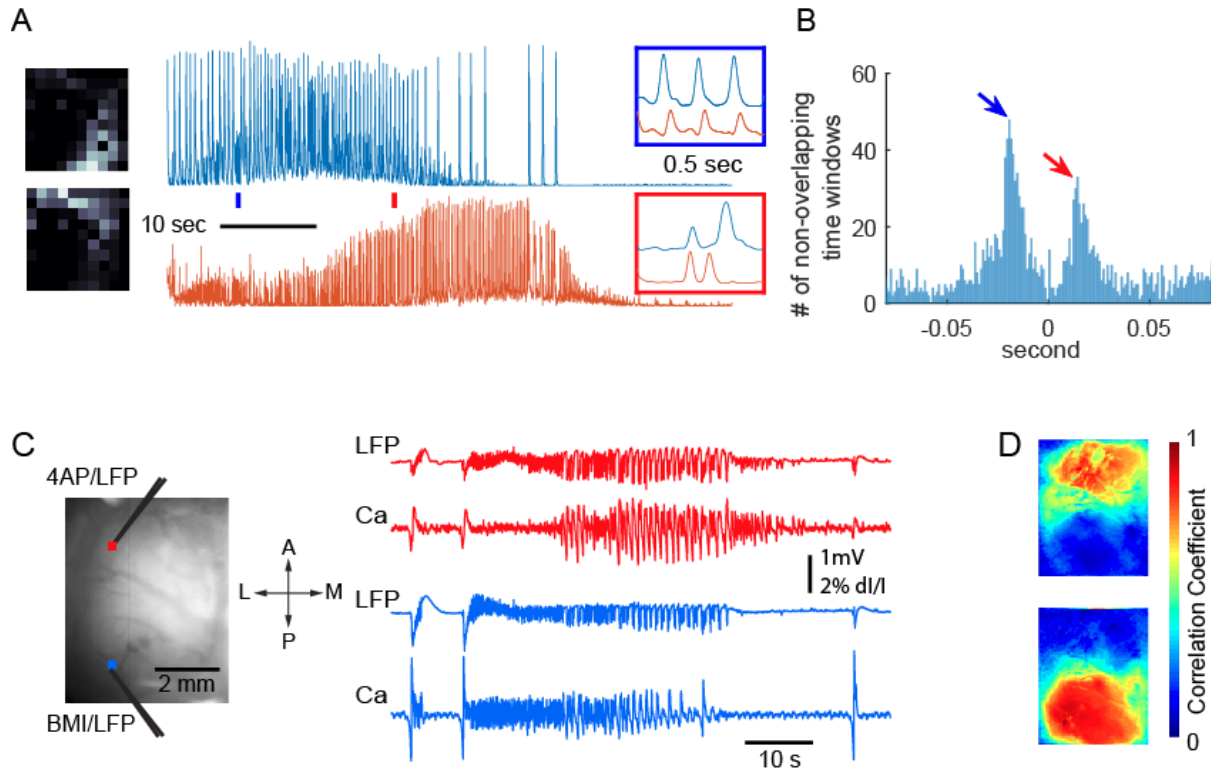
A) Factorization of neuronal dynamics. Multiunit spiking rates were estimated by 10 ms Gaussian kernel convolution every 1 ms. The resultant multivariate time series were factorized by non-negative matrix factorization (latent dimensionality = 2, residual Frobenius norm divided by the original matrix norm: 44%, interquartile range: 42.5 to 46.6%) Left panels: the distribution of the two non-negative factors (21 ictal events, 1037 seconds). Right traces: the temporal evolution of the weights of the two models during the sample event (the magenta box). The horizontal axis aligns with Panel C. The blue & red short segments are further zoomed in (inlet boxes) to illustrate the ping-pong dynamics. The blue box shows the blue factor temporally leads the red factor (BMI to 4AP corner); whereas the red box shows the opposite.

B) Cross-correlation study shows ping-pong dynamics. The multivariate time series calculated from Panel A were broken down into 2074 non-overlapping time windows (0.5 second each). The distribution of peak correlation times of miniepisodes are plotted. Notice the bimodal-like distribution of peak correlation times (red & blue arrows: -19 ms & 14 ms).

C) Wide field imaging of similar two focus experimental set-up. Left, the field of view, showing the location of 4-AP (red) and BMI (green) injection sites. Right, the LFP (top) and Ca signals (bottom, taken from ROI near electrode) recorded from 4-AP and BMI injection sites, respectively. Note that although the seizure onsets are temporally linked in that they start at the same time, the evolution of morphology of the ictal waveform is quite different as recorded both with the LFP and the calcium imaging.

D) The seed initiated correlation coefficient maps. Top: The seed trace is the Ca signal recorded from an ROI adjacent to the 4-AP injection site. Bottom: The seed trace is the Ca signal recorded from an ROI adjacent to the BMI injection site. Note, two distinct ictal foci are spatially separated indicating that each focus is distinct.

3.3.8 Cross-callosal projections

Finally, we investigated whether the same network dynamics could be served by cross-callosal synaptic projections, by creating an area of focal disinhibition in the contralateral hemisphere. A 4-AP ictal focus was created in left somatosensory cortex, and BMI was injected in the contralateral (right) homotopic region. As expected, 4-AP ictal events emerged ipsilaterally while focal interictal spikes were observed at the contralateral site (Figure 3.9A). Ictal events did not propagate to the contralateral hemisphere, with no difference in contralateral LFP activity between ictal and interictal periods (Figure 3.9B) (p=0.805, 2 animals, 17 ictal events, 680 data points). Similarly, there was no consistent increase in average multiunit firing rates in the contralateral cortices during ictal periods in comparison to interictal periods ($p = 0.98$, Figure 3.9C-D). This finding was also supported by wide field calcium imaging (Figure 3.9E-F). Calcium fluorescence dynamics in the contralateral hemisphere showed little correlation to the 4-AP ictal focus (correlation coefficients: 0.068 ± 0.229, n = 7 rats). These results indicate that cross callosal projections are not capable of recruiting and synchronizing a second focus to create an epileptic network acutely (Figure 3.9F).

Figure 3.9 Injecting BMI at contralateral hemisphere cortices did not cause ictal propagation
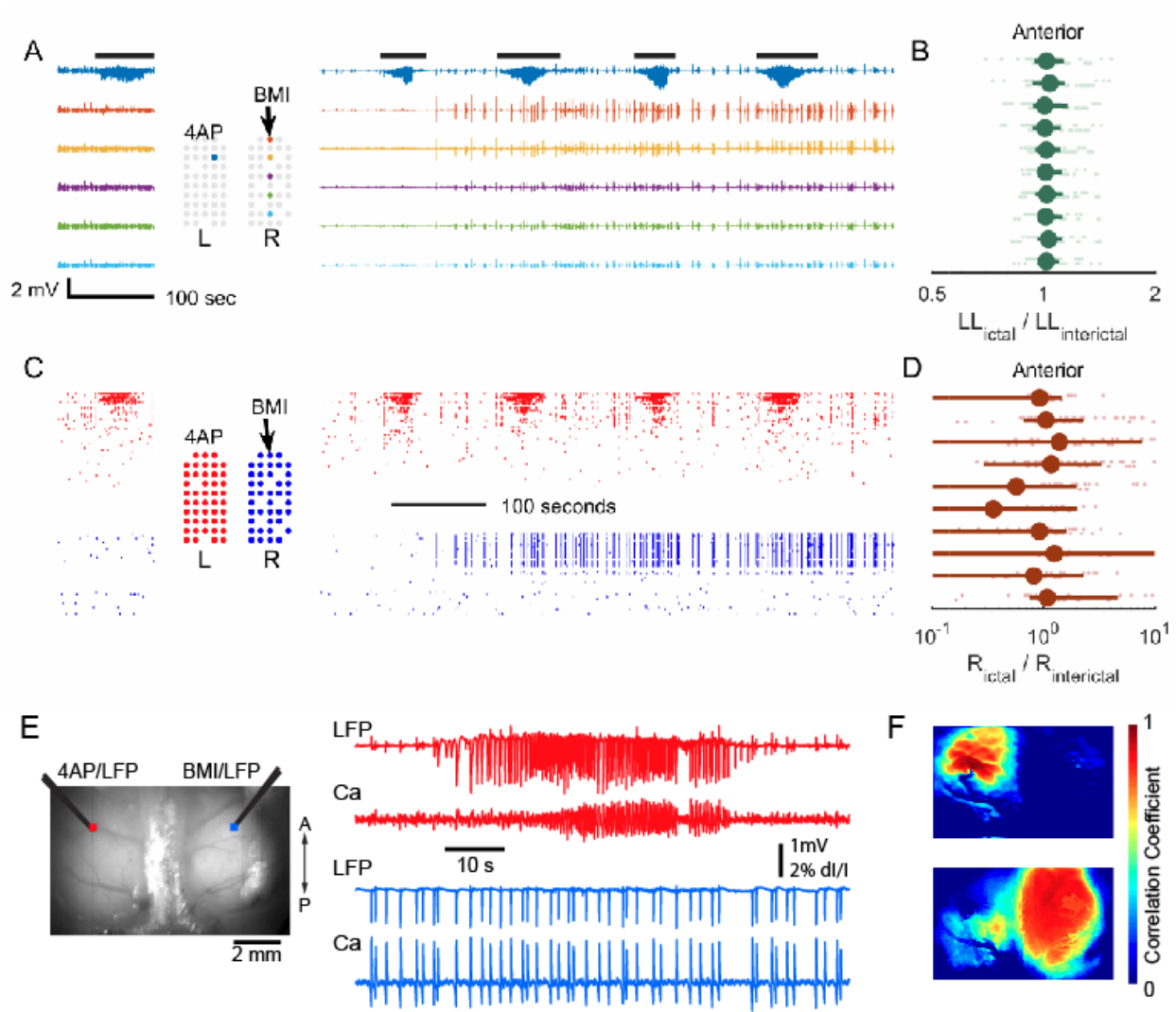
A) 4-AP is injected to create a seizure focus in the left hemisphere. LFP before (left) and after (right) BMI injection in the contralateral homotopic cortex. After BMI injection, paroxysmal interictal spikes were seen; however, a second ictal focus did not develop.

B) Comparison of line-length features during ictal versus interictal periods. For each channel during each ictal event, its line length was compared to the following interictal

period. A light green dot represents the analysis of one ictal event from one channel.
Data from different animals (N = 2) are plotted with minor vertical offsets for
visualization. Dark green dots represent medians and green bars indicate interquartile
ranges. Median $\frac{LL_{ictal}}{LL_{interictal}}$ = 1.02, sign test under null hypothesis $LL_{ictal} = LL_{interictal}$, p
= 0.805.

C) Multiunit raster plot before (left) and after (right) BMI injection. Time is aligned with
Panel A.

D) Firing rate comparison between ictal versus interictal periods, analogous to Panel B. R
stands for average multiunit firing rate. Data were plotted similar to Panel B. Median
$\frac{R_{ictal}}{R_{interictal}}$ = 1.02, sign test under null hypothesis $R_{ictal} = R_{interictal}$ 1, p = 0.98.

E) Wide field calcium imaging of 4-AP ictal focus in the left hemisphere and focal
disinhibition with BMI injected at the contralateral homotopic cortex. Left: the field of
view showing the injection sites. Right: The LFP and calcium fluorescence signal
recorded from 4AP (top) and BMI(bottom) injection sites. The ictal events do not
propagate to the contralateral side and the BMI injection results in focal interictal spikes
without creating a new interconnected ictal focus.

F) The seed initiated correlation coefficient maps. Top: the seed trace used was taken from
an ROI adjacent to the 4-AP injection site. Bottom: the seed trace used was taken from
an ROI adjacent to the BMI injection site. The ictal even remains focal and does not
involve the other hemisphere. The disinhibited interictal spiking zone is widespread and
completely independent from the seizure focus.

3.4 Discussion

We investigated local and distant neural responses to focal neocortical ictal events in an acute pharmacologically-induced seizure model. Recording data from both two-dimensional microelectrode arrays and calcium imaging confirmed the existence of multifocal ictal events and strong, widespread, long-range excitatory projections. Ictal events triggered by focal application of 4-AP remained confined to a small cortical territory, but displayed various propagation patterns when BMI was added focally or globally from the 4-AP site. The observed spread patterns and temporal delays of ictal discharges were consistent with activation of long-range excitatory synaptic pathways in the ipsilateral hemisphere, through which the success of seizure transmission depends on impairment of the GABA-A mediated inhibitory restraint. In some cases, the procedure created a two-node "epileptic network" with physically disparate seizure foci. These data indicate that long-range seizure spread may coexist with the classical model of contiguous cortical Jacksonian propagation, both involving the breakdown of inhibitory restraint. Further, the coupling of the two foci occurred in normal brain and in an acute model, implying that pathological structural alterations are not required for this to occur.

Previously, we characterized brain areas where principle neurons demonstrate intense, synchronized burst firing (i.e. clonic firing) temporally locked to synaptic deflections as the "ictal core"(Schevon, Weiss et al. 2012). This region is sharply demarcated and bounded by a narrow band characterized by asynchronous high firing rates (i.e. tonic firing) that we termed the ictal wavefront, and that is the seizure's main driving force(Smith, Liou et al. 2016). Regions outside the ictal core that are not directly participating in the seizure, but still receive significant, potentially ictogenic excitatory projections from it, are termed the "ictal penumbra". Synaptic

90

activity in the penumbra is time-locked to that in the ictal core, consisting of a mixture of excitatory and inhibitory field potentials, with pyramidal cell firing restrained by the inhibitory veto. This results in relatively sparse, heterogeneous firing that is generally not phase-locked to the low-frequency LFP(Truccolo, Donoghue et al. 2011, Schevon, Weiss et al. 2012, Weiss, Banks et al. 2013). Thus, in normally functioning penumbra, the effects of strong widespread excitation are masked by local inhibitory responses. A similar phenomenon occurs in the 4-AP model and when local inhibition is compromised, long-range excitation is sufficient to trigger a new ictal focus at a distant location. Thus, the ictal penumbra may be considered similarly to its counterpart in the stroke literature, as a brain region influenced by the ongoing seizure and at risk of seizure invasion. In our acute rodent neocortical model, this brain region widely includes the ipsilateral hemisphere but not the contralateral hemisphere.

We found the two topologically distinct seizure propagation patterns can arise from a similar process of inhibition breakdown; however, the physiological mechanisms may differ subtly. At the juxta-ictal core region, both synaptic as well as extracellular mechanisms, i.e. potassium diffusion and field effects, may contribute to the breakdown of inhibition(Pumain, Menini et al. 1985, Bikson, Fox et al. 2003, Park and Durand 2006, Frohlich, Bazhenov et al. 2008, Mylvaganam, Ramani et al. 2014, Zhang, Ladas et al. 2014), resulting in classical Jacksonian march-like propagation(Schevon, Weiss et al. 2012). In contrast, inhibition compromise at a distal site may be attributed to synaptic mechanisms, such as intracellular chloride accumulation(Huberfeld, Wittner et al. 2007, Barmashenko, Hefft et al. 2011, Lillis, Kramer et al. 2012, Buchin, Chizhov et al. 2016), synchronization(Lehnertz, Bialonski et al. 2009, Jiruska, de Curtis et al. 2013), or regional variation of inhibition robustness. Further research about physiological mechanisms that lead to inhibition breakdown is required.

91

We selected the 4-AP model(Szente and Pongracz 1979, Szente and Baranyi 1987, Ma, Zhao et al. 2009, Zhao, Ma et al. 2009, Zhao, Nguyen et al. 2011, Ma, Zhao et al. 2013, Zhao, McGarry et al. 2015) due to its ability to trigger a well-defined, spatially limited (~2-3 mm diameter) neocortical ictal discharge, mimicking the LFP appearance of human neocortical seizures. We demonstrated that the region of actively spiking cells is remarkably focal and it remains focal throughout the evolution of the seizure, as long as the surrounding inhibitory mechanisms are intact. We observed that the penumbral responses to the 4-AP focus are similar to those observed in the zero Mg mouse model(Trevelyan, Sussillo et al. 2006, Trevelyan, Sussillo et al. 2007, Trevelyan 2009) as well as during spontaneous human seizures(Schevon, Weiss et al. 2012) (Schevon et al 2012). However, the 4-AP ictal focus expanded only minimally when that agent was used alone. This focality permitted us to place the BMI site at varying fixed distances in order to assess long-range interactions between the core and surrounding areas.   In a chronic model, the site of seizure origination is less well defined, and cortical propagation is likely to occur spontaneously without a pharmacologically-induced breakdown of inhibition.   While our use of an acute model may limit applicability to chronic human epilepsy, it was necessary in order to create the simple structure needed to test our hypothesis. The use of an acute model also allowed us to determine that complex epileptic network interactions do not require pathological connectivity.

We hypothesized that the coupling mechanism is reflected in the morphology of LFP deflections associated with synchronized neuronal bursts during ictal events. Close to the 4-AP ictal focus, LFP deflections are negative (downward) and temporal delays are short. At distances greater than ~4 mm, the LFP deflections are positive (upgoing) with timing consistent with synaptic delays (~10 ms). These observations are not consistent with a passive volume-

conducted process, as we would then expect preserved polarity and zero or minimal temporal delays. Instead, our findings suggest that monosynaptic local recurrent excitatory projections arising from pyramidal neurons within the ictal zone dominates in nearby regions; whereas, territories at a distance to the ictal zone are dominated by di-synaptic feedforward inhibition, involving projections to inhibitory interneurons(Marshall, Li et al. 2016).

PV(+) interneurons are physiologically well-positioned to exert the inhibitory veto(Cammarota, Losi et al. 2013, Pouille, Watkinson et al. 2013, Sessolo, Marcon et al. 2015). Their small size, high input resistance, and low rheobase make them sensitive to synchronized excitation input(Markram, Toledo-Rodriguez et al. 2004, Kepecs and Fishell 2014). Their perisomatic projection makes them good candidates for exerting a sufficiently strong inhibitory effect to prevent ictal invasion(Pfeffer, Xue et al. 2013). Two-photon calcium imaging confirmed that PV(+) interneurons responded rapidly to distal ictal events (somatosensory to visual cortices). The strong inhibitory post-synaptic response is a likely source of the polarity flip seen in our spike-triggered averaging study.

Most studies of epileptic networks during seizures rely on low-frequency EEG analysis that reflects mainly synaptic activity(Kramer, Kolaczyk et al. 2008, Kramer, Eden et al. 2010). It is clear from our demonstration of a dual-focus network that it may be difficult to deduce the existence of multiple disparate foci from an analysis limited to synaptic activity. Analysis of temporal delays during ictal events can be a rich source of information, but the observed 'ping-ponging' between the foci indicates complex, bilaterally directed coupling dynamics could complicate the picture. It is important, therefore, to examine not only field potentials but also multiunit activity either directly or using a proxy signal (e.g. high gamma activity).

In conclusion, our study shows that focal ictal events project strong excitation over ipsilateral hemisphere in an acute rodent seizure model. Compromised local inhibitory response, regardless of its distance from the ictal core, can result in seizure propagation and epileptic network formation. Further studies are required to discriminate various distance-dependent seizure defense mechanisms.

Chapter 4

Spatial dissociation between interictal epileptiform discharges and neocortical epileptic foci suggests exhaustible inhibition at ictal penumbra

Abstract

Interictal epileptiform discharges (IEDs), an epilepsy hallmark, have been classically considered to co-localize with ictal onset zones (IOZs). However, distributed IED-generating mechanisms that involve areas outside the IOZ have also been proposed, since in some patients IEDs have been reported to occur outside their IOZs and IED occurrence could temporally dissociate with seizure frequencies. How focal epilepsy induces a distributed network favoring IED generation and whether chronic structural changes of cortical circuitry are required are still subject to ongoing debates. Using wide-field calcium imaging and multielectrode array recordings, we showed that normal cortical circuitry was capable of rapidly creating and sustaining a distributed IED-generating network in response to the creation of a single neocortical epileptic focus. We showed thalamus was an indispensable participant of the distributed IED-generating network. Our study confirmed a distributed network mechanism for IED generations. Weakening of surround inhibition, either by compromising cortical inhibitory defense or enhanced thalamocortical oscillations, may explain the spatiotemporal dissociation between IEDs and focal seizures.

95

4.1 Introduction

4.1.1 Localization of interictal epileptiform discharges in focal epilepsies

Interictal epileptiform discharges (IEDs), an EEG hallmark of epileptic brain, have been used to guide epilepsy diagnosis, prognosis, and therapy (Wirrell 2010). The interplay between IEDs and ictal events has long been investigated and may depend on subtypes of seizures (Avoli, Biagini et al. 2006). For patients with focal epilepsies, spatial association between IEDs and ictal onset zone (IOZ) provides clinically critical information, since several therapeutic strategies, such as seizure abortive device (Heck, King-Stephens et al. 2014) and epilepsy surgery, rely on precise localization. Although previous studies have shown IEDs may co-localize with IOZs (Alarcon, Garcia Seoane et al. 1997, Bautista, Cobbs et al. 1999), IEDs have also been reported to arise from spatially dissociated neuronal populations (de Curtis and Avanzini 2001). This dissociation hypothesis has been further strengthened by recent multielectrode array recordings in human epilepsy patients, which shows diverse cellular reactions during IEDs dissimilar to seizures (Keller, Truccolo et al. 2010), as well as large scale whole brain ECoG recordings in animal study (Vanleer, Blanco et al. 2016). IED frequency has also been shown to dissociate with seizure severity and frequency as well as their responses to anti-seizure medications, further suggesting IEDs may be generated by different mechanisms from ictal events itself (Gotman and Marciani 1985, Selvitelli, Walker et al. 2010, Steinhoff, Scholly et al. 2013, Karoly, Freestone et al. 2016).

In vivo seizure models have shown widespread effects from focal ictal activity – such as hemisphere-scale glial activation and neurovascular responses (Bahar, Suh et al. 2006, Geneslaw, Zhao et al. 2011, Zhao, Nguyen et al. 2011, Ma, Zhao et al. 2013). It is therefore conceivable

that focal ictal activity may irritate regions where it projects to, therefore, create spatial dissociations. This may also explain why IED frequency increases after human spontaneous seizures (Goncharova, Alkawadri et al. 2016) and IED itself may reflect the degree of brain damages (Gotman and Marciani 1985). However, the causal relationship may be more complicated in chronic seizures, as neuronal synchronization during IEDs may contribute to epileptogenesis (Staley, White et al. 2011) through Hebbian plasticity (Mehta, Dasgupta et al. 1993, Hsu, Chen et al. 2008), which has also been supported in previous animal studies (Chauviere, Doublet et al. 2012, Huneau, Benquet et al. 2013)).

Here, we used bilateral multielectrode array recording and wide-field calcium imaging to investigate the spatial correlation between ictal events and IEDs, testing the classical assumption that IEDs colocalize with IOZs (Alarcon, Garcia Seoane et al. 1997). We used acute 4-aminophyridine (4-AP) injection as a focal seizure model to test the co-localization assumption in various cortical areas. Our experiment confirmed IEDs do spatially correlate, but not co-localize, with the seizure-onset zone. Specifically, IEDs developed at areas which ictal activities project to – the ipsilateral surround as well as the mirror site of the contralateral hemisphere. We showed cortical IEDs are dependent on thalamic inputs, as the area where IEDs are generated showed increased excitability of thalamic inputs. The results suggested IEDs may be consequential to pathologically altered circuitry property caused by repetitive exposure to ictal projections. Comprehensive understanding of spatiotemporal association between IEDs and focal seizures are therefore required to achieve high precision therapy.

4.2 Materials and Methods

All the experimental procedures, including animal preparation, calcium imaging, and multielectrode array recordings were the same as Chapter 3, Section 2. Multiunit spike detection threshold was increased to -4.5 s.d. for more specific multiunit spike detection results. Ictal events were reviewed visually.

4.2.1 Interictal epileptiform discharge identification

Paroxysmal LFP discharges (less than 2 seconds, at least 500 μV in amplitude) that occurred during interictal intervals were considered IEDs. IEDs were required to be at least 2 seconds apart to be considered as separate events. In the case of multielectrode array study, detectable multiunit burst during epileptiform events (at least 2 electrodes with instantaneous firing rate > 50 spikes/sec) were also required for IED definition. IEDs were further categorized according to which hemisphere the associated multiunit bursts were detected (ipsilateral, contralateral, or both if both hemispheres were associated). IEDs were further separated into pre-spike (-200 to -35ms relative to the climax of neuronal bursts), the IED proper (-35 to +35 ms), and post-spike periods (+35 to +500 ms) following Keller and college's work (Keller, Truccolo et al. 2010). LFP power of each channel during IED proper period was calculated and heat maps were generated to present the spatial involvement of IEDs.

4.2.2 Thalamic recording during epileptiform events (Contributed by Eliza Baird-Daniel)

Four glass electrodes were employed to record the LFPs from the 4-AP injection site, the homotopic contralateral cortical area (mirror focus), and both ipsilateral and contralateral thalami.

The thalamic electrodes were placed in the ventrobasal region: 2.6 mm posterior to Bregma, 2.8 mm lateral to the midline, and 5.8-6.0 mm ventral to the surface of the cortex on either side to target both the ventro posterolateral (VPL) and ventral posterolateral thalamic nuclei (VPM). The onset time of each IED during an epileptiform event was defined as the moment when the LFP signal reached 3 times the standard deviation of the baseline noise level.

4.2.3 Selective thalamic inactivation

In a subgroup of experiments, tetrodotoxin (TTX) (0.3 mM, 1μL) was injected into either the contralateral or ipsilateral thalamus ~30 minutes after development of 4-AP ictal events. These injections targeted the ventrobasal (VB) nuclei of the thalamus. Given the volume of fluid injected, and the known diffusion of TTX in the thalamus we projected that a 1-1.5mm^3 volume of the thalamus was electrically silenced (Sacchetti, Lorenzini et al. 1999). During these experiments, to ensure the TTX was not impacting cortical activity and that the cortex was still capable of sustaining epileptiform events, bipolar cortical stimulation was employed to elicit a seizure. The bipolar electrode (1 mm apart) was placed across the 4-AP injection electrode and square-wave electrical stimulation (1mA in amplitude and 1ms in duration) was applied using a stimulation isolator and Master-9 (A.M.P.I. Jerusalem, Israel). The location of the TTX injection in the thalamus was confirmed in a pilot study with injection of 1μL blue dye RH-1692 (Optical Imaging Ltd. Rehovot, Israel).

4.3 Results

4.3.1 Ictal calcium activity was focal while IED's was globally propagating (Contributed by Eliza Baird-Daniel)

After approximately 10 minutes, focal cortical injection of 4-AP elicited stereotypical, repetitive ictal events (Figure 4.1). Ictal events lasted on average 39.18 ± 19.59 s (mean $\pm$ sd, n =116 ictal events) with average interictal intervals of 118.22 ± 97.40 seconds (n=32 ictal events from 6 animals). Wide field calcium imaging demonstrated that calcium increases associated with ictal events were focal and spatially constrained to a localized area around the 4-AP injection site with an average area of 9.44 ± 2.69 mm^2 (n=7 rats) (Figure 4.1B).

During interictal periods, brief, intermittent epileptiform discharges were noted. These discharges, here termed as interictal epileptiform discharges (IEDs), were brief (0.98 ± 0.42s, n=50, 6 animals) with an average frequency of 1.8 ± 0.85 events per minute (Figure 4.1A). Interestingly, in contrast to ictal events, wide-field calcium imaging demonstrated that neuronal calcium increases during IEDs occurred globally, involving both hemispheres (Figure 4.1C). Correlation maps showed that the average area of involvement was 46.99 ± 7.46 mm² (n=7 animals), which was significantly greater than that of ictal events ($p<0.001$, unpaired t-test).

Figure 4.1: Neuronal calcium signals were focal during ictal events but global during IEDs
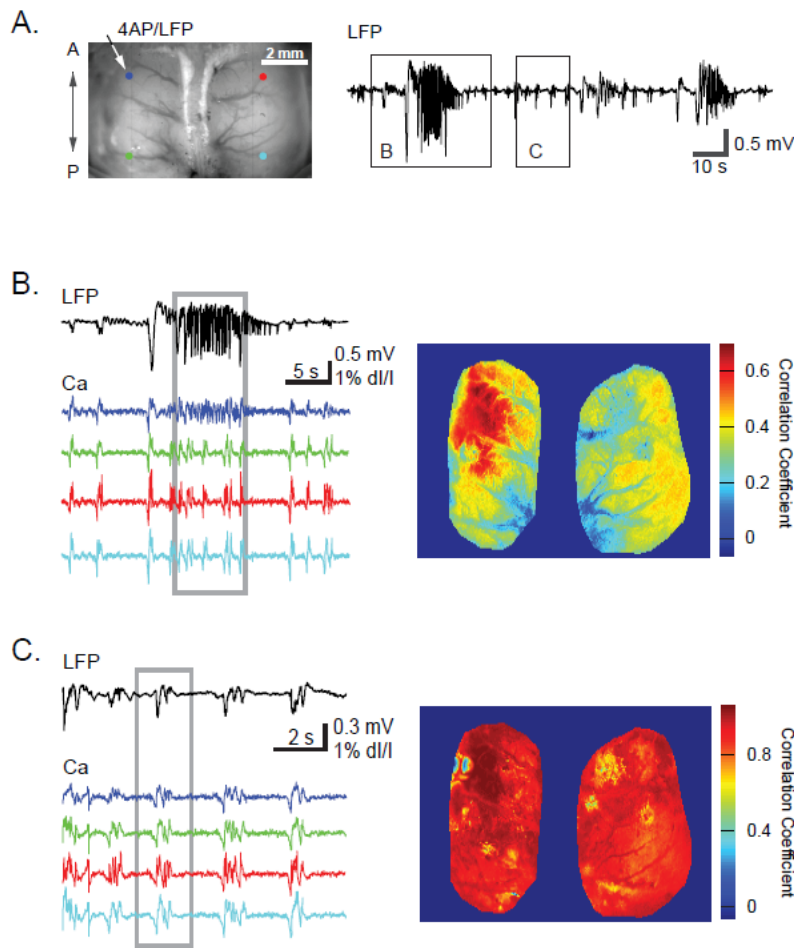
A) (Left) Imaged bilateral cortices with 4-AP injection site and LFP recording indicated with
an arrow. Four colored ROIs indicate locations of calcium traces shown in B and C.
(Right) LFP trace shows ictal and interictal events. Boxed regions of ictal event
expanded in B and interictal events expanded in C.

B) (Left) LFP (black) and calcium traces from four ROIs shown in A, indicate focality of
ictal event with highest correlation in ROI adjacent to 4-AP injection site. Note that the
high frequency activity present at the 4-AP injection site (blue trace) does not occur in

other ROIs. (Right) Correlation coefficient heat map shows the spatial location of pixels

with highest correlation with a seed at the 4-AP injection site.

C) (Left) LFP (black) and calcium traces from four ROIs shown in A, during IEDs indicate

global activation.(Right) Correlation coefficient heat map shows the spatial involvement

during the boxed IED at left. A seed trace was selected at the 4-AP injection site. Note

the global propagation of the IED.

4.3.2 IED calcium signal initiation avoided the ictal onset zone (Contributed by Eliza Baird-Daniel)

Although IEDs were associated with global calcium surges, the global involvement did

not occur simultaneously everywhere. Instead, local surge timing varied according to its location

relative to the ictal onset zone. Two examples of differential calcium surges are provided in

Figure 4.2A. The earliest calcium surge were observed at the ipsilateral surround and

contralateral homotypic cortex, respectively. We therefore further divided the cortex into

quadrants: Zone 1- ipsilateral ictal onset zone/4AP injection site, Zone 2- ipsilateral surround,

Zone 3 - contralateral homotopic and Zone 4- contralateral surround (Figure 4.2B). Surprisingly,

early surges were found mainly in Zone 2 and Zone 3, avoiding Zone 1(the IOZ) (Figure 4.2B,

C). Of the 36 IEDs analyzed in 5 animals, only one arose first in the quadrant containing the 4-

AP injection site (Figure 4.2C), which was a statistically significant non-random distribution

(chi-squared test, $p < 0.001$).

Figure 4.2: Temporal variation of calcium surges during IEDs
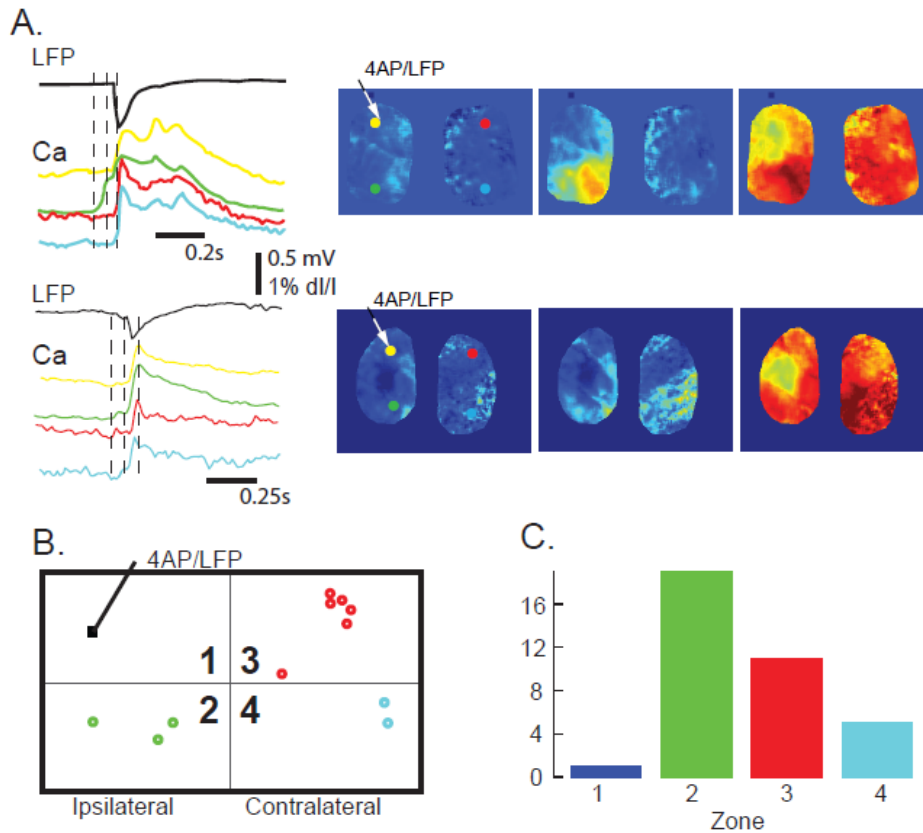
A) Top row shows example of ipsilaterally-initiating IED in a single animal. At Left, the black top trace represents the LFP at the 4AP injection site. Lower traces represent wide-field calcium imaging data 4 ROIs depicted in the first panel at right. Panels at right correspond to calcium imaging of exposed bilateral cortex at three time-steps (each 20ms apart) denoted as dashed vertical lines at left. Bottom row shows the same for contralaterally-initiating IED in a separate animal. Note that while events propagate globally, the initiation of IEDs does not occur in the 4AP injection site.

B) Schematic showing 4 cortical zones. Zone 1 is defined as containing the 4-AP injection/seizure initiation site, Zone 2 is ipsilateral surround, Zone 3, contralateral

homotopic and Zone 4, contralateral surround. ROIs show multifocal initiation sites from one example animal.

C) Bar graph showing spatial distribution of initiation sites of all IEDs detected via calcium imaging across 5 animals (36 events). Note that the majority of events were detected outside zone 1.

4.3.3 Spatial distribution of IED-associated multiunit bursts

Since calcium imaging is limited in temporal resolution and unable to record specific timing of neuronal action potentials, we endeavored to further study the IED's temporal differential calcium surge with bilateral multielectrode recordings. As expected from calcium imaging study, we found ictal events were restricted to the area surrounding the 4-AP injection site; whereas, IEDs were associated with widespread LFP fluctuations (Figure 4.3A, B). However, spatial distribution of LFP power during IEDs was uneven. Increase of LFP power was more prominent at ipsilateral surround (Zone 2 in calcium imaging study) and contralateral homotopic cortex (Zone 3) This dissociation between IEDs and IOZs were corresponded with calcium imaging findings.

Figure 4.3: Multiunit activity and LFP power during ipsilateral IEDs
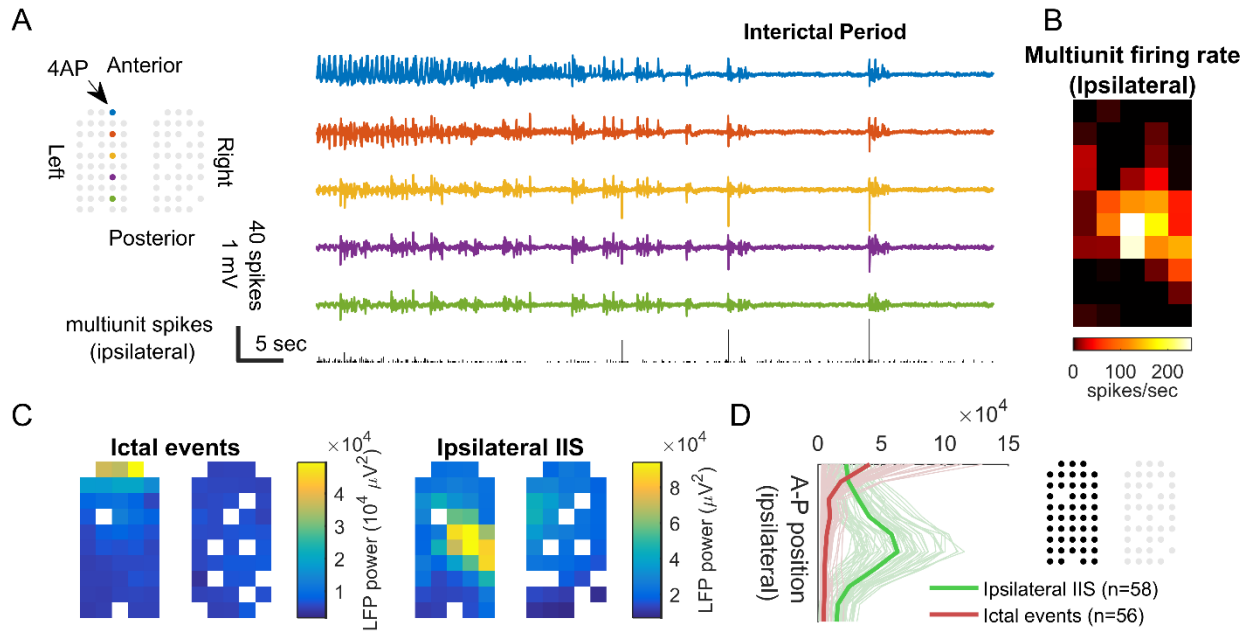
A) Cartoon illustrates locations of electrodes in ipsilateral hemisphere. Colored ROIs indicate the physical locations of the electrodes from which the LFP tracings (right) are recorded. LFP traces depict the termination of an ictal event followed by an interictal period. The bottom histogram shows ipsilateral hemisphere's multiunit spike counts every 100 ms. IEDs are associated with burst of neuronal activity whereas ictal activity does not elicit significant bursts.

B) The averaged multiunit firing rate across the ipsilateral cortex during all ipsilateral-initiating IEDs. Note the highest burst rate is found outside the 4-AP injection zone.

C) The spatial distribution of LFP power during the ictal events (n=56) and ipsilateral IEDs (n=58). While ictal events demonstrate field activity that remains restricted to the 4-AP injection site, IEDs instead occur in the ipsilateral surround, away from the focus.

105

D) LFP power of ictal events and ipsilateral IEDs were marginalized along the anterior-posterior axis of one (left) hemisphere. The thin, light-colored lines correspond to each episode of ictal (red) or IED (green) event, and the thick, dark-colored lines are the averages. The centers of ipsilateral IEDs were significantly more posterior than the ictal onset zone (median IED activity center: 2 mm from the anterior edge, U test, $p \ll 0.001$).

IEDs with ipsilateral multiunit bursts showed increased LFP power was most prominent in the cortex surrounding the 4-AP injection site (Figure 4.3B right and 4.3C). The exaggerated LFP responses were accompanied with focal multiunit bursts (Figure 4.3A & 4.4; n = 58 IEDs, 2 animals). The epileptiform discharges and multiunit bursts appeared to propagate towards the ictal onset zone, emerging sequentially in space, constituting a traveling wave propagating from the surround toward the 4-AP ictal center (Figure 4.4B). This wave-like phenomenon was found to travel at an average velocity of 26.2 cm/second (Figure 4.4C, F-test, $p < 0.001$). Directions of individual traveling waves were highly similar (Figure 4.4D, n = 27, circular s.t.d. = 31 degrees, Rayleigh test, $p < 0.001$).

Figure 4.4: IEDs formed traveling waves initiating at ipsilateral surround and propagating centripetally towards the IOZ
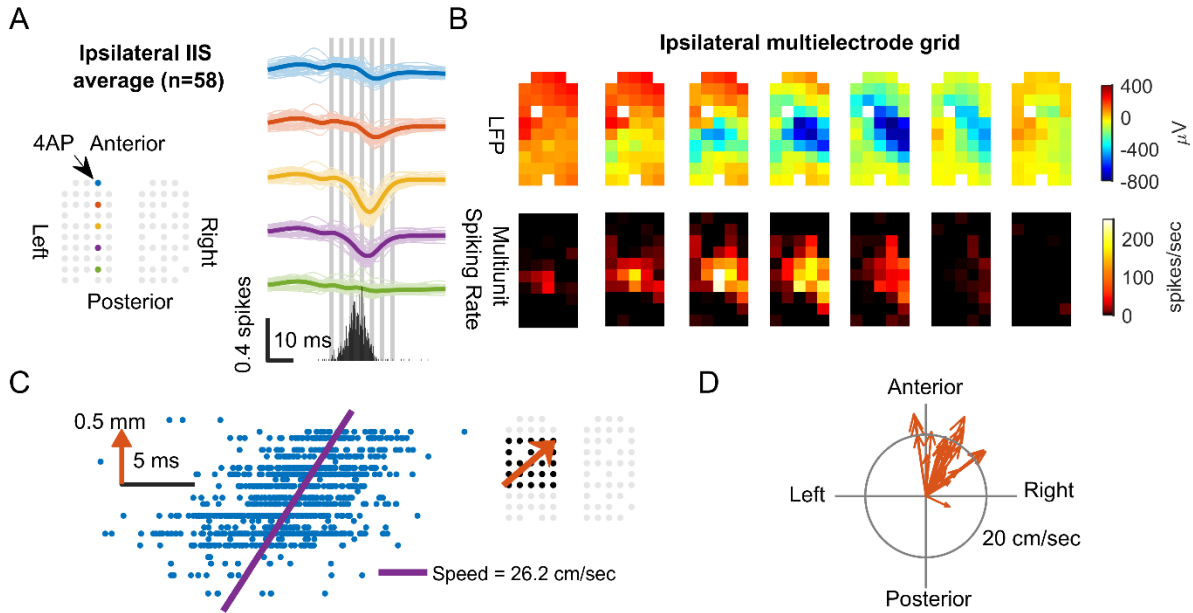
A) (Left) Cartoon illustrates electrode locations and colored electrodes indicate sources for traces on right. Average of multiple (n=58) ipsilateral IEDs arising from ictal surround. The thick lines represent the average. The bottom histogram shows average left hemisphere MUA spike count every 1 ms.

B) The averaged spatiotemporal evolution of LFPs and multiunit spiking. The timing of each frame is indicated by the gray vertical bars in Panel A. Notice the sequential appearance of multiunit spikes and LFP discharges (left lower to upper right).

C) Local regression (data from the black-marked electrodes, right inlet) shows that multiunit spikes (blue dots) were detected sequentially along the centripetal direction (orange arrow, right inlet, F-test p << 0.001). All ipsilateral IEDs were temporally aligned according to its neuronal burst climax for the regression analysis. Vertical axis of the

107

raster plot (left inlet) indicates each electrode's position along the propagation path

(orange arrow).

D) Ipsilateral IEDs propagate toward the ictal zone. Each arrow represents each left

hemisphere IED traveling wave's velocity (n=27, mean direction = 62 degree, Rayleigh

test, p << 0.001).

For contralateral IEDs (IEDs with ipsilateral multiunit bursts), highest LFP power increase were observedin the contralateral homotopic cortex (Figure 4.5). Analogously, the focal exaggerated LFP responses were associated with multiunit bursts (Figure 4.5). Unlike ipsilateral IEDs, we did not find traveling wave behavior in contralateral IEDs.

Figure 4.5: Multiunit activity and LFP power of contralateral IEDs
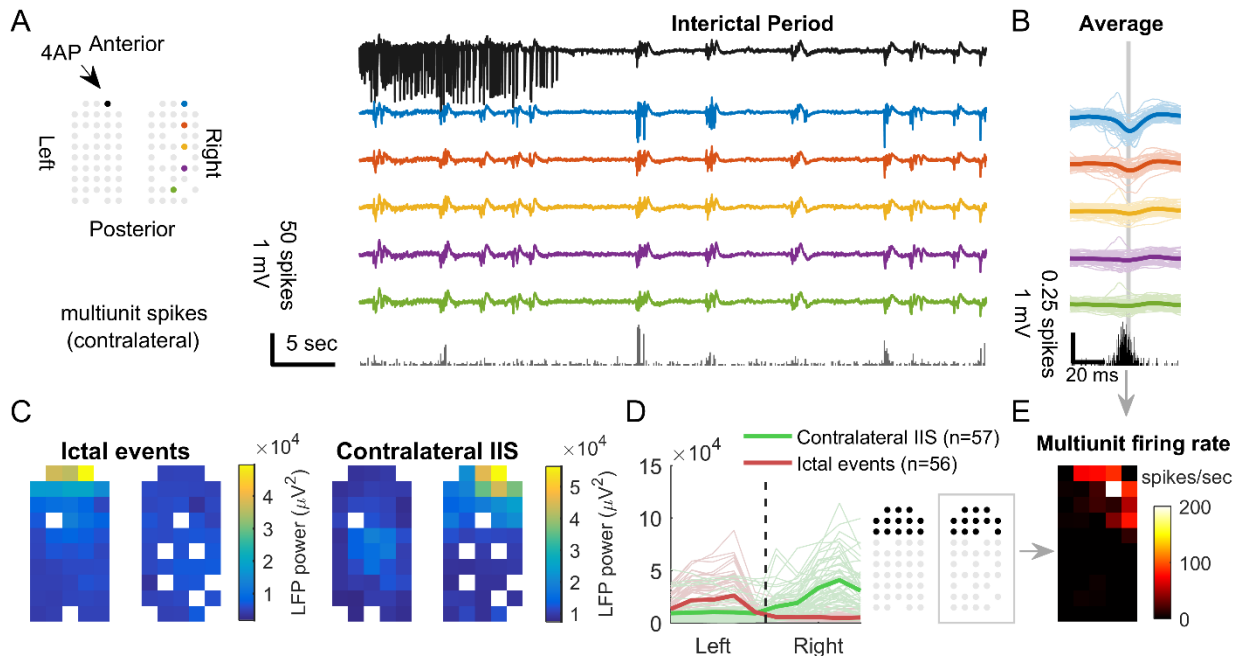
A) Cartoon illustrates locations of electrodes in contralateral hemisphere. Colored ROIs

indicate the physical locations of the electrodes from which the LFP tracings (right) are

recorded. LFP traces depict the termination of an ictal event followed by an interictal

period. The bottom histogram shows contralateral hemisphere's multiunit spike counts

every 100 ms. IEDs are associated with burst of neuronal activity whereas ictal activity

does not elicit significant bursts.

B) Average of all contralateral IEDs (n=57). Notice the largest amplitude of LFP discharge

are located at the anterior electrodes (blue traces) and the large increase in multiunit

firing rate associated with the IED peak.

C) The spatial distribution of LFP power shows focal activation of the ictal onset zone in the

hemisphere ipsilateral to the 4-AP injection in the region of the injection. IED activity,

on the other hand, has maximal field activity from the contralateral homotopic region.

White boxes show electrodes that were not recording.

D) LFP power from electrodes in black in anterior portion of the grids during ictal (red) and

IED (green) events. The average is in bold. Contralateral IEDs were not associated with

electrical activity at the ictal focus (U test for cross-hemisphere LFP power ratios, $p \ll$

0.001).

E) The averaged multiunit firing rate (time is indicated by the gray vertical bar in Panel B).

Note that the neuronal bursts were detected at the contralateral homotopic mirror focus.

4.3.4 IEDs triggered by thalamus activity (Partially contributed by Eliza Baird-Daniel)

It is hard to explain the multifocal, bilateral onset and rapid generalized spread of IEDs with a known cortical mechanism. Instead, one possible explanation is a thalamic site of origin. To test this hypothesis, we simultaneously recorded IEDs from bilateral thalami, targeting both the VB nuclei, as well as bilateral neocortices in the area of the 4-AP injection and contralateral homotopic cortex (Figure 4.6A). All IEDs appeared to initiate in the thalamus before quickly spreading to the cortex with a delay of 10.33±3.13 ms (n=295 IEDs in 6 animals) (Figure 4.6B-D). The ictal evolution, on the other hand, was a predominantly cortical event with minimal involvement in the thalamus after the initial spike (Figure 4.6A).

Figure 4.6 Simultaneous bilateral cortical and thalamic LFP recordings suggested thalamic origin of IEDs (Contributed by Eliza Baird-Daniel)
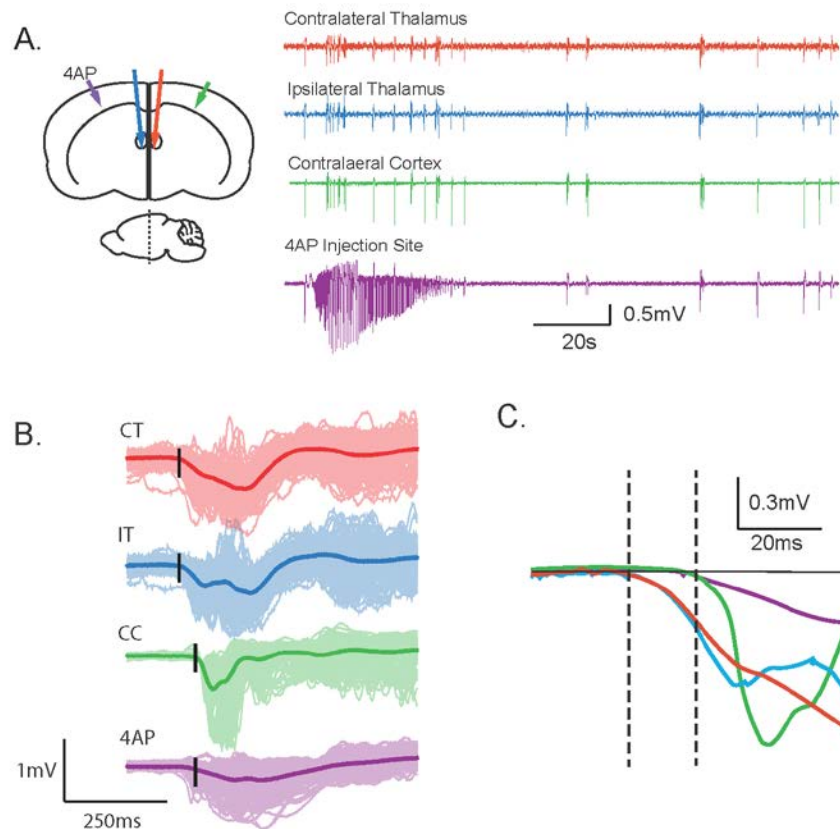
A) (Left) Cartoon illustrates experimental set-up with bilateral thalamic and cortical LFP electrodes. At right, example LFP traces from one animal showing activity during and after an ictal event. Colors correspond to arrows in the cartoon. Note that IED events involve both the thalamus and the cortex while low voltage-fast ictal activity is constrained to the 4AP injection site.

B) Bold traces represent LFP data from the same locations averaged across 295 IED events shown in lighter shade. Black vertical lines denote event initiation. Note the delay

between IED initiation in the thalamus and IED initiation in the cortex, especially in the

seizure focus.

C) Averaged traces from B overplayed. Horizontal black line denotes baseline. Leftmost

dashed line shows thalamic IED onset time while the dashed line at right shows the

cortical IED onset. Thalamic onset precedes cortical onset by on average 10.33 ± 3.13 ms

(n=6 animals)

To confirm a causal role of the thalamus in initiating IEDs, we injected TTX, a potent

sodium channel blocker, into the VB nucleus of the thalamus to abolish its electrical activity.

Silencing the thalamus effectively abolished all ictal activity and significantly decreased IED

frequency from 1.8 ± 0.85 spikes/min prior to TTX injection to 0.44 ± 0.35 spikes/min (n=6

animals) after TTX injection (paired t-test, $p< 0.001$) (Fig 4.7A-B). To ensure that cortical

excitability was not impaired by thalamic TTX injection, we directly stimulated the 4-AP

injection site of the cortex under these conditions and were able to trigger an ictal event (Figure

4.7C).

Figure 4.7: Thalamic inactivation abolishes both ictal and IED events
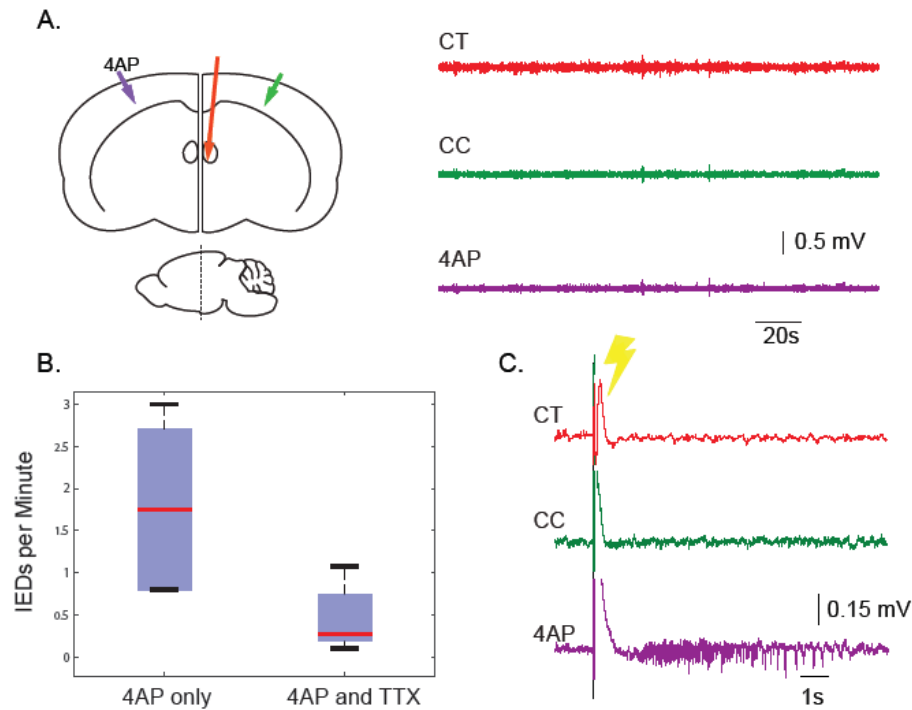
A) (Left) A cartoon shows experimental set up for TTX injection in contralateral cortex. At right, LFP traces correspond to colored arrows in one animal after TTX injection in the contralateral thalamus. Note the lack of activity on all channels.

B) A box and whisker plot showing IED spike rate in spikes/min before and after TTX injection. 4-AP only condition elicited a mean of 1.8±0.85 spikes/min while after TTX injection, this was reduced to 0.44±0.35 spikes/min (n=6 animals).

C) Stimulation of the cortex at the 4-AP injection site. A 2 ms, 10 mA single stimulus delivered at the 4-AP/seizure initiation site successfully induces an ictal event in spite of thalamic inactivation with TTX.

4.3.5 Anesthesia-induced polyspike complexes (PSCs) evolved into IEDs after establishment of epileptic focus

Prior to injection of 4-AP, episodic, generalized LFP fluctuations could also be observed from both hemispheres by multielectrode array recording (Figure 4.8). Its frequency is inversely correlated with depth of anesthesia (isoflurane 1.5% versus 3%, inter-PSC interval: 4.7 versus 17 seconds, unpaired t-test $p < 0.001$). These anesthesia-induced polymorphic LFP fluctuations, here termed polyspike complexes (PSCs), differed from IEDs in several specific ways. First, prior to 4-AP injection, PSCs were not associated with multiunit bursts (Figure 4.8A), nor did they elicit the 'focal' sharp LFP spikes, a hallmark of the IEDs described previously (Figure 4.8B). PSCs recorded before the injection of 4-AP were never associated with spatially-specific onset of high amplitude sharp LFP fluctuations either in ipsilateral surround (0/42 versus 58/599; $n = 2$ animals, χ^2 test $p \ll 0.001$) or contralateral cortex (0/42 versus 57/599, 2 animals, χ^2 test $p < 0.001$) (Figure 4.8B-C), which only developed after 4-AP injections.

Figure 4.8: Anesthesia-induced thalamocortical PSC oscillations differ from IEDs
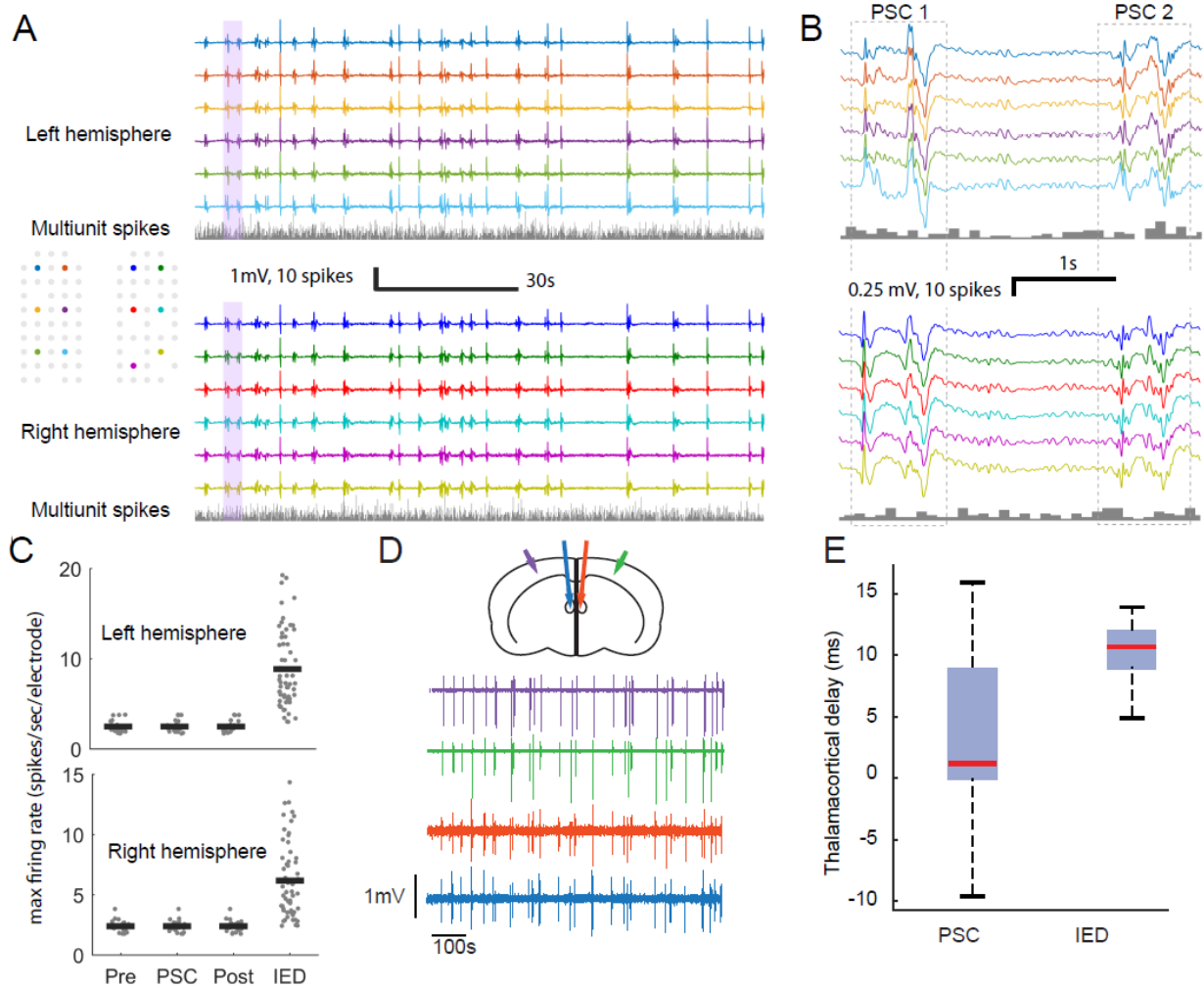
A) Baseline recording before 4-AP injection in one animal. PSCs occur intermittently with global involvement. Unlike IEDs, baseline PSCs are no associated multiunit bursting. Pink shaded vertical bar is expanded and displayed in Panel B.

B) Two polyspike complexes. Note the polymorphic nature of polyspike complexes as opposed to IEDs. Also, unlike IEDs, the morphology of PSCs are not invariant, as the comparison between PSC1 and PSC2.

C) Maximal multiunit firing rate, averaged over each hemisphere, before (pre, -3 to -1 second with respect to the time of peak LFP power), during (-1 to +1 second), and after (post, +1 to +3 second) polyspike complexes. 21 baseline PSCs were observed. There is no significant increase of multiunit firing rate during PSCs compare to pre and post-PSC periods (paired t-test, $p > 0.05$). However, the maximal firing rates during IEDs are significantly higher than baseline PSCs. (Left: 2.46 versus 8.83 spikes/sec/electrode, t-test $p<0.001$, Right: 2.38 versus 6.16 spikes/sec/electrode, t-test $p<0.001$, firing rate estimated by 10ms Gaussian kernel.)

D) Below, LFP traces correspond to electrodes represented as colored arrows in the cartoon above. Traces are taken before 4-AP injection. Note that the PSCs occur bilaterally in both the thalamus and the cortex.

E) A comparison of the delay between thalamic and cortical initiation of PSCs and IEDs before and after 4-AP injection in the cortex, respectively. Note the much greater variability of initiation delay in the pre 4-AP condition.

4.4 Discussion

In this study, we show that the establishment of an acute neocortical seizure focus leads to the rapid formation of a widely distributed bilateral, multifocal IED-generating network orchestrated by the thalamus. Spatial dissociation between IED and IOZs have important diagnostic and therapeutic implications. First, the rapid formation of IED-generating network indicates that chronic structural change is not required; instead, normal circuitry is capable of creating and sustaining multifocal IEDs after a focal neocortical ictal perturbation. Second, IEDs may not co-localize with IOZs, indicating using IEDs to localize epileptic focus may be prone to erroneous identifications. Finally, spatial distribution of IEDs indicates local inhibition defect could happen at brain regions where IOZs projected to, as cortical responses to anesthesia-induced thalamocortical oscillation were enhanced at ipsilateral surround and homotopic cortex.

4.4.1 Spatial Relationship between IOZ and IEDs

While IEDs in focal epilepsy often co-localize with the IOZs (Hamer, Najm et al. 1999, Luo, An et al. 2014, Khoo, Hao et al. 2017), it has also been known for years from human subdural electrode studies that the "irritative zone", from which IEDs arise, is more extensive than IOZs (Luders, Najm et al. 2006). Surgical removal of the irritative zone is not absolutely required to abolish epileptic seizures (Wyllie et al., 1987). Recent neuroimaging studies have also confirmed that focal epilepsies can associate with a distributed, abnormal functional network rather than a single epileptogenic region (Fahoum, Lopes et al. 2012, Kramer and Cash 2012, Laufs 2012, Constable, Scheinost et al. 2013). Additional lines of evidence, including MEG recordings, depth electrodes and multiple dipole modeling, have indicated that spatially

separated IEDs of different amplitudes and duration may arise out of the IOZ (Sutherling, Crandall et al. 1988, Sutherling and Barth 1989, Ebersole and Wade 1991, Alarcon, Guy et al. 1994, Baumgartner, Lindinger et al. 1995, Bautista, Cobbs et al. 1999). Overall, these data indicate that circuit mechanisms underlying ictal and interical events may be quite distinct (Jensen and Yaari 1988).

However, the pathophysiology of this widely distributed irritative zone has been presumed to depend on progressive development of independent cortically-based regions of potential epileptogenicity that require chronic structural, chemical or synaptic reorganization (Goldberg and Coulter 2013). Proposed mechanisms such as axonal sprouting, glial scarring, neurotransmitter receptor and gene up- and down-regulation that result in synaptic strengthening or increased excitability and synchronization require prolonged exposure to recurrent ictal events. In this report, we show that such a widely distributed epileptic network capable of sustaining multifocal IEDs can be formed rapidly from normal cortical circuitry as a response to a focal neocortical IOZ. Mechanistic explanations formed here do not necessarily rely on chronic alterations in cortical circuitry but instead rely on existing mechanisms that are activated within the normal brain.

4.4.2 Localization and variability of IEDs

Initial theories regarding the cortical basis of IEDs arose from the application of disinhibiting agents such as penicillin or bicuculline to mammalian cortex (Matsumoto and Marsan 1964, Prince 1968, Prince 1971). The resulting population spikes were cortically-based stereotypical, electrographically-stable events involving the synchronous firing of large

118

populations of cells (Matsumoto and Marsan 1964, Prince 1968, Prince 1971, Traub and Wong 1982). However, in human epilepsy, single unit recording from the IOZ demonstrate a lack of synchronized single unit bursting during IEDs (Wyler 1982, Colder, Frysinger et al. 1996, Colder, Wilson et al. 1996). These results point to the possibility that IEDs arise from an unsampled location outside the IOZ. More recent studies with 2-photon single cell calcium imaging from various subregions of the hippocampus have revealed that even within the IOZ, the population of cells participating in each IED is variable and shifting (Feldt Muldoon, Soltesz et al. 2013, Muldoon, Villette et al. 2015). Recent studies of single cell activity during interictal events in the human cortex also suggest a wide heterogeneity in neuronal firing with different populations of neurons participating in sequential bursts (Keller, Truccolo et al. 2010).

Our work extends these studies since we were able to record from large areas of the neocortex, a considerable distance from the IOZ. We show that while IEDs can be recorded from the IOZ with field electrodes, these large-scale recordings are very misleading. The cortical origin of the IEDs not only was extremely variable but was more likely to arise outside rather than within the IOZ, with some even arise from the contralateral hemisphere. However, the cortical location from IEDs was not randomly distributed throughout the cortex but rather spatially clustered. The concept that IEDs can cluster into "dominant" imitation sites has been described using voltage sensitive dyes. In fact, as in our studies, non-random spatial clustering occurred rapidly and likely relied on intrinsic cortical circuitry rather than chronic mechanisms (Vitantonio, Xu et al. 2015). Non-random formation of epileptic networks has also been described in human neocortical epilepsy using chronic subdural grid recordings. Such networks have been hypothesized to create a cortico-cortico inhibitory network to limit seizure spread(Tracy, Osipowicz et al. 2014). As we will discuss, a possible unifying theory involves

119

implicating the thalamus, not only in orchestrating the rapid development of an epileptic network but in triggering IEDs.

4.4.3 Role of the thalamus in focal epilepsy IEDs

Thalamocortical loops play a critical role in epileptogenesis (Gasteiger, Albowitz et al. 1985, Mondragon and Lamarche 1990, Detre, Alsop et al. 1996, Redecker, Bruehl et al. 1997, Blumenfeld 2002, Englot, Modi et al. 2009, Valentin, Garcia Navarrete et al. 2013, Krishna, King et al. 2016), as been studied in absence epilepsy (Gutnick and Prince 1972, Prevett, Duncan et al. 1995). However, its role in focal epilepsies has been less clear. Electrical recordings from the thalamus in focal neocortical seizure models in cats and monkeys have demonstrated thalamic recruitment (Gutnick and Prince 1972, Kusske 1976, Albowitz and Gasteiger 1985). IEDs have also been recorded from the thalamus in human patients with partial epilepsy via implanted depth electrodes (Sweeney-Reed, Lee et al. 2016). In many of these studies, IEDs were elicited with focal disinhibition using penicillin or bicuculline, which initiates IEDs in the neocortex where the drug is injected. In contrast to these prior studies, 4-AP does not compromise inhibitory synaptic strength but rather recruits a widely-distributed network of IEDs that emerge as a reaction to the ictal onset zone. Moreover, we clearly show that the thalamus is not recruited by the IEDs but rather triggers them and our acute model demonstrates that focal seizures can elicit rapid responses in thalamocortical circuitry leading to multifocal IEDs.

4.4.4 Mechanisms that may lead to cortical disinhibition

The evolution from anesthesia-induced PSCs to IEDs suggested thalamocortical loops may have been altered by exposure to focal ictal activity, and the change was spatially inhomogeneous (Figure 4.9). The ipsilateral surround and homotopic cortices received the most ictal projections from the IOZs (Figure 4.9 II). Prolonged exposure to ictal synaptic barrages may compromise inhibition responses (Figure 4.9 III). From Chapter 3, we have shown an ictal focus could cause large-scale inhibitory responses, potentially mediated by local PV-interneurons at projected sites. Intense usage of GABAergic synapses could lead to chloride accumulation (Raimondo, Burman et al. 2015) or receptor desensitization (Jones and Westbrook 1996). Repetitive use of inhibitory strength may also increase ambient GABA concentration, which can activate pre-synaptic GABA-B receptors (Scanziani 2000, Chalifoux and Carter 2011). GABA-B activation reduces releasing probability of GABAergic axonal terminals; therefore, inhibitory synaptic strength at the projected sites may be compromised. When thalamic input arrived, inadequate local inhibition failed to constrain the incoming excitation, causing multiunit bursts and IEDs (Figure 4.9 IV).

Alternatively, disinhibition by enhancing thalamic inputs toward ipsilateral surround and homotopic cortices could have contributed. Reciprocal interactions between the reticular nucleus and the corticothalamic neurons can lead to hyperpolarization and rebound bursting of thalamic neurons (Fogerson and Huguenard 2016). The ictal focus may elicit such a phenomenon in the thalamus resulting in enhanced thalamocortical activation. Via a divergent corticothalamic projection (Rouiller and Welker 2000), periodic bursting activity of thalamic neurons which projected to ipsilateral surrounding and homotopic cortices may be enhanced. Strong thalamic input could break through cortical defense and manifest as IEDs.

How then can we explain the fact that in most human focal epilepsies, IEDs often occur in or near the IOZ? The most likely explanation is that the 4-AP model elicits repetitive seizures with only a short interictal period and thus little time for the IOZ to recover before the next seizure occurs. Must human epilepsies occur with a much slower periodicity, at most a few times per week ,; such a long interictal-seizure intervals allows the neurons in a chronic human focus to recover, allowing them to sustain IEDs.

Figure 4.9 Theory of spatial dissocation between IOZs and IEDs

I. Baseline thalamacortical connectivity

II. 4-AP ictal event increases cortical excitability in the surround and contralateral homotopic foci

III. Post-ictal focus is metabolically exhausted while surround and contralateral homotopic cortex remain excitable

IV. Surround and mirror foci more responsive to thalamic projections causing multifocal IIS that avoid focus

In summary, we have demonstrated that widespread multifocal IEDs can emerge rapidly after the establishment of an acute epileptic focus. Chronic structural, chemical or genetic alterations are therefore not required to create a distributed epileptic network. The thalamus plays a critical role, not only in the development of this acute epileptic network, but also in the triggering of IEDs.

123

Chapter 5

A theoretical model for focal seizure initiation, propagation, termination, and progression

Abstract

Neocortical focal seizures can present with a plethora of behavioral manifestations that vary according to the affected regions. However, several key features have been consistently observed. Here, with minimal assumptions, we proposed a neural network model that account for long-standing behavioral observations as well as the most up-to-date electrophysiological recordings. We showed slow expansion of seizure territory and tonic-clonic transitions can be explained by two slow, sequentially activated processes: usage-dependent exhaustion of inhibition and adaptation current upregulation. The slowing-down features commonly observed before seizure termination can originate from an inhibition recovery process which happens after the tonic-firing ictal wavefront has dissipated. The model indicates that seizure onset pattern can vary according to distribution of recurrent inhibitory projections. It also provides a mechanistic understanding of how spike-timing dependent plasticity may contribute to spontaneous seizure generation. Macroscopically, the model explains how preference of ictal traveling wave direction may emerge and persist from purely white noise. Spiral waves underpinning status epilepticus are also predicted. Overall, our model explains the complex spatiotemporal dynamics of focal seizures with minimal, generalizable neurophysiological principles. With rapid advancement of clinical and experimental tools, we believe this work could provide a roadmap for future understanding and therapies for epilepsy patients.

5.1 Introduction

5.1.1 Review of common features of focal seizures

Focal seizures have been reported on for more than 3000 years, with descriptions dating back to ancient Mesopotamia (Worthington 2007, Magiorkinis, Sidiropoulou et al. 2010). Although focal seizures can present with a plethora of behavioral manifestations that vary according to the affected cortical regions, several key features have been consistently observed. Classically, focal seizures begin in a spatially constrained location, then propagate slowly to contiguous regions, as in the well-known Jacksonian march (Worthington 2007, York and Steinberg 2011, Extercatte, de Haan et al. 2015). As adjacent regions are progressively recruited, pronounced synchronization (Lehnertz, Bialonski et al. 2009, Jiruska, de Curtis et al. 2013) can be observed behaviorally, especially in seizures involving primary motor cortex: stiffening of the corresponding body parts occurs first, referred to as the tonic phase, followed by periodic spasm and jerks, termed the clonic phase (Mattson, Cramer et al. 1985). As seizures approach termination, the frequency of clonic movements typically slows down (Extercatte, de Haan et al. 2015). Synchronized activity stops abruptly and simultaneously across the entire affected brain region when seizures terminate. Similar dynamics are also commonly seen in across cortical regions (Anziska and Cracco 1977, Blumenfeld, Rivera et al. 2004, Kramer, Truccolo et al. 2012).

5.1.2 Phenomenological approaches versus biophysical models

These fascinating spatiotemporal dynamics have been investigated computationally (Soltesz and Staley 2011). Modeling seizure dynamics can be categorized into two approaches:

biophysical and phenomenological (Wendling 2008). Phenomenological models, as exemplified

by the Epileptor model (Jirsa, Stacey et al. 2014), have successfully captured the temporal

evolution of local field potentials (LFPs) during seizures. However, the abstract nature of the

phenomenological approach limits the direct link to biophysical mechanisms. Biophysical

approaches, on the other hand, permit the exploration of pathophysiological underpinnings of

clinically observed seizure dynamics (Naze, Bernard et al. 2015). Examples of processes that

have been investigated include intracellular and extracellular potassium dynamics (Cressman,

Ullah et al. 2009, Ullah, Cressman et al. 2009, Frohlich, Sejnowski et al. 2010, Krishnan and

Bazhenov 2011), transmembrane chloride gradients (Buchin, Chizhov et al. 2016), and calcium-

activated processes (Kudela, Franaszczuk et al. 2003, Yang, Franaszczuk et al. 2005). However,

given that extreme pathological seizure activity can activate a multitude of physiological

processes simultaneously, biophysical models may be limited to fragmented or overly specific

understanding of seizure dynamics. Additionally, the parameter space for biophysical models is

huge, and it is computationally challenging to reproduce all the possible factors underlying a

given process (Dyhrfjeld-Johnsen, Santhakumar et al. 2007).

5.1.3 Review of multielectrode array findings

Recently, multielectrode array recordings have revealed an unprecedented high-

resolution picture of neuronal dynamics in epilepsy patients, providing a window that can be

used to model at a level between the biophysical and phenomenological ends of the spectrum.

Seizures appeared to start from a millimeter-scale cortical region, with a transient band of tonic

firing at the time of ictal invasion (Schevon, Weiss et al. 2012). This band defines the extent of

the 'ictal core,' a region of seizing brain that slowly expanded at measured speeds of ≤ 1 mm per second. This speed corresponded to the progression of a Jacksonian march through the motor homonculus. Within the ictal core, neuronal bursts arose sequentially in space, behaving like traveling waves (Smith, Liou et al. 2016, Liou, Smith et al. 2017). The source of these faster waves has been studied intensely (Ursino and La Cara 2006, Gonzalez-Ramirez, Ahmed et al. 2015). Evidence has been provided that they arise from the edge of the seizure territory, travelling backward into the ictal core with average speed of 20 to 50 cm per second (Smith, Liou et al. 2016). Pre-termination neuronal dynamics also mimic large-scale patient behavior, showing progressively prolonged inter-burst intervals and progressive desynchronization (Kramer, Truccolo et al. 2012, Smith, Liou et al. 2016). To our knowledge, a model linking electrical activity at the precision of neuronal populations, constrained by biophysical mechanisms, to long-standing clinical observations supplemented by recent multiscale electrophysiological recordings has not been available.

Here, we propose such a biophysically constrained neural network model that reproduces the spatiotemporal evolution of human focal seizures and provides new predictions about the neuronal mechanisms of seizures (Steyn-Ross, Steyn-Ross et al. 1999, Liley, Cadusch et al. 2002, Kramer, Kirsch et al. 2005). We adopt an approach with minimal assumptions, aiming to show that complex spatiotemporal dynamics can arise from simple and experimentally validated neurophysiological principles. The model demonstrates the neurophysiological signatures of slow propagation, tonic-clonic transition, and pre-termination slowing. Our theoretical study offers several clinically and experimentally testable predictions regarding seizure-onset patterns, plasticity-induced rewiring, seizure progression, and traveling wave direction stabilities.

127

5.2 Material and Methods.

Patient data collection and processing has been reported in Chapter 2, Section 2.

5.2.1 Rate model

A spatially homogeneous neural field with an aperiodic boundary was evenly discretized into 500 populations. Within each of these fields, a 'typical' principle cell was described by the following conductance model

$$C\frac{\partial V}{\partial t} = \sum_i g_i(E_i - V) + I_\xi + I_{ext} \qquad (5.1)$$

Where V was the mean membrane potential and C was cell capacitance. Four types of conductances (g) were modelled: leak (g_L), glutamatergic synaptic (g_E), GABAergic synaptic (g_I), and slow potassium conductance (g_K). E_i represented each conductance's reversal potential. I_ξ was the randomly fluctuating background input coming from outside the modeled network, with amplitude σ_ξ. Spatiotemporal autocorrelations in the background input were generated by Ornstein-Uhlenbeck processes with time and spatial constants, τ_ξ and λ_ξ, respectively. I_{ext} represented external focal constant current inputs for seizure initiation. The amplitude, location, and duration of current injection are reported in each figure's legends. Each population's averaged instantaneous firing rate, f, was obtained by passing the difference between the typical cell's membrane potential, V, and its firing threshold, ϕ, through a sigmoid function, $f(v) = \frac{f_{max}}{1+\exp(-v/\beta)}$, where $v = V - \phi$; β controled slope of the sigmoid function, and f_{max} is maximal firing rate. The threshold was dynamic and its steady state was linearly dependent on firing rate via Δ_ϕ

$$\tau_\phi \frac{\partial \phi}{\partial t} = (\phi_0 - \phi) + \Delta_\phi f \tag{5.2}$$

where ϕ_0 represented the baseline firing threshold. The reversal potential of GABAergic

conductance (g_I) depended on the transmembrane chloride gradient. Intracellular chloride

concentration was determined by two counteracting mechanisms: chloride current influx and a

first-order kinetics clearance mechanism (Zhu, Lovinger et al. 2005),

$$\frac{\partial [Cl]_{in}}{\partial t} = I_{Cl} + \frac{[Cl]_{in,eq} - [Cl]_{in}}{\tau_{Cl}} \tag{5.3}$$

Where I_{Cl} was chloride flow through GABA-A receptors, $I_{Cl} = \frac{g_{Cl}(V - E_{Cl})}{V_d F}$. V_d was volume of

distribution of intracellular chloride (Marchetti, Tabak et al. 2005, Vladimirski, Tabak et al.

2008), F was Faraday's constant, τ_{Cl} was the time constant for clearance mechanisms (Deisz,

Lehmann et al. 2011), and $[Cl]_{in.eq}$ was the equilibrium intracellular chloride concentration. The

steady state of the slow adaptation conductance, g_K, was also linearly dependent on firing rate

via Δ_K and evolved with simple first-order kinetics,

$$\tau_K \frac{\partial g_K}{\partial t} = -g_K + \Delta_K f \tag{5.4}$$

However, τ_K was significantly slower than threshold adaptation and operated in the time scale of

seconds (Table 5.1).

Neurons in the model were recurrently connected via "Mexican-hat" connectivity (Figure

5.1A). Recurrent excitation, g_E, was computed by first convolving the normalized firing rate,

$A = \frac{f}{f_{max}}$, with a spatial Gaussian kernel ($K_E \sim N(0, \sigma_E^2)$), $\int_{-\infty}^{+\infty} A(x - s, t) K_E(s) ds$. The results

were further temporally filtered to model synaptic delay (single exponential with time constant

τ_E) and then multiplied by the strength of recurrent excitation, $\overline{g_E}$. Recurrent inhibition was modelled analogously. The inhibitory kernel had a wider spread than the excitatory kernel and could be partitioned into spatially localized and non-localized parts. $K_I \sim (1 - \gamma)N(0, \sigma_I^2) + \gamma U$, where U was a uniform distribution over the whole space (normalized length = 1) and γ controled the relative contribution of the localized versus non-localized elements of recurrent inhibition. All rate models and the following simulations were done with dt=1 ms.

5.2.2 Spiking model

2000 neurons with membrane potentials modeled analogously to equation (1) were evenly distributed along a bounded one-dimensional space. Spikes were emitted probabilistically with instantaneous firing rate, $f = f_s \exp(\frac{V-\phi}{\beta})$, where f_s quantified the activation slope and β represented threshold noise. Numerically, spikes were generated by a Bernoulli process for each time step, $dt = 1$ ms. If a spike was emitted, membrane potential was set to +40 mV for 0.5 ms and then reset to 20 mV below the pre-spike membrane potential. During the following refractory period (τ_{ref}), membrane potentials were allowed to evolve but spiking was prohibited by setting $f = 0$. Analogous to equation (2), threshold increased by Δ_ϕ immediately after a spike and exponentially decayed with time constant τ_ϕ. Chloride dynamics, slow potassium conductance, and recurrent projections were also modeled analogously.

5.2.3 Spike-timing dependent plasticity (STDP)

Recurrent excitation was subject to STDP (Bi and Poo 1998, Song, Miller et al. 2000). In this model, the recurrent weight matrix, W_E, was first initiated as the convolution matrix of an excitatory kernel, K_E. Plastic synaptic weights were then considered by $W_E \leftarrow W \odot W_E$ (Toyoizumi, Kaneko et al. 2014), where W was subject to STDP and $\odot$ was element-wise multiplication. Every entry of W was initiated as 1. After each seizure, the plastic part of synaptic projection from neuron b to a, W_{ab}, was updated by the rule,

$$\Delta W_{ab} = W_{ab} + \eta \int \rho_a(t)\rho_b(t+s)K_{STDP}(s)ds \qquad (5)$$

where ρ represented spike trains during the seizure, η was the learning rate, and K_{STDP} was an asymmetric exponential kernel with time constant τ_{STDP}. The learning rate was set so that a single seizure episode maximally changed synaptic weights by 1/3.

5.2.4 LFP in the spiking model

LFP was modeled by the reference weighted sum proxy method (Mazzoni, Linden et al. 2015). Briefly, LFP was modeled to be proportional to a linear combination of excitatory and synaptic currents, $I_E - \alpha I_I$, where $\alpha = 1.65$ and I_E is temporally delayed by 6 ms. Contribution from neighboring cells decayed exponentially with spatial constant $\sigma_{LFP} = 0.025$ (unit: normalized space).

5.2.5 Phenomenological model

We developed an abstract model to describe exhaustible inhibition. The model was exactly the same as the rate model, except the inhibitory synaptic currents were not explicitly

modeled as a function of transmembrane chloride gradient. Instead, an abstract dynamic variable, z, was used to quantify the effectiveness of local inhibition: $g_I(x,t) \leftarrow zg_I(x,t)$. z therefore generally represented numerous factors that could contribute to inhibition effectiveness, including chloride gradient, interneuron excitability, short-term plasticity, etc. z followed simple first-order kinetics

$$\tau_z \frac{\partial z}{\partial t} = z_\infty - z \tag{5.6}$$

Where its steady state, z_∞, depended on inhibition usage, $z_\infty = H(g_{I.th} - g_I)$. H was Heaviside step function. While strong inhibition was used (above $g_{I.th}$), local inhibition effectiveness decreased with time constant τ_z.

5.2.6 Two-dimensional model

The rate model was extended to a bounded, round-shape two-dimensional space. Along the diameter, the space was evenly partitioned into 50 populations (100 for higher image quality in Figure 1). Recurrent projection was calculated by two-dimensional convolution, $K_E \sim N(0, \sigma_E^2 I_2)$ and $K_I \sim (1-\gamma)N(0, \sigma_I^2 I_2) + \gamma U$. A round space was used in order to avoid inhomogeneous boundary effects along various directions.

5.2.7 Measuring seizure activity in model and patient recordings

For rate models, the spatiotemporal extent of a focal seizure was defined as the convex hull of a set of time-space points, $\{(x,t)|f(x,t) > 0.1f_{max}\}$. Ictal activity ($> 0.1f_{max}$) needed

to last more than 3 seconds independently for an ictogenic input to be considered successful. Seizures were partitioned into the following phases: pre-ictal, ictal-tonic (after successful seizure initiation), ictal-clonic (after emergence of repetitive bursting region), pre-termination (after disappearance of all tonic-firing regions), and post-ictal. Transitions between them were identified visually.

Traveling wave velocities were calculated by least squares linear regression (Liou, Smith et al. 2017). For patient data, velocity was inferred by regressing multiunit spike timing against spatial information (significance level = 0.05). For rate models, timing of firing rate peaks were regressed (significance level $=10^{-3}$). Circular standard deviation (20-second window) quantified traveling wave direction variability.

Spiral waves centers were identified by finding phase singularity points (Iyer and Gray 2001). At a given time t, a population's instantaneous phase, $\psi(x, t)$, was estimated according to its state in the membrane potential – threshold plane. $\psi(x, t) = angle(V(x, t) - V_m(x) + i(\phi(x, t) - \phi_m(x)))$. $V_m(x)$ and $\phi_m(x)$ were the median voltage and threshold throughout the whole seizure episode at location x. Singular points were found by looking for a closed-path, l, that circulated the immediately surrounding points, where $\oint_l \nabla \psi \cdot dl = \pm 2\pi$.

Table 5.1 Parameters for rate models.

Parameters		unit
C	100	pF
g_L	4	nS
$\overline{g_E}$	100	nS
$\overline{g_I}$	300	nS
E_L	-57	mV
E_E	0	mV
E_K	-90	mV
f_{max}	200	Hz
β	2.5	mV
τ_E	15	ms
τ_I	15	ms
τ_ϕ	100	ms
ϕ_0	-45	mV
Δ_ϕ	0.3	mV/Hz
τ_{Cl}	5	second
V_d	0.24	pL
$[Cl]_{in.eq}$	6	mM
$[Cl]_{out}$	110	mM
τ_K	5	second
Δ_K	0.2	nS/Hz
σ_E	0.02	
σ_I	0.03	
γ	1/6	

Neurons are modelled analogous to neocortical pyramidal neurons in terms of cell capacitance, leak conductance, and membrane time constant (Tripathy, Savitskaya et al. 2014). Maximal synaptic conductance during seizures have been reported in the range of lower hundreds of nS (Neckelmann, Amzica et al. 2000). Chloride clearance (Deisz, Lehmann et al. 2011), buffer (Marchetti, Tabak et al. 2005), and seizure-induced sAHP conductance (Alger and Nicoll 1980) were all modeled in the reported ranges. The existence of non-localized cortico-cortical projections (γ) were modelled as reported previously (Braitenberg and Schüz 2013).

Table 5.2 Parameters for spiking models

Parameters		unit
C	100	pF
g_L	4	nS
g_E	100	nS
g_I	300	nS
E_L	-57	mV
E_E	0	mV
E_K	-90	mV
f_s	2	Hz
β	1.5	mV
τ_{ref}	5	ms
τ_E	15	ms
τ_I	15	ms
τ_ϕ	100	mV
ϕ_0	-55	mV
Δ_ϕ	2	mV
τ_{Cl}	5	Second
V_d	0.24	pL
$[Cl]_{in.eq}$	6	mM
$[Cl]_{out}$	110	mM
τ_K	5	Second
Δ_K	0.04	nS
σ_E	0.02	
σ_I	0.03	
γ	1/6	
τ_{STDP}	15	ms
η	1/300	

Parameters are chosen as described in Table 1's legends. Spike-timing dependent plasticity time

constant was chosen in the time scale reported in previous experiments (Bi and Poo 1998).

5.3 Results

Microelectrode array recordings from two pharmaco-resistant focal epilepsy patients demonstrated multiunit firing patterns indicative of seizure invasion (Schevon, Weiss et al. 2012, Smith, Liou et al. 2016). Figure 5.1 compares multielectrode array recordings from Patient A (right posterior temporal lobe) with the results of a two-dimensional rate model simulation. The patient recording shows a narrow band of tonic firing, approximately 1 mm wide, just after seizure onset (Figure 5.1B, left). The seizure territory slowly expanded as the tonic-firing band, termed the 'ictal wavefront', advanced. Seconds later, neurons inside the territory, behind the ictal wavefront, transitioned into repetitive bursting. Bursts propagated sequentially from the ictal wavefront backward to the internal domain, constituting the fast-moving 'backward traveling waves' (Figure 5.1C, left). The two-dimensional model, after being triggered by an ictogenic stimulus (red star in Figure 5.1B), reproduced all of the key dynamics that were observed in the patient recording – including the slow-marching wavefront (Figure 5.1B, right) and fast backward-moving traveling waves (Figure 5.1C, right).

Figure 5.1 Model schematics and the comparison of patient recordings and model simulation results.
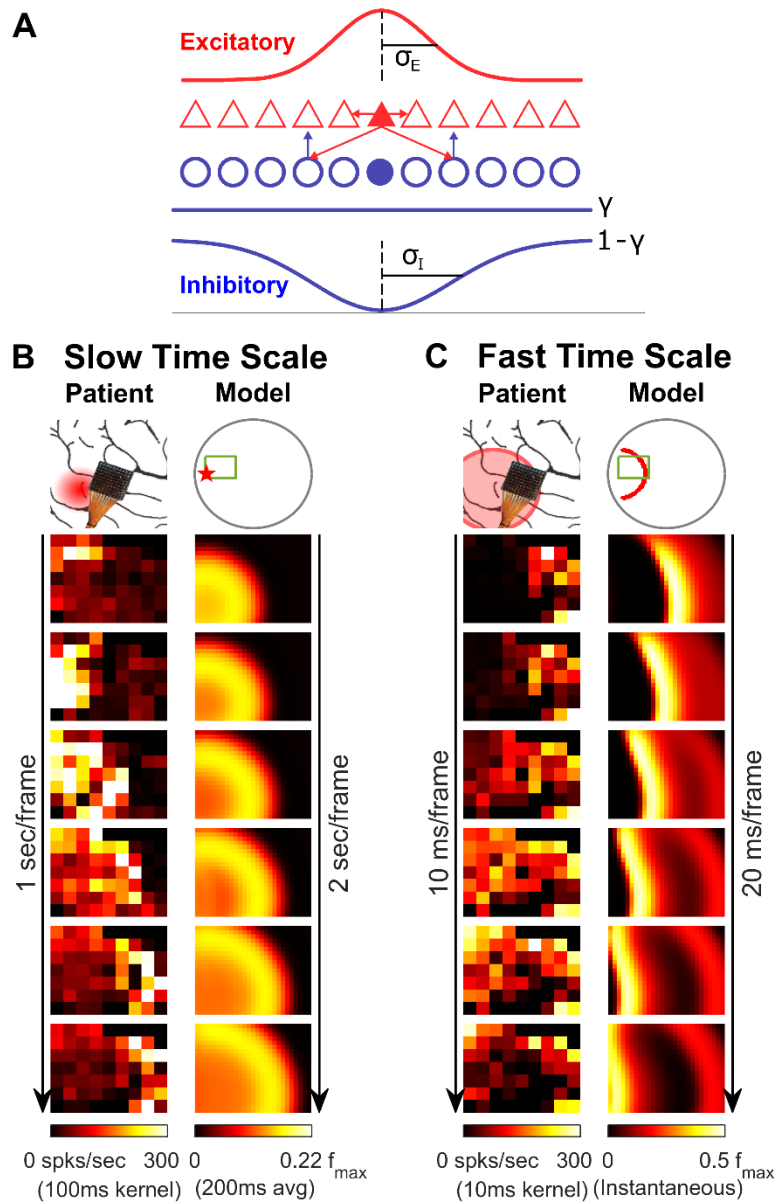
A) Model schematic. Triangles: excitatory (E) neurons. Blue circles: inhibitory (I) neurons.

Equations 1 to 4 modelled E neuron dynamics. E neurons recurrently connected with

each other via direct projections (red, spatial kernel width:σ_E). E neurons exerted

inhibitory effects to each other via indirect projections, mediated by I neurons. E-to-I

projections included two parts: spatially localized (width:σ_I) and non-localized. I

neurons collected γ non-localized and $1 - \gamma$ localized projections from E neurons,

linearly transformed them and projected onto their corresponding E neurons via

GABAergic synapses.

B) Expansion of the ictal core with the slow marching ictal wavefront. Left column: Patient

A recording – multielectrode array was implanted at right temporal-parietal junction.

Red shaded area: seizure onset zone. Firing rate was estimated by a 100 ms kernel to

show slow expansion of seizure territory. Right column: simulation. Red star – seizure

onset spot, where an external excitatory input was injected. The green rectangle

indicated where the following images showed. Firing rate was normalized by maximal

firing rate, f_{max}, and averaged over 200 ms to show the slow marching wavefront.

Supplementary movie 1 showed the whole field with complete seizure evolution.

C) Backward traveling wave emitted from the edge of seizure territory. Left column: patient

recording. Red shaded area: seizure territory. Red rim: the wavefront. Right column:

simulation. Red rim of the schematic: edge of seizure territory. Notice both showed fast-

moving backward traveling waves.

5.3.1 Phasic evolution of focal seizures

      To increase simulation precision and simplify topological considerations, we reduced our model's dimensionality from two to one (Figure 5.2). The simplified 1D model also shows Jacksonian-like slow expansion (Figure 5.2A) and fast backward traveling waves (Figure 5.2B), with a speed ratio ($\approx$200) that is compatible with the range previously reported from human recordings (1 mm/sec versus 20$\sim$50 cm/sec) (Smith, Liou et al. 2016, Liou, Smith et al. 2017). Moreover, sequential stages of seizure evolution can be discerned. After receiving a transient external stimulus, establishment of a self-sustaining tonic-firing region, i.e. an activity bump, marks seizure initiation. The tonic firing bump transitions spontaneously to repetitive neuronal bursting, marking the onset of the ictal-clonic phase. After a period of ictal wavefront expansion with associated backward traveling discharges, the ictal wavefront spontaneously dissipates. Annihilation of the wavefront marks the transition into the pre-termination phase. After the last burst propagates across the territory, the seizure terminates abruptly. All these seizure phases can be identified in both the simplified 1D and the full 2D model. Phasic transitions, with all the characteristic dynamics, were also seen in a spiking model (Figure 5.3).

Figure 5.2. Phasic evolution of focal seizures
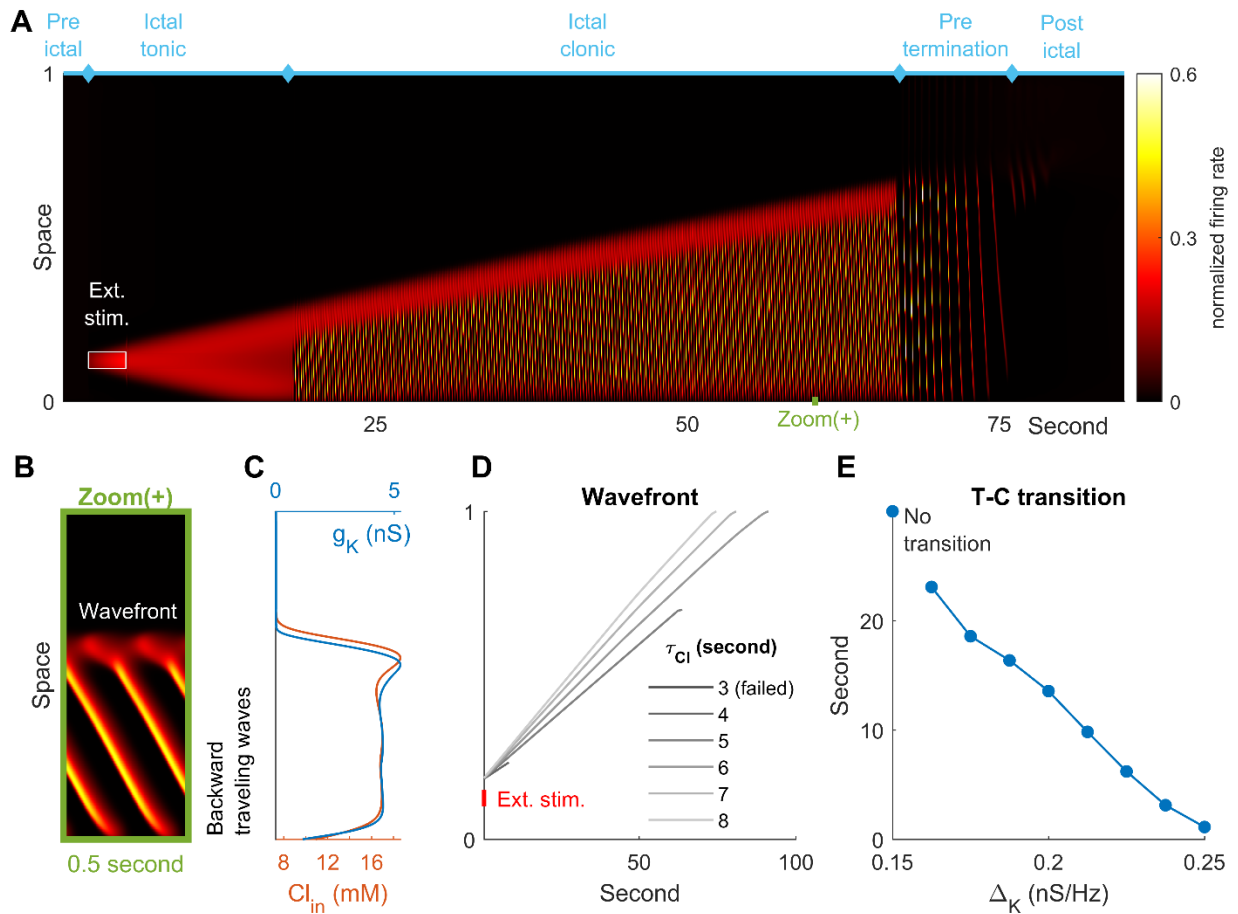
A) Spatiotemporal evolution of a one-dimensional model. The dynamics could be separated

into the following distinct phases: pre-ictal, ictal-tonic, ictal-clonic, pre-termination, and

post-ictal. Seizure was initiated by an external stimulus (white box, 200 pA). After

tonic-to-clonic transition, seizure territory could be partitioned into the tonic-firing edge

(wavefront) and internal bursting domain (backward traveling waves). Annihilation of

wavefront lead into pre-termination phase. After the last burst, the field entered post-ictal

phase.

B) Temporal zoom-in during the ictal-clonic phase. Notice the fast-moving traveling waves moved backward. Speed: 1.36 normalized space unit per second. Expansion speed of wavefront: 0.008 normalized space unit per second.

C) Intracellular chloride concentration and sAHP conductance distribution during ictal-clonic phase (as B). Notice sequential activation of the two processes.

D) Impaired chloride clearance allowed seizure initiation and sped up propagation. Gray lines: the upper edge of seizure territory. End of the lines: seizure termination, either spontaneously ($\tau_{Cl} \leq 5$ seconds) or after meeting the boundary ($\tau_{Cl} \geq 6$ seconds).

E) Activation of sAHP lead tonic-to-clonic transition. Duration of ictal-tonic phase monotonously decreased as potassium conductance increased (Spearman's correlation coefficient = -1).

Figure 5.3 A corresponding spiking model reproduced phasic transitions and characteristic

dynamics.
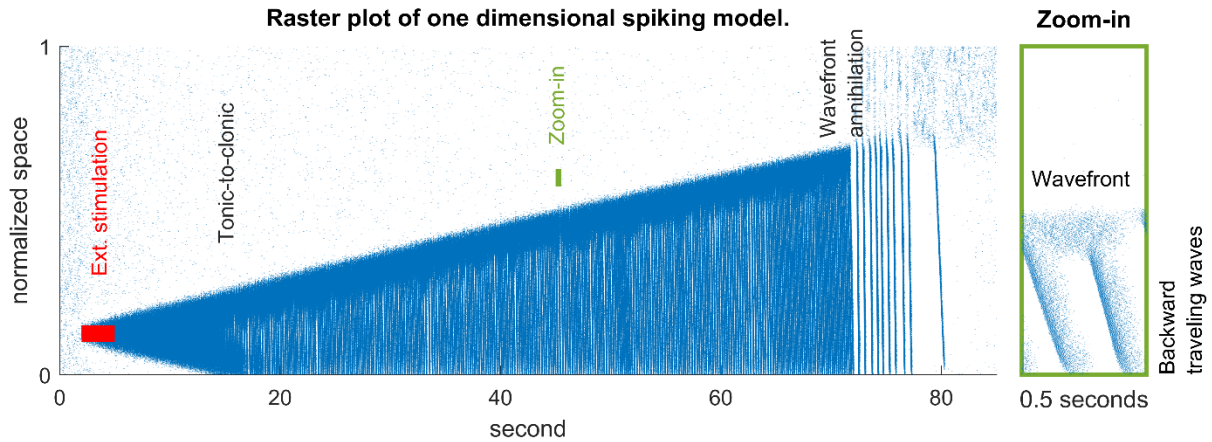
Raster plot of a corresponding spiking model to Figure 5.2's model. Each blue dot indicates an

action potential occurred at that point in space and time. E_L=-57.25 mV, β=2.5 mV. Red box: the

external ictogenic input, 200 pA. The seizure territory slowly expanded, generating backward

traveling waves following the phasic transition sequences as shown in Figure 5.2A.

5.3.2 Physiology of the ictal wavefront

The slow advance of the ictal wavefront in the model results from sequential activation of

two slow variables: the intracellular chloride concentration and the sAHP conductance (Figure

5.2C). Initially, surround inhibition blocks seizure propagation. However, immediately ahead of

the wavefront, intracellular chloride starts to accumulate due to strong disynaptic feedforward

inhibition projected from the seizing territory. Collapse of the transmembrane chloride gradient,

which compromises the strength of inhibition, presages seizure invasion. Following seizure

invasion, intense firing activates the sAHP conductance, which decreased neuronal excitability.

Consequently, the tonic firing of the ictal wavefront transitions into repetitive bursts that travels backward into the ictal core.   Modulating chloride clearance in order to ramp up the robustness of inhibition results in decreased seizure propagation speed, reduced seizure duration, and failed seizure initiation if chloride can be pumped out fast enough (Figure 5.2D). A similar study confirmed the role of sAHP in tonic-to-clonic transitions. Strong sAHP conductance hastens the transitions and, in extreme cases, results in failed seizure initiation.

5.3 Ictal wavefront annihilation and the pre-termination phase

As the seizure territory expands, the ictal wavefront in the model encounters increasingly stronger inhibition ahead of itself. This is because spatially widespread, non-localized di-synaptic inhibition has been progressively activated (the 1-γ part of recurrent inhibition). This works like a spatial integrator counting the size the space that has been invaded. Consequentially, seizure propagation slows. Once the propagation speed is inadequate to escape from sAHP-induced suppression, the wavefront is annihilated, and the seizure transitions into the pre-termination phase (Figure 5.2A & 5.4).

The pre-termination phase is characterized by irregular and gradually increasing inter-discharge intervals, as was observed in our patient recordings and has long been observed clinically (Figure 5.4B-E). Prolonged interburst intervals give the cells more time to remove their previously accumulated chloride. As the transmembrane chloride gradient is gradually restored, inhibition strength recovers. Recovered inhibition attenuates burst intensity (Figure 5.4C), slows backward traveling waves (Figure 5.4D), and desynchronizes neuronal populations (Figure 5.4E).

Figure 5.4 Pre-termination phase shows the 'slowing-down' dynamics
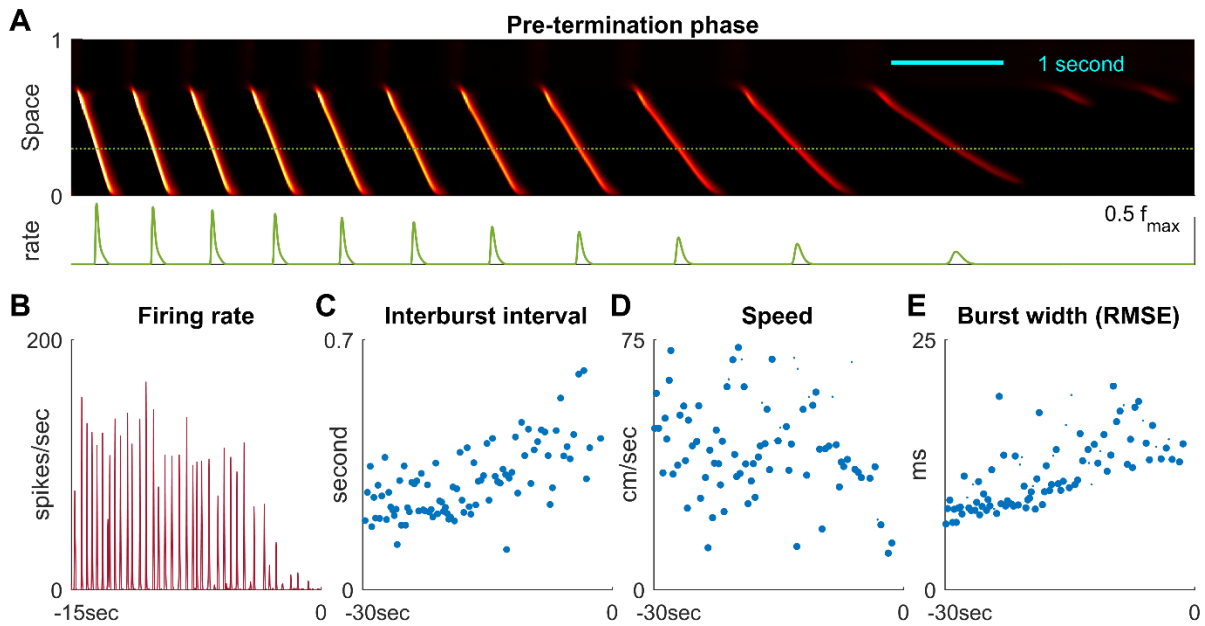
A) Pre-termination phase as enlarged from Figure 5.2A. Instantaneous firing rate at the
position marked by dotted green line was plotted in the lower subpanel. Locally (green
line), as seizure approached termination, maximal firing rate decreased, interburst
interval prolonged, burst width increased, and traveling wave speed (upper subpanel,
slope of the traveling waves) slowed.

B) B-E) A sample seizure recorded from Patient B during pre-termination phase. Maximal
firing rate decreased, interburst interval increased, traveling wave speed decreased, and
burst width increased, as predicted from Panel A. Spearman's correlation coefficients: -
0.62 (p<0.001), 0.64 (p<0.001), -0.34 (p=0.002), 0.78 (p<0.001) for B-E respectively.

Although pathological chloride accumulation is an appealing candidate mechanism for usage-dependent exhaustion of inhibition, several other mechanisms have also been proposed, such as depolarization block of inhibitory neurons (Meijer, Eissa et al. 2015). We hypothesized that any mechanism that compromises inhibition strength in a few seconds under intense, prolonged usage could be a candidate mechanism for the slow expansion of seizure territory. To confirm our hypothesis, we modeled a general inhibition exhaustion process (equation 5.5). All evolutionary stages of focal seizures and their characteristic dynamics could be reproduced in this way (Figure 5.5).

Figure 5.5 Simulation results of the phenomenological model.
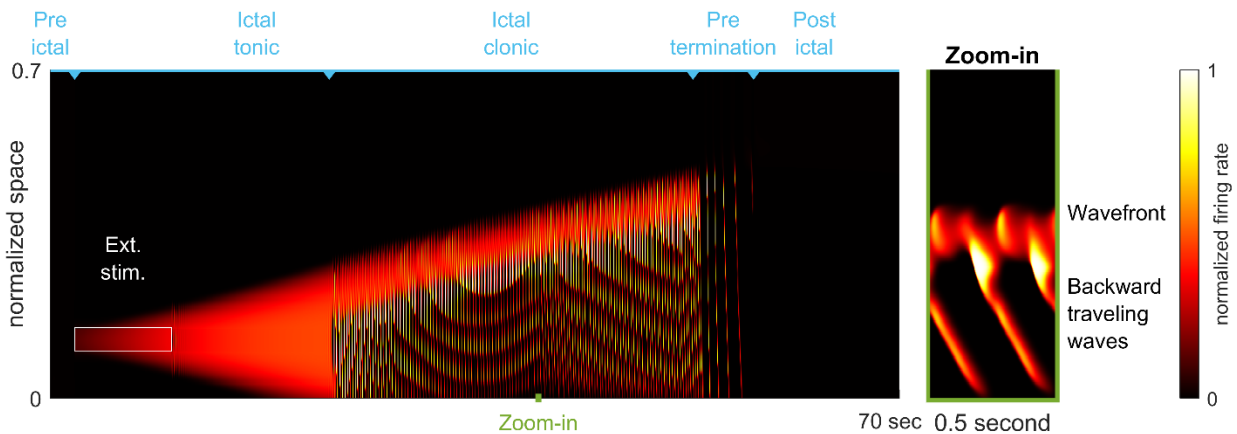
Figure conventions were adopted from Figure 5.2A. Phasic evolution and characteristic dynamics can be seen. Parameters were adopted from Table 1 with the following adjustments: Δ_K=0.125 nS/Hz; τ_K=7 seconds; $g_{I.th}$=15 nS; $\overline{g_E}$=125 nS; E_L=-60 mV. External stimulation strength: 200 pA.

5.5 Seizure onset pattern explained by distribution of recurrent inhibitory projections

We have thus far shown that minimal neurophysiologically based assumptions can account for complex spatiotemporal evolution of focal seizures. By estimating LFPs from our spiking model, we can provide insights into the mechanisms of different focal seizure onset patterns. Low-voltage fast activity (LVFA) is the most common onset pattern, with rhythmic discharges or slow rhythmic oscillations seen in other instances (Perucca, Dubeau et al. 2014). We hypothesized that seizure onset patterns are determined by the distribution of recurrent inhibitory projections (Figure 5.6 & Figure 5.7). When recurrent projections favor strong localized inhibition, focal LVFA is produced (Figure 5.6A, local versus global recurrent inhibition 5:1). The onset pattern shifts to rhythmic discharges when the distribution of recurrent inhibition favors spatially non-specific projections (Figure 5.6B, local versus global recurrent inhibition 1:1). Under this condition, inadequate local restraint allows ictogenic perturbation to ripple outward in the form of forward traveling waves. The model predicted that forward waves travel slower than backward waves, because inhibition is initially intact (Figure 5.6B), an observation in accord with the measurements of traveling wave speeds from microelectrode array recordings of human focal seizures (Smith, Liou et al. 2016, Liou, Smith et al. 2017). Furthermore, in the case of rhythmic discharge seizure onsets, and again mimicking dynamics observed in the human recordings, travelling waves switch direction and accelerate on either side of the ictal wavefront (Figure 5.6C).

Figure 5.6. Forward traveling waves with rhythmic onset could arise due to inadequate local inhibition.
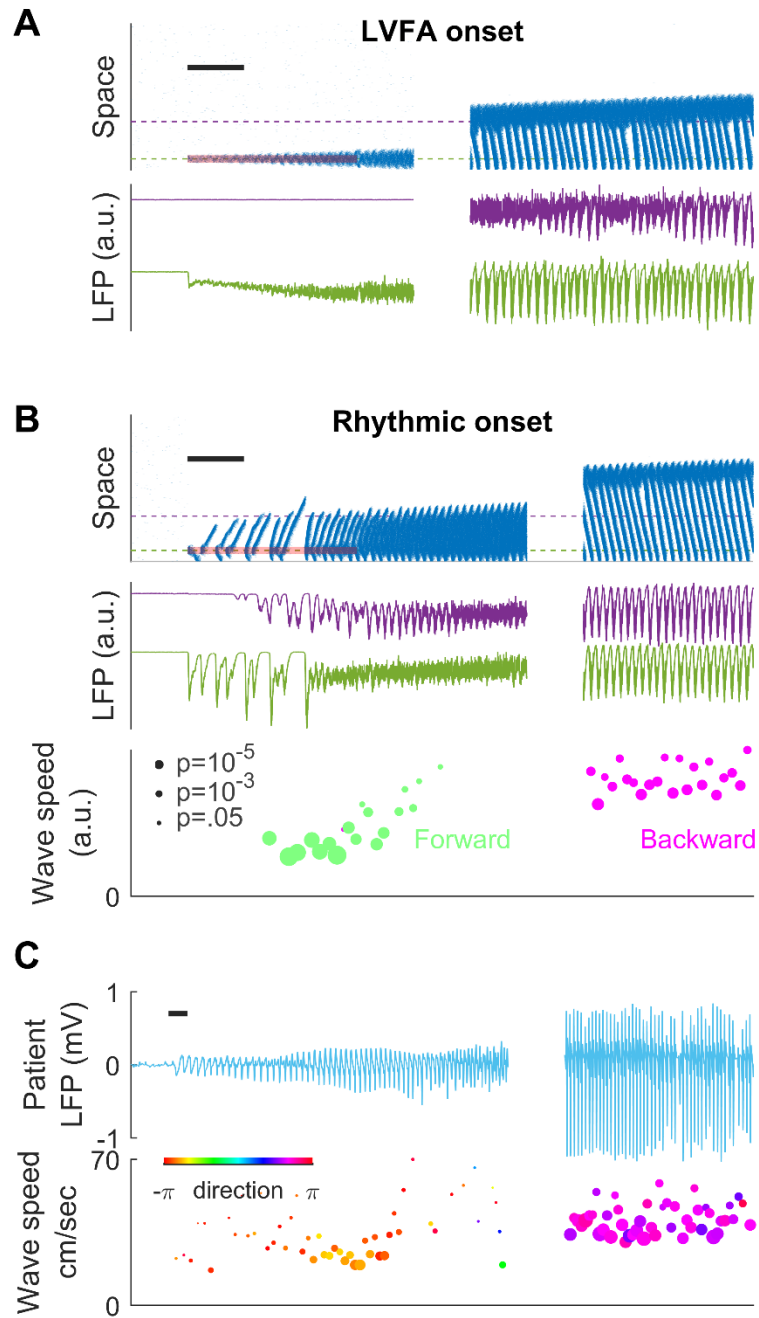
A) Low-voltage fast activity (LVFA) during seizure onset (E_L=-60mV). Time scale (black): 1 second. Upper panel: raster plot. $\gamma = 1/6$. Shaped reddish zone: external input = 80 pA. Green and purple dashed lines indicated where the LFPs, shown in the lower subpanel, were recorded. Blank: 20 seconds. Notice LVFA with large LFP DC shift corresponded with seizure onset and wavefront invasion. After ictal wavefront passed, LFP evolved into periodic discharges.

B) Rhythmic seizure onset. $\gamma = 1/2$. Figure conventions as Panel A. Blank: 15 seconds. Several forward traveling wave-associated LFP discharges preceded wavefront invasion (fast activity). Traveling wave speed were measured locally along the purple dashed line. Results were plotted in the lower subpanel. Dot size corresponded with F-test p-Value and color represented traveling direction. Null hypothesis was rejected if p<0.001. Forward traveling waves were slower than backward waves (U-test, p<0.001).

C) Rhythmic seizure onset recorded from Patient B. Time scale bar (black): 1 second. LFP was averaged across the whole array. Traveling wave velocities were estimated according to the spatiotemporal distribution of multiunit spikes. Seizure started with periodic LFP discharges, some of which associated with traveling waves. Blank: 40 seconds. As seizure evolved, traveling wave direction switched and accelerated (U-test p<0.001) (Smith, Liou et al. 2016, Liou, Smith et al. 2017).

Figure 5.7 Local environment determined onset, propagation and termination patterns
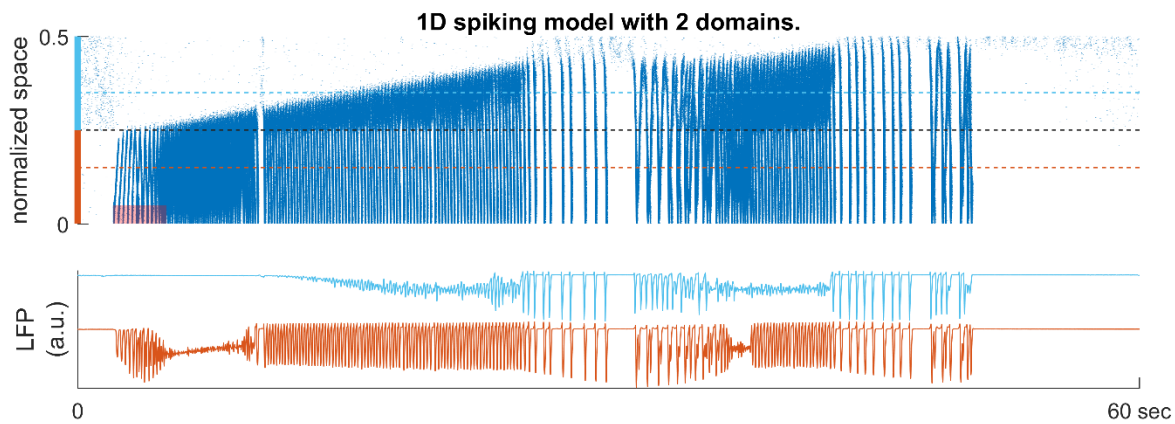
The upper part of the space was configured as Figure 5.3, whereas the lower part configured as

Figure 5.6B. The gray dashed line indicates the boundary between the two domains. The light

blue and orange dashed lines indicate where the LFPs were recorded from. The transparent red

rectangle was where 80 pA external current was injected. The seizure approached termination

two times, failing to terminate the first time. Forward traveling waves with rhythmic LFP

discharges could be seen near the position of the first seizure's onset (inadequate local inhibition);

whereas LVFA and pre-termination slowing originated from the more eccentric position.

5.3.6 Spike-timing dependent plasticity (STDP) and spontaneous seizure generation

Synaptic plasticity has been implicated in epileptogenesis, although the process by which

it reduces seizure threshold remains unknown (Mehta, Dasgupta et al. 1993, Reid and Stewart

1997, Scharfman 2002). We investigated how synaptic plasticity affects seizure dynamics in our

1D spiking model. After a provoked LVFA seizure (Figure 5.8A), the backward traveling waves

induced a centripetal restructuring of connectivity (Figure 5.8B). This centripetal E-to-E

connectivity could be epileptogenic. As shown in Figure 5.8C, centripetal connectivity allows

normal-range physiologic background input to evoke centripetal traveling waves. The

background input is therefore redirected toward the centripetal connectivity center; consequently,

another LVFA seizure spontaneously emerge (Figure 5.8C, see its legend for noise parameters).

The second seizure further reciprocally enhances the centripetal connectivity by exposing it to

more backward traveling waves. A chronic epileptic focus is thereby established.

     Centripetal traveling waves could be observed in our patient recordings before seizure

onset, manifested as the clinically recognized phenomenon of herald spikes, i.e. large

epileptiform discharges resembling those seen interictally, but immediately preceding seizure

onset. Figure 5.8D shows a microelectrode recording of a human LVFA seizure (Patient A)

preceded by herald spikes, demonstrating centripetal traveling waves. As shown in Figure 5.8D-

E and Figure 5.9, herald spike-associated multiunit firing traveled in the opposite direction of

seizure propagation (Figure 5.8D, inset). We also observed seizure initiation from the same

region, as predicted by our plasticity simulation study. Indeed, the propagation sequence of

Patient B's three seizures (anterior inferior temporal lobe) were all highly similar (Figure 5.8F-G,

see legend for statistics). These results indicate that, as observed in the biophysically constrained

model, the origination point of all three events was constant relative to the microelectrode

recording site.

Figure 5.8 Herald spikes and seizure progression explained by STDP
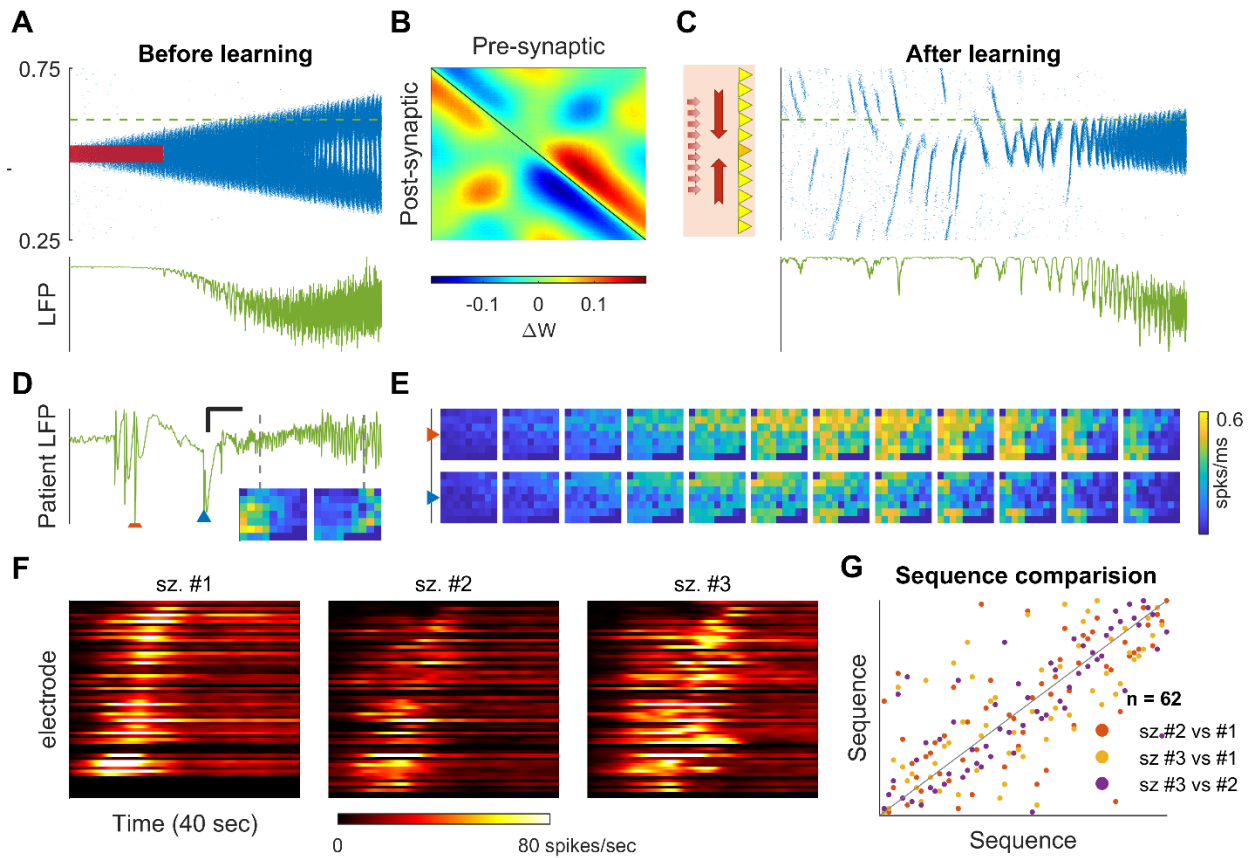
A) Raster plot of a seizure induced by an external excitatory stimulus (red area, 3-second, 200 pA). The green dashed line indicates where the LFP, shown in the lower subpanel, was recorded. LFP at seizure onset showed LVFA activity with DC shift. Δ_K=0.05 nS.

B) Changes in connectivity strength induced by STDP. A centripetal pattern was induced by exposure to backward traveling waves.

C) Spontaneous seizures developed after STDP learning (σ_ξ=20 pA, λ_ξ=0.1, τ_ξ=15 ms). Centripedal traveling waves produced epileptiform discharges before the emergence of LVFA activity.

D) LFP recording during the seizure onset (Patient A). Several herald spikes preceded LVFA onset. For the herald spikes marked with colored triangles, evolution of their associated multiunit firing patterns were shown in Panel E. Inlet: instantaneous firing rate (10-ms kernel) showed expansion of seizure territory followed left to right order. Scale bars: 1 second, 0.5 mV.

E) Multiunit firings constituted centripedal traveling waves (10 ms kernel) during herald spikes. Notice the right half of the array detected multiunit firings earlier than the left half. For detailed statistics, see Supplementary Figure 4.

F) Repetitive seizures followed the same invasion sequence (Patient B). Seizure #2 happened 37 hours 13 minutes after seizure #1. Seizure #3 happened 5 hours 32 minutes after seizure #2. Each row showed evolution of firing rates recording from one electrode during a seizure (1-second kernel, 62 electrodes). Electrode sequence was sorted according to the sequence of detecting maximal firing rates based on data from seizure #1. Sequence was fixed for displaying seizure #2 and #3 data. Notice their similar sequences of invasion.

G) Quantification of similarity in Panel F. Spearman correlation coefficients = 0.67, 0.72, and 0.8 for the three sequence comparisons respectively ($p < 0.001$ in all cases).

Figure 5.9 Herald spikes as centripedal traveling waves.
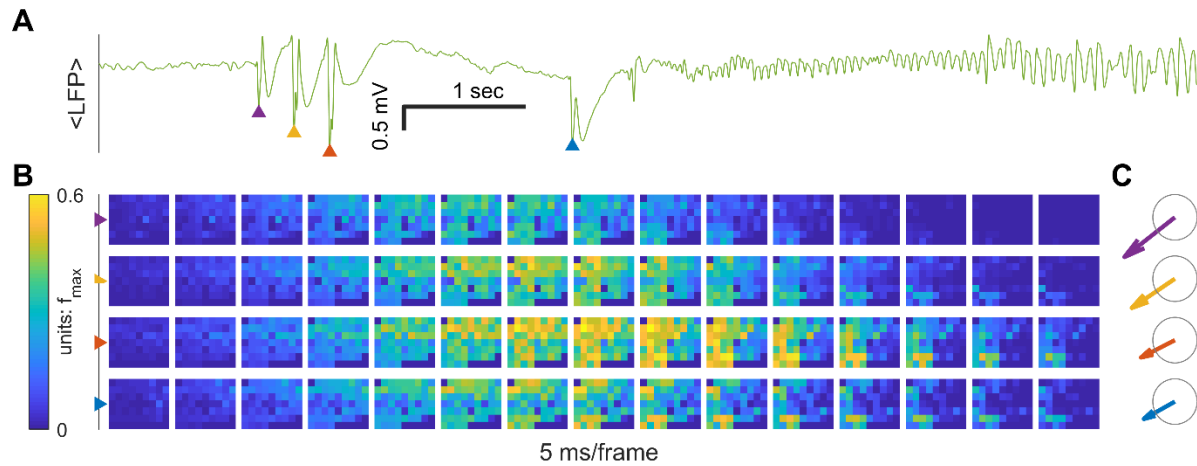
A) Averaged LFP of the sample patient seizure. Before appearance of LVFA, 4 herald spikes
   were found and marked with triangles, whose color indicated which row of data in Panel
   B they corresponded to.

B) Spatiotemporal evolution of instantaneous firing rate estimated by a 10 ms Guassian
   kernel. For all herald spikes, multiunit spikes were detected earlier at the upper right
   corner than the left lower corner

C) Traveling wave velocities estimated by the linear regression method. F-test of all four
   episodes rejected null hypothesis (standing waves), $p < 0.001$. Gray circle: 10 cm/sec.

5.3.7 Variability of traveling wave directions under noisy conditions

To study traveling wave direction variability in epileptic cortices, we returned to our two-dimensional models (Figure 5.10). In a circular neural sheet under noise-free condition, the ictal wavefront from a seizure evoked at the center expands as a perfect circle. All backward traveling waves are directed in a centripetal pattern towards the center point, with no direction preference (Figures 5.10A). From the vantage point of any position within the seizing territory, the traveling wave could therefore come from any direction. However, investigations of traveling waves in human recordings clearly demonstrated preferred traveling wave directions (Smith, Liou et al. 2016, Liou, Smith et al. 2017, Martinet, Fiddyment et al. 2017). To rectify this discrepancy and in light of the numerous noise sources in vivo, we studied the effects of noise in our model.

It might seem that adding random perturbations in our model would make traveling waves flip randomly, which would further contradict in vivo observations. Paradoxically, in our model, a preferred direction can emerge from uniformly distributed spatiotemporally white noise (Figure 5.10B) without any spatial asymmetry or inhomogeneities in the neuronal properties. After the tonic-to-clonic transition, added noise at first biases the traveling wave confluence points (Figure 5.10C). However, once established, the bias persists, creating a traveling wave direction preference that is sustained throughout the seizure. After wavefront annihilation, traveling wave directions start to randomly fluctuate and flip (Figure 5.10D). Such variable wave directions mimic human seizure recordings, as an increase in the variability of wave directions before seizure termination is seen in patient recordings (Figure 5.11). This increase in variability further supports the model prediction that the pre-termination period is associated

with annihilation of the ictal wavefront, yet it also accounts for the relative consistency of pre-termination wave directions.

Figure 5.10 Consistent backward traveling wave direction emerges from white noise
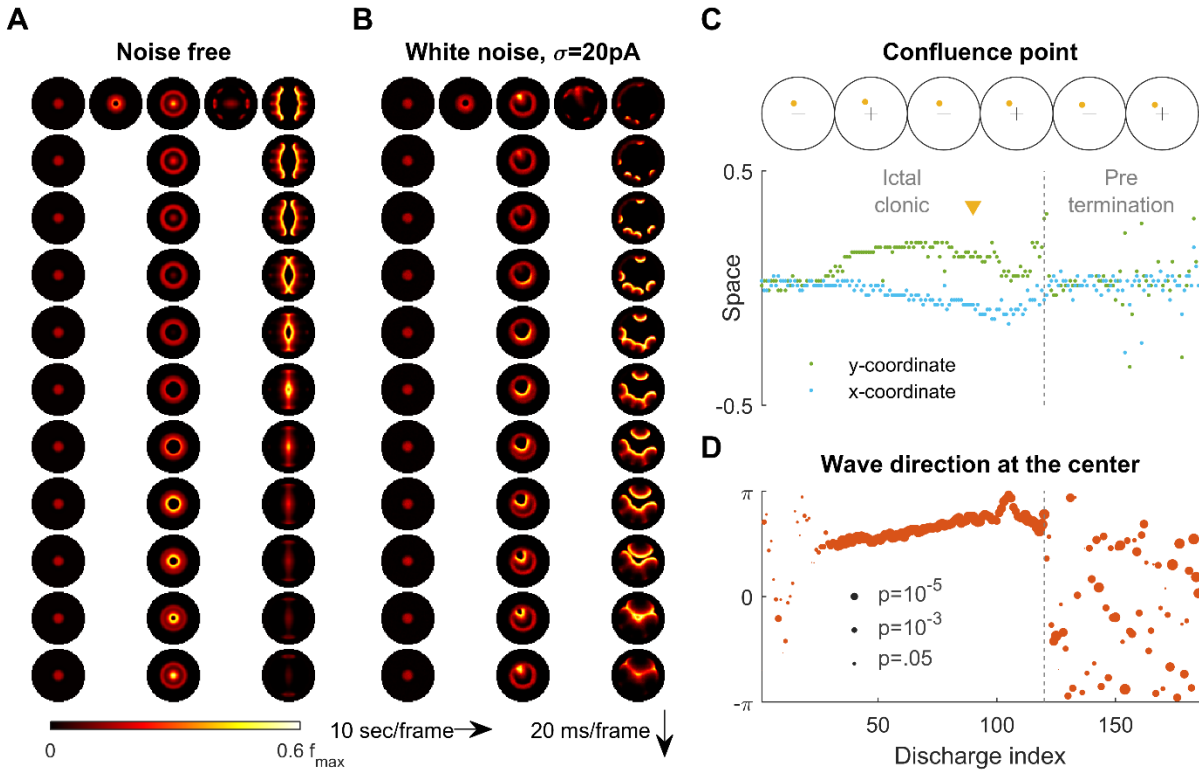
A) Simulation results of a spatially bounded, two-dimensional rate model under noise free condition. Ictogenic stimulus was given at the round field's center (200 pA, 3 second, stimulation radius = 0.05). Seizure territory slowly expanded (the top row, left to right, 10 seconds per frame) with phasic transitions. The 1st frame showed tonic stage, as firing rate within the seizure territory stayed largely constant (the left column, 20 ms per frame).

Clonic phase were shown in the 2nd and 3rd frames. Backward traveling waves (the middle column) emerged. Pretermination phase (the 4th and 5th frames) ensued after wavefront annihilation, with its backward traveling waves shown in the right column. Given the symmetry of the environment, all backward traveling waves met (confluence point) exactly at the field's center.

B) Simulation protocol as Panel A, though spatiotemporally white noise with σ_ξ=20pA was injected uniformly all over the space. The confluence points of backward traveling waves during clonic phase departed from the center (middle column). Multiple, non-symmetric sources generated complex traveling wave patterns during pre-termination phase (right column).

C) Evolution of confluence point positions, quantified from Panel B. The upper row: 6 consecutive confluence points, marked in yellow. Despite complete white noise, confluence point positions did not randomly flip. Instead, all of them appeared at the upper left quadrant. Lower subpanel: positions of all confluence points. During the clonic phase (n=120), confluence points significantly departed away from the center (signed-rank test for both x and y coordinates, p <0.001) and their positions evolved continuously (auto-correlation coefficients: $\rho_x(1)$=0.82, $\rho_y(1)$=0.83; both p < 0.001.).

D) Traveling wave direction estimated from the central area (radius = 0.05). White noise generated a consistent traveling wave direction during clonic phase once the confluence points left the field center. Circular auto-correlation $\rho_\theta(1)$ during ictal phase: 0.97, p<0.001, n=120. However, traveling wave directions became chaotic during pre-termination phase: $\rho_\theta(1)$=0.09, p=0.5, n=65.

Figure 5.11 Increasing traveling wave direction variability as seizure approached termination.
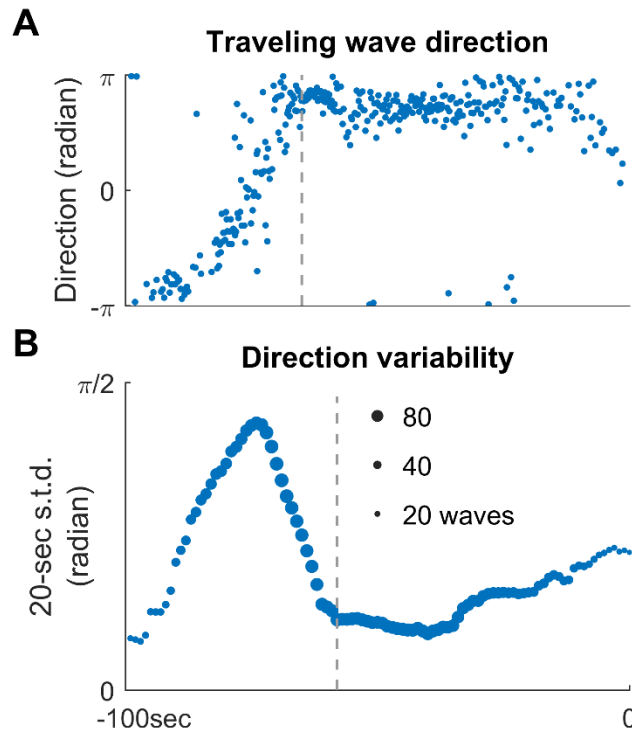
A) All ictal traveling wave direction during the sample seizure recorded from Patient B (the same episode as shown in Figure 5.4). After direct shift (gray dashed line), traveling waves direction was stabilized (backward in comparison to seizure propagation direction).

B) Evolution of traveling direction variability estimated by 20-second moving window every 1 second, quantified by circular standard deviation. Traveling wave direction increased as seizure approached termination. Data right to the gray line: Spearman's correlation coefficient: 0.89, $p < 0.001$.

5.3.8 Spiral wave formation, status epilepticus, and synchronization-induced termination

Without adequate sAHP suppression, the aforementioned seizure termination pathway is compromised in the model, and the territory continues to expand until it occupies the entire neural sheet (Figure 7, in contrast to Figure 6). Spontaneously, at that stage, spiral waves form (Figure 7A), and repel each other (Figure 7C). In this simulation, one spiral center eventually dominated and persisted indefinitely, resulting in in-silico status epilepticus.

Interestingly, there exists an alternative, hidden pathway allowing the model to escape from its everlasting seizure. A global excitatory pulse that temporarily synchronizes the whole neural sheet can break the spiral structure (Figure 7B). Within hundreds of milliseconds, the model directly transitions into post-ictal phase without going through pre-termination dynamics.

Figure 5.12 Emergence of spiral waves, spiral center movement, and synchronization
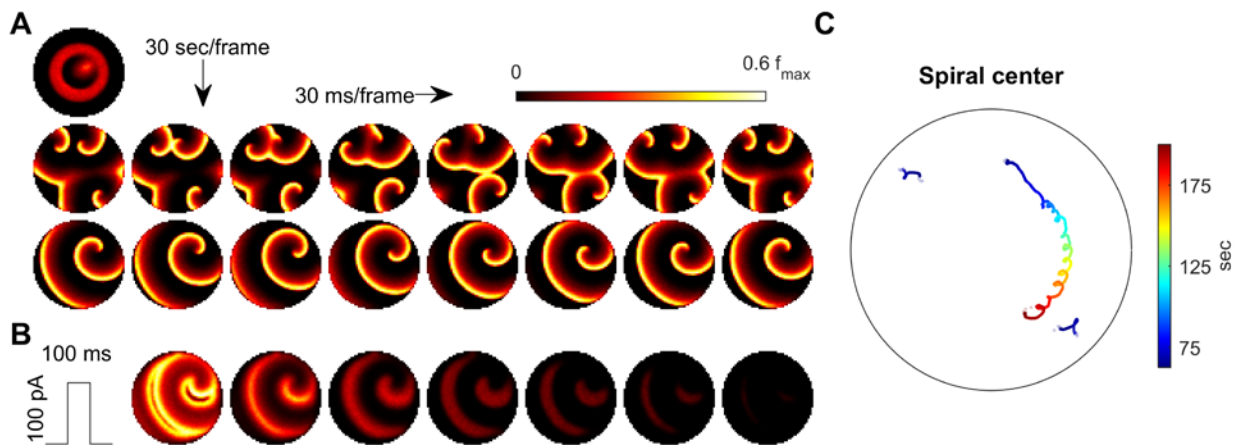
A) Spiral waves emerged after wavefront annihilation in a two-dimensional rate model.

Figure conventions and external ictogenic stimulus were the same as Figure 5.10B. g_K

was decreased to 0.175 nS/Hz to allow full seizure invasion of the whole cortical field. After the ictal wavefront crashed into the boundary, spiral waves developed (the upper row). Three spiral centers co-existed early after wavefront annihilation, though only one survived, as shown in the lower row.

B) A brief synchronizing excitatory pulse (100 ms, 100 pA), given to the whole field (left lower frame of Panel A), successfully destroyed the spiral wave.

C) Movement of spiral wave centers, quantified from Panel A. Time was coded in color, counted from seizure onset. Three spiral waves coexisted at early stage, though two were repelled out of the field. The surviving one patrolled along the boundary, marching with a spiral trajectory. The surviving one would never terminate without further manipulation.

5.4 Discussion

We presented a biophysically constrained computational model of seizures that, despite being limited to a minimal set of localized dynamic neural properties, reproduced several key dynamics of spontaneous human focal seizures that generally manifest on a large scale. We showed that the collapse of inhibition strength ahead of the ictal wavefront, followed by emergence of hyperpolarizing currents, accounts for the slow expansion of seizure territory, tonic-to-clonic transition, and generation of backward traveling waves. The model's dynamics evolve in a way reminiscent of human seizures, displaying both a continuous modulation of ictal activities and distinct ictal stages with characteristic key dynamics. Additionally, the model demonstrates that distinct seizure onset patterns can result from topological variance of recurrent inhibitory projections. The inclusion of STDP in the model results in learned pathological alteration of connectivity, similar to what has been proposed to occur during epileptogenesis (Wong and Crino 2012, Goldberg and Coulter 2013), resulting in seizure threshold reduction and spontaneous seizure generation. We also address failure of seizure termination mechanisms, which can lead to status epilepticus.

Both in vitro brain slice studies (Trevelyan, Sussillo et al. 2007) and in vivo human recordings (Schevon, Weiss et al. 2012) showed that a focal ictal event exerted local excitation and surround inhibition effects, motivating the Mexican-hat pattern of connectivity used in our study. Massive GABAergic activity provoked by ictal events might overwhelm chloride buffering and clearance mechanisms (Lillis, Kramer et al. 2012). The collapsed transmembrane chloride gradient compromises the strength of surround inhibition, leading to successful seizure onset and propagation (Alfonsa, Merricks et al. 2015). Excitatory GABAergic transmissions

160

have been found in epilepsy patient brain slices (Cohen, Navarro et al. 2002). The paradoxical effects may attribute to clearance defects, as tissues from temporal lobe epilepsy (Huberfeld, Wittner et al. 2007) and tumor-associated epilepsy (Pallud, Le Van Quyen et al. 2014) both showed reduced KCC2 expression. Experimentally knocking down KCC2 lead to epileptiform discharges (Zhu, Lovinger et al. 2005), and an in-vitro fluorescence study also showed that chloride accumulation preceded seizure onset (Lillis, Kramer et al. 2012). In agreement with previous studies, our model indicates chloride homeostasis is critical in preventing and restraining focal seizures.

Phasic transitions have been demonstrated in focal seizures (Bergey and Franaszczuk 2001, Schiff, Sauer et al. 2005). In our model, because of sAHP currents, the tonic-firing population could not support such a high firing rate indefinitely. Reduced excitability caused a spontaneous transition into periodic bursting, rippling away from the wavefront. The sequence of chloride overload, followed by excitability reduction, thus explains both the slow-marching wavefront and backward traveling waves. The duration required for the wavefront to recruit the next neuron progressively increases; once it becomes longer than the duration it can stay in tonic-firing, the ictal wavefront is annihilated. During the subsequent pre-termination phase, the return of inhibition strength produces the reduces wave speed and increased inter-discharge interval. The seizure terminates when the ictal core's excitability can no longer support traveling waves. Clinical studies have also confirmed the importance of sAHP in prohibiting epileptic activities, as KCNQ2 and KCNQ3 mutations, which contributed to sAHP, have been reported to cause benign familial neonatal convulsions (Biervert, Schroeder et al. 1998, Singh, Westenskow et al. 2003, Tzingounis and Nicoll 2008).

The biophysical processes proposed here should not be considered the only mechanisms causing seizure evolution. Instead, they should be considered as representative candidates. Processes which share similar effects on network dynamics operating in the same time scale may also contribute, as we showed in our phenomenological model. For example, in addition to chloride overload, depolarization block of GABAergic neurons may also contribute to inhibition breakdown (Meijer, Eissa et al. 2015). Aside from hyperpolarizing currents, intense neuronal bursts have been found to inactivate sodium channels, which reduces neuronal excitability within seconds (Fleidervish, Friedman et al. 1996). Excitatory synaptic depletion (Beverlin, Kakalios et al. 2012) and inhibitory cell recovery (Ziburkus, Cressman et al. 2006) have also been reported to cause tonic-to-clonic transitions and seizure termination. However, in search of physiological processes underlying seizure evolution, universally present mechanisms should be prioritized because the key features of seizure dynamics have been observed across various brain regions.

Spatial distribution of recurrent inhibition might also explain the difference between focal seizure subtypes. LVFA onset, in our model, is associated with emergence of a local activity bump. Whereas, seizures with rhythmic discharging onsets, which are called low-frequency, high-voltage spike onset (Perucca, Dubeau et al. 2014), or hypersynchrnous onset in in the clinical literature (Weiss, Alvarado-Rojas et al. 2016) are associated with forward traveling waves. Inadequate local inhibitory restraint allows ictogenic insults to generate neuronal bursts, rippling out as forward traveling waves producing rhythmic, large amplitude, low-frequency LFP discharges. However, because forward traveling waves operate in areas that inhibition strength is still largely intact, albeit reduced progressively, their speed is slower than backward traveling waves.

162

Focal, highly-recurrently connected neural clusters have been found in focal epilepsy patients by imaging studies (Liao, Zhang et al. 2010, Luo, An et al. 2014). Our model suggests STDP can bias recurrent excitatory projections centripetally, generating centripetal traveling waves and causing spontaneous seizures. This 'hijacked' learning mechanism is compatible with epileptogenic neural clusters, although the altered topology may be both casual and sequential to epileptic activities. Clinical studies have also shown LVFA onsets are associated with herald spikes (Lee, Spencer et al. 2000), which we showed are associated with neurons activated in a centripetal sequence. Our model also predicts that, within a cluster, seizure dynamics should be highly stereotypical. This has also been supported by previous observations that focal seizure evolution followed fixed sequences, especially during early stages (Jouny, Adamolekun et al. 2007).

In our model, some seizures fail to terminate. In these seizures at the point following wavefront annihilation, a spiral wave pattern is established and continues indefinitely. In agreement with our prediction, spiral waves have been shown in animal seizure models. Voltage-sensitive dye has shown that, in rodent visual cortex, both in brain slice model (Huang, Troy et al. 2004) and in vivo (Huang, Xu et al. 2010), spiral waves can develop under bicuculline disinhibition. Multielectrode array recordings have also shown spiral epileptiform discharges happened during feline picrotoxin-induced seizures (Viventi, Kim et al. 2011). We expect spiral wave structures would be found more often as human high-density electrode recording technology advances, particularly during prolonged seizures. Further studies about the stability about seizure spiral centers may be required (Biktashev 2007).

In a two-dimensional space, spiral waves can be terminated by a brief, synchronized excitation. Similar observation that synchronization promotes seizure termination has also been reported in status epilepticus patients (Schindler, Elger et al. 2007). Interestingly, spiral waves also develop during ventricular fibrillation, a fatal form of cardiac arrhythmia (Gray, Pertsov et al. 1998). Delivering a brief DC shock that synchronizes the whole heart at once has been the standard therapy to rescue patients. Our theory suggests similar treatment may abort spiral-wave seizures.

In this study, we aimed to explain key seizure manifestations with few assumptions. However, since every individual patient is unique, it may not be surprising to find counter examples. Nevertheless, instead of trying to replicate a patient's epileptic brain neuron by neuron, we believe our simplistic approach will be more valuable in two ways – provide insights to principles underlying complex seizure dynamics and make predictions that are generalizable.

Conclusion

With minimal assumptions, we developed a computational model that replicates several key manifestations of spontaneous human focal seizure semiology, and the activity of seizing neuronal populations. Additionally, this simple, biophysical model makes several experimentally and clinically verifiable predictions. With rapid advancement of clinical and experimental tools, we believe our computational work provides both a means for mechanistic understanding of seizure physiology, and therefore a basis for developing future therapies.

Bibliography

Huang di nei jing su wen. 9 juan, Zhejiang shu ju.

Alarcon, G., J. J. Garcia Seoane, C. D. Binnie, M. C. Martin Miguel, J. Juler, C. E. Polkey, R. D. Elwes and J. M. Ortiz Blasco (1997). "Origin and propagation of interictal discharges in the acute electrocorticogram. Implications for pathophysiology and surgical treatment of temporal lobe epilepsy." Brain **120 (Pt 12)**: 2259-2282.

Alarcon, G., C. N. Guy, C. D. Binnie, S. R. Walker, R. D. Elwes and C. E. Polkey (1994). "Intracerebral propagation of interictal activity in partial epilepsy: implications for source localisation." J Neurol Neurosurg Psychiatry **57**(4): 435-449.

Albowitz, B. and E. L. Gasteiger (1985). "Interictal afterdischarge in focal penicillin epilepsy: thalamocortical unit activity." Exp Neurol **88**(2): 360-371.

Alfonsa, H., E. M. Merricks, N. K. Codadu, M. O. Cunningham, K. Deisseroth, C. Racca and A. J. Trevelyan (2015). "The contribution of raised intraneuronal chloride to epileptic network activity." J Neurosci **35**(20): 7715-7726.

Alger, B. E. and R. A. Nicoll (1980). "Epileptiform burst afterhyperolarization: calcium-dependent potassium potential in hippocampal CA1 pyramidal cells." Science **210**(4474): 1122-1124.

Alvarado-Rojas, C., M. Valderrama, A. Fouad-Ahmed, H. Feldwisch-Drentrup, M. Ihle, C. A. Teixeira, F. Sales, A. Schulze-Bonhage, C. Adam, A. Dourado, S. Charpier, V. Navarro and M. Le Van Quyen (2014). "Slow modulations of high-frequency activity (40-140-Hz) discriminate preictal changes in human focal epilepsy." Sci Rep **4**: 4545.

Anziska, B. and R. Q. Cracco (1977). "Changes in frequency and amplitude in electrographic seizure discharges." Clinical EEG and Neuroscience **8**(4): 206-210.

Avoli, M., G. Biagini and M. de Curtis (2006). "Do interictal spikes sustain seizures and epileptogenesis?" Epilepsy Curr **6**(6): 203-207.

Avoli, M. and M. de Curtis (2011). "GABAergic synchronization in the limbic system and its role in the generation of epileptiform activity." Prog Neurobiol **95**(2): 104-132.

Avoli, M., M. de Curtis, V. Gnatkovsky, J. Gotman, R. Kohling, M. Levesque, F. Manseau, Z. Shiri and S. Williams (2016). "Specific imbalance of excitatory/inhibitory signaling establishes seizure onset pattern in temporal lobe epilepsy." J Neurophysiol **115**(6): 3229-3237.

Badier, J. M. and P. Chauvel (1995). "Spatio-temporal characteristics of paroxysmal interictal events in human temporal lobe epilepsy." J Physiol Paris **89**(4-6): 255-264.

Bahar, S., M. Suh, M. Zhao and T. H. Schwartz (2006). "Intrinsic optical signal imaging of neocortical seizures: the 'epileptic dip'." Neuroreport **17**(5): 499-503.

Banerjee, P. N., D. Filippi and W. Allen Hauser (2009). "The descriptive epidemiology of epilepsy-a review." Epilepsy Res **85**(1): 31-45.

Barmashenko, G., S. Hefft, A. Aertsen, T. Kirschstein and R. Kohling (2011). "Positive shifts of the GABAA receptor reversal potential due to altered chloride homeostasis is widespread after status epilepticus." Epilepsia **52**(9): 1570-1578.

Baumgartner, C., G. Lindinger, A. Ebner, S. Aull, W. Serles, A. Olbrich, S. Lurger, T. Czech, R. Burgess and H. Luders (1995). "Propagation of interictal epileptic activity in temporal lobe epilepsy." Neurology **45**(1): 118-122.

Bautista, R. E., M. A. Cobbs, D. D. Spencer and S. S. Spencer (1999). "Prediction of surgical outcome by interictal epileptiform abnormalities during intracranial EEG monitoring in patients with extrahippocampal seizures." Epilepsia **40**(7): 880-890.

Bayly, P. V., B. H. KenKnight, J. M. Rogers, R. E. Hillsley, R. E. Ideker and W. M. Smith (1998). "Estimation of conduction velocity vector fields from epicardial mapping data." IEEE Trans Biomed Eng **45**(5): 563-571.

Berg, A. T. (2009). "Identification of pharmacoresistant epilepsy." Neurol Clin **27**(4): 1003-1013.

Bergey, G. K. and P. J. Franaszczuk (2001). "Epileptic seizures are characterized by changing signal complexity." Clin Neurophysiol **112**(2): 241-249.

Beverlin, B., 2nd, J. Kakalios, D. Nykamp and T. I. Netoff (2012). "Dynamical changes in neurons during seizures determine tonic to clonic shift." J Comput Neurosci **33**(1): 41-51.

Bi, G. Q. and M. M. Poo (1998). "Synaptic modifications in cultured hippocampal neurons: dependence on spike timing, synaptic strength, and postsynaptic cell type." J Neurosci **18**(24): 10464-10472.

Biervert, C., B. C. Schroeder, C. Kubisch, S. F. Berkovic, P. Propping, T. J. Jentsch and O. K. Steinlein (1998). "A potassium channel mutation in neonatal human epilepsy." Science **279**(5349): 403-406.

Bikson, M., J. E. Fox and J. G. Jefferys (2003). "Neuronal aggregate formation underlies spatiotemporal dynamics of nonsynaptic seizure initiation." J Neurophysiol **89**(4): 2330-2333.

Biktashev, V. N. (2007). "Drift of spiral waves." Scholarpedia **2**(4): 1836.

Blumenfeld, H. (2002). "The thalamus and seizures." Arch Neurol **59**(1): 135-137.

Blumenfeld, H., M. Rivera, K. A. McNally, K. Davis, D. D. Spencer and S. S. Spencer (2004). "Ictal neocortical slowing in temporal lobe epilepsy." Neurology **63**(6): 1015-1021.

Bokil, H., P. Andrews, J. E. Kulkarni, S. Mehta and P. P. Mitra (2010). "Chronux: a platform for analyzing neural signals." J Neurosci Methods **192**(1): 146-151.

Braitenberg, V. and A. Schüz (2013). Cortex: statistics and geometry of neuronal connectivity, Springer Science & Business Media.

Brown, E. N., R. E. Kass and P. P. Mitra (2004). "Multiple neural spike train data analysis: state-of-the-art and future challenges." Nat Neurosci **7**(5): 456-461.

Buchin, A., A. Chizhov, G. Huberfeld, R. Miles and B. S. Gutkin (2016). "Reduced Efficacy of the KCC2 Cotransporter Promotes Epileptic Oscillations in a Subiculum Network Model." J Neurosci **36**(46): 11619-11633.

Buzsaki, G., C. A. Anastassiou and C. Koch (2012). "The origin of extracellular fields and currents--EEG, ECoG, LFP and spikes." Nat Rev Neurosci **13**(6): 407-420.

Cammarota, M., G. Losi, A. Chiavegato, M. Zonta and G. Carmignoto (2013). "Fast spiking interneuron control of seizure propagation in a cortical slice model of focal epilepsy." J Physiol **591**(4): 807-822.

Chagnac-Amitai, Y. and B. W. Connors (1989). "Horizontal spread of synchronized activity in neocortex and its control by GABA-mediated inhibition." J Neurophysiol **61**(4): 747-758.

Chalifoux, J. R. and A. G. Carter (2011). "GABAB receptor modulation of synaptic function." Curr Opin Neurobiol **21**(2): 339-344.

Chauviere, L., T. Doublet, A. Ghestem, S. S. Siyoucef, F. Wendling, R. Huys, V. Jirsa, F. Bartolomei and C. Bernard (2012). "Changes in interictal spike features precede the onset of temporal lobe epilepsy." Ann Neurol **71**(6): 805-814.

Chen, T. W., T. J. Wardill, Y. Sun, S. R. Pulver, S. L. Renninger, A. Baohan, E. R. Schreiter, R. A. Kerr, M. B. Orger, V. Jayaraman, L. L. Looger, K. Svoboda and D. S. Kim (2013). "Ultrasensitive fluorescent proteins for imaging neuronal activity." Nature **499**(7458): 295-300.

Chervin, R. D., P. A. Pierce and B. W. Connors (1988). "Periodicity and directionality in the propagation of epileptiform discharges across neocortex." J Neurophysiol **60**(5): 1695-1713.

Cohen, I., V. Navarro, S. Clemenceau, M. Baulac and R. Miles (2002). "On the origin of interictal activity in human temporal lobe epilepsy in vitro." Science **298**(5597): 1418-1421.

Colder, B. W., R. C. Frysinger, C. L. Wilson, R. M. Harper and J. Engel, Jr. (1996). "Decreased neuronal burst discharge near site of seizure onset in epileptic human temporal lobes." <u>Epilepsia</u> **37**(2): 113-121.

Colder, B. W., C. L. Wilson, R. C. Frysinger, L. C. Chao, R. M. Harper and J. Engel, Jr. (1996). "Neuronal synchrony in relation to burst discharge in epileptic human temporal lobes." <u>J Neurophysiol</u> **75**(6): 2496-2508.

Constable, R. T., D. Scheinost, E. S. Finn, X. Shen, M. Hampson, F. S. Winstanley, D. D. Spencer and X. Papademetris (2013). "Potential use and challenges of functional connectivity mapping in intractable epilepsy." <u>Front Neurol</u> **4**: 39.

Cressman, J. R., Jr., G. Ullah, J. Ziburkus, S. J. Schiff and E. Barreto (2009). "The influence of sodium and potassium dynamics on excitability, seizures, and the stability of persistent states: I. Single neuron dynamics." <u>J Comput Neurosci</u> **26**(2): 159-170.

Daube, J. R., D. I. Rubin and ebrary Inc. (2009). Clinical neurophysiology. <u>Contemporary neurology series 75</u>. Oxford ; New York, Oxford University Press,**:** xxvii, 886 p., 887 p. of plates.

David, O., J. Bastin, S. Chabardes, L. Minotti and P. Kahane (2010). "Studying network mechanisms using intracranial stimulation in epileptic patients." <u>Front Syst Neurosci</u> **4**: 148.

de Curtis, M. and G. Avanzini (2001). "Interictal spikes in focal epileptogenesis." <u>Prog Neurobiol</u> **63**(5): 541-567.

de Curtis, M. and M. Avoli (2016). "GABAergic networks jump-start focal seizures." <u>Epilepsia</u>.

de Curtis, M., J. G. R. Jefferys and M. Avoli (2012). Interictal Epileptiform Discharges in Partial Epilepsy: Complex Neurobiological Mechanisms Based on Experimental and Clinical Evidence. <u>Jasper's Basic Mechanisms of the Epilepsies</u>. J. L. Noebels, M. Avoli, M. A. Rogawski, R. W. Olsen and A. V. Delgado-Escueta. Bethesda (MD).

Deisz, R. A., T. N. Lehmann, P. Horn, C. Dehnicke and R. Nitsch (2011). "Components of neuronal chloride transport in rat and human neocortex." <u>J Physiol</u> **589**(Pt 6): 1317-1347.

Detre, J. A., D. C. Alsop, G. K. Aguirre and M. R. Sperling (1996). "Coupling of cortical and thalamic ictal activity in human partial epilepsy: demonstration by functional magnetic resonance imaging." <u>Epilepsia</u> **37**(7): 657-661.

Devinsky, O. (2004). "Diagnosis and treatment of temporal lobe epilepsy." <u>Rev Neurol Dis</u> **1**(1): 2-9.

Dyhrfjeld-Johnsen, J., V. Santhakumar, R. J. Morgan, R. Huerta, L. Tsimring and I. Soltesz (2007). "Topological determinants of epileptogenesis in large-scale structural and functional models of the dentate gyrus derived from experimental data." <u>J Neurophysiol</u> **97**(2): 1566-1587.

Ebersole, J. S. (1994). "Non-invasive localization of the epileptogenic focus by EEG dipole modeling." Acta Neurol Scand Suppl **152**: 20-28.

Ebersole, J. S. (1997). "Defining epileptogenic foci: past, present, future." J Clin Neurophysiol **14**(6): 470-483.

Ebersole, J. S. (2000). "Noninvasive localization of epileptogenic foci by EEG source modeling." Epilepsia **41 Suppl 3**: S24-33.

Ebersole, J. S. and T. A. Pedley (2003). Current practice of clinical electroencephalography. Philadelphia, Lippincott Williams & Wilkins,.

Ebersole, J. S. and P. B. Wade (1991). "Spike voltage topography identifies two types of frontotemporal epileptic foci." Neurology **41**(9): 1425-1433.

Einevoll, G. T., C. Kayser, N. K. Logothetis and S. Panzeri (2013). "Modelling and analysis of local field potentials for studying the function of cortical circuits." Nat Rev Neurosci **14**(11): 770-785.

Eissa, T. L., A. K. Tryba, C. J. Marcuccilli, F. Ben-Mabrouk, E. H. Smith, S. M. Lew, R. R. Goodman, G. M. McKhann, Jr., D. M. Frim, L. L. Pesce, M. H. Kohrman, R. G. Emerson, C. A. Schevon and W. van Drongelen (2016). "Multiscale Aspects of Generation of High-Gamma Activity during Seizures in Human Neocortex." eNeuro **3**(2).

Emerson, R. G., C. A. Turner, T. A. Pedley, T. S. Walczak and M. Forgione (1995). "Propagation patterns of temporal spikes." Electroencephalogr Clin Neurophysiol **94**(5): 338-348.

Englot, D. J., B. Modi, A. M. Mishra, M. DeSalvo, F. Hyder and H. Blumenfeld (2009). "Cortical deactivation induced by subcortical network dysfunction in limbic seizures." J Neurosci **29**(41): 13006-13018.

Esteller, R., J. Echauz, T. Tcheng, B. Litt and B. Pless (2001). "Line length: An efficient feature for seizure onset detection." Proceedings of the 23rd Annual International Conference of the Ieee Engineering in Medicine and Biology Society, Vols 1-4 **23**: 1707-1710.

Extercatte, J., G. J. de Haan and A. Gaitatzis (2015). "Teaching Video NeuroImages: Frontal opercular seizures with jacksonian march." Neurology **84**(11): e83-84.

Faeth, W. H., A. E. Walker and O. J. Andy (1954). "The propagation of cortical and subcortical epileptic discharge." Epilepsia **3**: 37-48.

Fahoum, F., R. Lopes, F. Pittau, F. Dubeau and J. Gotman (2012). "Widespread epileptic networks in focal epilepsies: EEG-fMRI study." Epilepsia **53**(9): 1618-1627.

Feldt Muldoon, S., I. Soltesz and R. Cossart (2013). "Spatially clustered neuronal assemblies comprise the microstructure of synchrony in chronically epileptic networks." Proc Natl Acad Sci U S A **110**(9): 3567-3572.

Fisher, R. S., C. Acevedo, A. Arzimanoglou, A. Bogacz, J. H. Cross, C. E. Elger, J. Engel, Jr., L. Forsgren, J. A. French, M. Glynn, D. C. Hesdorffer, B. I. Lee, G. W. Mathern, S. L. Moshe, E. Perucca, I. E. Scheffer, T. Tomson, M. Watanabe and S. Wiebe (2014). "ILAE official report: a practical clinical definition of epilepsy." Epilepsia **55**(4): 475-482.

Fisher, R. S., J. H. Cross, J. A. French, N. Higurashi, E. Hirsch, F. E. Jansen, L. Lagae, S. L. Moshe, J. Peltola, E. Roulet Perez, I. E. Scheffer and S. M. Zuberi (2017). "Operational classification of seizure types by the International League Against Epilepsy: Position Paper of the ILAE Commission for Classification and Terminology." Epilepsia **58**(4): 522-530.

Fisher, R. S., H. E. Scharfman and M. deCurtis (2014). "How can we identify ictal and interictal abnormal activity?" Adv Exp Med Biol **813**: 3-23.

Fleidervish, I. A., A. Friedman and M. J. Gutnick (1996). "Slow inactivation of Na+ current and slow cumulative spike adaptation in mouse and guinea-pig neocortical neurones in slices." J Physiol **493 (Pt 1)**: 83-97.

Frohlich, F., M. Bazhenov, V. Iragui-Madoz and T. J. Sejnowski (2008). "Potassium dynamics in the epileptic cortex: new insights on an old topic." Neuroscientist **14**(5): 422-433.

Frohlich, F., T. J. Sejnowski and M. Bazhenov (2010). "Network bistability mediates spontaneous transitions between normal and pathological brain states." J Neurosci **30**(32): 10734-10743.

Gallmetzer, P., F. Leutmezer, W. Serles, E. Assem-Hilger, J. Spatt and C. Baumgartner (2004). "Postictal paresis in focal epilepsies--incidence, duration, and causes: a video-EEG monitoring study." Neurology **62**(12): 2160-2164.

Gasteiger, E. L., B. Albowitz and F. M. Barken (1985). "Interictal afterdischarge in focal penicillin epilepsy: block by thalamic cooling." Exp Neurol **88**(2): 349-359.

Geneslaw, A. S., M. Zhao, H. Ma and T. H. Schwartz (2011). "Tissue hypoxia correlates with intensity of interictal spikes." J Cereb Blood Flow Metab **31**(6): 1394-1402.

Goldberg, E. M. and D. A. Coulter (2013). "Mechanisms of epileptogenesis: a convergence on neural circuit dysfunction." Nat Rev Neurosci **14**(5): 337-349.

Goldensohn, E. S. and A. M. Salazar (1986). "Temporal and spatial distribution of intracellular potentials during generation and spread of epileptogenic discharges." Adv Neurol **44**: 559-582.

Golomb, D. and Y. Amitai (1997). "Propagating neuronal discharges in neocortical slices: computational and experimental study." J Neurophysiol **78**(3): 1199-1211.

Goncharova, II, R. Alkawadri, N. Gaspard, R. B. Duckrow, D. D. Spencer, L. J. Hirsch, S. S. Spencer and H. P. Zaveri (2016). "The relationship between seizures, interictal spikes and antiepileptic drugs." Clin Neurophysiol **127**(9): 3180-3186.

Gonzalez-Ramirez, L. R., O. J. Ahmed, S. S. Cash, C. E. Wayne and M. A. Kramer (2015). "A biologically constrained, mathematical model of cortical wave propagation preceding seizure termination." PLoS Comput Biol **11**(2): e1004065.

Gotman, J. (1983). "Measurement of small time differences between EEG channels: method and application to epileptic seizure propagation." Electroencephalogr Clin Neurophysiol **56**(5): 501-514.

Gotman, J. and M. G. Marciani (1985). "Electroencephalographic spiking activity, drug levels, and seizure occurrence in epileptic patients." Ann Neurol **17**(6): 597-603.

Gray, R. A., A. M. Pertsov and J. Jalife (1998). "Spatial and temporal organization during cardiac fibrillation." Nature **392**(6671): 75-78.

Guo, L., D. Rivero, J. Dorado, J. R. Rabunal and A. Pazos (2010). "Automatic epileptic seizure detection in EEGs based on line length feature and artificial neural networks." J Neurosci Methods **191**(1): 101-109.

Gutnick, M. J. and D. A. Prince (1972). "Thalamocortical relay neurons: antidromic invasion of spikes from a cortical epileptogenic focus." Science **176**(4033): 424-426.

Hamer, H. M., I. Najm, A. Mohamed and E. Wyllie (1999). "Interictal epileptiform discharges in temporal lobe epilepsy due to hippocampal sclerosis versus medial temporal lobe tumors." Epilepsia **40**(9): 1261-1268.

Heck, C. N., D. King-Stephens, A. D. Massey, D. R. Nair, B. C. Jobst, G. L. Barkley, V. Salanova, A. J. Cole, M. C. Smith, R. P. Gwinn, C. Skidmore, P. C. Van Ness, G. K. Bergey, Y. D. Park, I. Miller, E. Geller, P. A. Rutecki, R. Zimmerman, D. C. Spencer, A. Goldman, J. C. Edwards, J. W. Leiphart, R. E. Wharen, J. Fessler, N. B. Fountain, G. A. Worrell, R. E. Gross, S. Eisenschenk, R. B. Duckrow, L. J. Hirsch, C. Bazil, C. A. O'Donovan, F. T. Sun, T. A. Courtney, C. G. Seale and M. J. Morrell (2014). "Two-year seizure reduction in adults with medically intractable partial onset epilepsy treated with responsive neurostimulation: final results of the RNS System Pivotal trial." Epilepsia **55**(3): 432-441.

Hesdorffer, D. C., T. Tomson, E. Benn, J. W. Sander, L. Nilsson, Y. Langan, T. S. Walczak, E. Beghi, M. J. Brodie, W. A. Hauser and I. C. o. Epidemiology (2012). "Do antiepileptic drugs or generalized tonic-clonic seizure frequency increase SUDEP risk? A combined analysis." Epilepsia **53**(2): 249-252.

Hofer, S. B., H. Ko, B. Pichler, J. Vogelstein, H. Ros, H. Zeng, E. Lein, N. A. Lesica and T. D. Mrsic-Flogel (2011). "Differential connectivity and response dynamics of excitatory and inhibitory neurons in visual cortex." Nat Neurosci **14**(8): 1045-1052.

Holland, P. W. and R. E. Welsch (1977). "Robust regression using iteratively reweighted least-squares." Communications in Statistics-theory and Methods **6**(9): 813-827.

Hsu, D., W. Chen, M. Hsu and J. M. Beggs (2008). "An open hypothesis: is epilepsy learned, and can it be unlearned?" Epilepsy Behav **13**(3): 511-522.

Huang, X., W. C. Troy, Q. Yang, H. Ma, C. R. Laing, S. J. Schiff and J. Y. Wu (2004). "Spiral waves in disinhibited mammalian neocortex." J Neurosci **24**(44): 9897-9902.

Huang, X., W. Xu, J. Liang, K. Takagaki, X. Gao and J. Y. Wu (2010). "Spiral wave dynamics in neocortex." Neuron **68**(5): 978-990.

Huberfeld, G., L. Wittner, S. Clemenceau, M. Baulac, K. Kaila, R. Miles and C. Rivera (2007). "Perturbed chloride homeostasis and GABAergic signaling in human temporal lobe epilepsy." J Neurosci **27**(37): 9866-9873.

Huneau, C., P. Benquet, G. Dieuset, A. Biraben, B. Martin and F. Wendling (2013). "Shape features of epileptic spikes are a marker of epileptogenesis in mice." Epilepsia **54**(12): 2219-2227.

Hutchins, L. N., S. M. Murphy, P. Singh and J. H. Graber (2008). "Position-dependent motif characterization using non-negative matrix factorization." Bioinformatics **24**(23): 2684-2690.

Isokawa, M. (2000). "Remodeling dendritic spines of dentate granule cells in temporal lobe epilepsy patients and the rat pilocarpine model." Epilepsia **41 Suppl 6**: S14-17.

Iyer, A. N. and R. A. Gray (2001). "An experimentalist's approach to accurate localization of phase singularities during reentry." Ann Biomed Eng **29**(1): 47-59.

Jensen, M. S. and Y. Yaari (1988). "The relationship between interictal and ictal paroxysms in an in vitro model of focal hippocampal epilepsy." Ann Neurol **24**(5): 591-598.

Jirsa, V. K., W. C. Stacey, P. P. Quilichini, A. I. Ivanov and C. Bernard (2014). "On the nature of seizure dynamics." Brain **137**(Pt 8): 2210-2230.

Jiruska, P., M. de Curtis, J. G. Jefferys, C. A. Schevon, S. J. Schiff and K. Schindler (2013). "Synchronization and desynchronization in epilepsy: controversies and hypotheses." J Physiol **591**(Pt 4): 787-797.

Jones, M. V. and G. L. Westbrook (1996). "The impact of receptor desensitization on fast synaptic transmission." <u>Trends Neurosci</u> **19**(3): 96-101.

Jouny, C. C., B. Adamolekun, P. J. Franaszczuk and G. K. Bergey (2007). "Intrinsic ictal dynamics at the seizure focus: effects of secondary generalization revealed by complexity measures." <u>Epilepsia</u> **48**(2): 297-304.

Kalman, R. E. (1960). "A new approach to linear filtering and prediction problems." <u>Journal of basic Engineering</u> **82**(1): 35-45.

Karoly, P. J., D. R. Freestone, R. Boston, D. B. Grayden, D. Himes, K. Leyde, U. Seneviratne, S. Berkovic, T. O'Brien and M. J. Cook (2016). "Interictal spikes and epileptic seizures: their relationship and underlying rhythmicity." <u>Brain</u> **139**(Pt 4): 1066-1078.

Kay, M. W. and R. A. Gray (2005). "Measuring curvature and velocity vector fields for waves of cardiac excitation in 2-D media." <u>IEEE Trans Biomed Eng</u> **52**(1): 50-63.

Keller, C. J., W. Truccolo, J. T. Gale, E. Eskandar, T. Thesen, C. Carlson, O. Devinsky, R. Kuzniecky, W. K. Doyle, J. R. Madsen, D. L. Schomer, A. D. Mehta, E. N. Brown, L. R. Hochberg, I. Ulbert, E. Halgren and S. S. Cash (2010). "Heterogeneous neuronal firing patterns during interictal epileptiform discharges in the human cortex." <u>Brain</u> **133**(Pt 6): 1668-1681.

Kepecs, A. and G. Fishell (2014). "Interneuron cell types are fit to function." <u>Nature</u> **505**(7483): 318-326.

Khambhati, A. N., K. A. Davis, T. H. Lucas, B. Litt and D. S. Bassett (2016). "Virtual Cortical Resection Reveals Push-Pull Network Control Preceding Seizure Evolution." <u>Neuron</u> **91**(5): 1170-1182.

Khoo, H. M., Y. Hao, N. von Ellenrieder, N. Zazubovits, J. Hall, A. Olivier, F. Dubeau and J. Gotman (2017). "The hemodynamic response to interictal epileptic discharges localizes the seizure-onset zone." <u>Epilepsia</u>.

Kramer, M. A. and S. S. Cash (2012). "Epilepsy as a disorder of cortical network organization." <u>Neuroscientist</u> **18**(4): 360-372.

Kramer, M. A., U. T. Eden, E. D. Kolaczyk, R. Zepeda, E. N. Eskandar and S. S. Cash (2010). "Coalescence and fragmentation of cortical networks during focal seizures." <u>J Neurosci</u> **30**(30): 10076-10085.

Kramer, M. A., H. E. Kirsch and A. J. Szeri (2005). "Pathological pattern formation and cortical propagation of epileptic seizures." <u>J R Soc Interface</u> **2**(2): 113-127.

Kramer, M. A., E. D. Kolaczyk and H. E. Kirsch (2008). "Emergent network topology at seizure onset in humans." <u>Epilepsy Res</u> **79**(2-3): 173-186.

Kramer, M. A., A. J. Szeri, J. W. Sleigh and H. E. Kirsch (2007). "Mechanisms of seizure propagation in a cortical model." J Comput Neurosci **22**(1): 63-80.

Kramer, M. A., W. Truccolo, U. T. Eden, K. Q. Lepage, L. R. Hochberg, E. N. Eskandar, J. R. Madsen, J. W. Lee, A. Maheshwari, E. Halgren, C. J. Chu and S. S. Cash (2012). "Human seizures self-terminate across spatial scales via a critical transition." Proc Natl Acad Sci U S A **109**(51): 21116-21121.

Krishna, V., N. K. King, F. Sammartino, I. Strauss, D. M. Andrade, R. A. Wennberg and A. M. Lozano (2016). "Anterior Nucleus Deep Brain Stimulation for Refractory Epilepsy: Insights Into Patterns of Seizure Control and Efficacious Target." Neurosurgery **78**(6): 802-811.

Krishnan, G. P. and M. Bazhenov (2011). "Ionic dynamics mediate spontaneous termination of seizures and postictal depression state." J Neurosci **31**(24): 8870-8882.

Kudela, P., P. J. Franaszczuk and G. K. Bergey (2003). "Reduction of intracellular calcium removal rate can explain changes in seizure dynamics: studies in neuronal network models." Epilepsy Res **57**(2-3): 95-109.

Kusske, J. A. (1976). "Interactions between thalamus and cortex in experimental epilepsy in the cat." Exp Neurol **50**(3): 568-578.

Kutner, M. H., C. Nachtsheim and J. Neter (2004). Applied linear regression models. Boston ; New York, McGraw-Hill/Irwin.

Lamberts, R. J., A. Gaitatzis, J. W. Sander, C. E. Elger, R. Surges and R. D. Thijs (2013). "Postictal generalized EEG suppression: an inconsistent finding in people with multiple seizures." Neurology **81**(14): 1252-1256.

Laufs, H. (2012). "Functional imaging of seizures and epilepsy: evolution from zones to networks." Curr Opin Neurol **25**(2): 194-200.

Lee, D. D. and H. S. Seung (1999). "Learning the parts of objects by non-negative matrix factorization." Nature **401**(6755): 788-791.

Lee, S. A., D. D. Spencer and S. S. Spencer (2000). "Intracranial EEG seizure-onset patterns in neocortical epilepsy." Epilepsia **41**(3): 297-307.

Lehnertz, K., S. Bialonski, M. T. Horstmann, D. Krug, A. Rothkegel, M. Staniek and T. Wagner (2009). "Synchronization phenomena in human epileptic brain networks." J Neurosci Methods **183**(1): 42-48.

Liao, W., Z. Zhang, Z. Pan, D. Mantini, J. Ding, X. Duan, C. Luo, G. Lu and H. Chen (2010). "Altered functional connectivity and small-world in mesial temporal lobe epilepsy." PLoS One **5**(1): e8525.

Liley, D. T., P. J. Cadusch and M. P. Dafilis (2002). "A spatially continuous mean field theory of electrocortical activity." Network **13**(1): 67-113.

Lillis, K. P., M. A. Kramer, J. Mertz, K. J. Staley and J. A. White (2012). "Pyramidal cells accumulate chloride at seizure onset." Neurobiol Dis **47**(3): 358-366.

Liou, J. Y., E. Smith, L. Bateman, G. McKhann, R. Goodman, B. Greger, T. Davis, S. Kellis, P. House and C. Schevon (2017). "Multivariate regression methods for estimating velocity of ictal discharges from human microelectrode recordings." J Neural Eng.

Lopantsev, V. and M. Avoli (1998). "Participation of GABAA-mediated inhibition in ictallike discharges in the rat entorhinal cortex." J Neurophysiol **79**(1): 352-360.

Luders, H. O., I. Najm, D. Nair, P. Widdess-Walsh and W. Bingman (2006). "The epileptogenic zone: general principles." Epileptic Disord **8 Suppl 2**: S1-9.

Luo, C., D. An, D. Yao and J. Gotman (2014). "Patient-specific connectivity pattern of epileptic network in frontal lobe epilepsy." Neuroimage Clin **4**: 668-675.

Ma, H., M. Zhao, S. Harris and T. H. Schwartz (2014). Simultaneous multi-wavelength optical imaging of neuronal and hemodynamic activity. Neurovascular Coupling Methods**:** 237-249.

Ma, H., M. Zhao and T. H. Schwartz (2013). "Dynamic neurovascular coupling and uncoupling during ictal onset, propagation, and termination revealed by simultaneous in vivo optical imaging of neural activity and local blood volume." Cereb Cortex **23**(4): 885-899.

Ma, H., M. Zhao, M. Suh and T. H. Schwartz (2009). "Hemodynamic surrogates for excitatory membrane potential change during interictal epileptiform events in rat neocortex." J Neurophysiol **101**(5): 2550-2562.

Ma, H. T., C. H. Wu and J. Y. Wu (2004). "Initiation of spontaneous epileptiform events in the rat neocortex in vivo." J Neurophysiol **91**(2): 934-945.

Magiorkinis, E., K. Sidiropoulou and A. Diamantis (2010). "Hallmarks in the history of epilepsy: epilepsy in antiquity." Epilepsy Behav **17**(1): 103-108.

Manning, J. R., J. Jacobs, I. Fried and M. J. Kahana (2009). "Broadband shifts in local field potential power spectra are correlated with single-neuron spiking in humans." J Neurosci **29**(43): 13613-13620.

Marchetti, C., J. Tabak, N. Chub, M. J. O'Donovan and J. Rinzel (2005). "Modeling spontaneous activity in the developing spinal cord using activity-dependent variations of intracellular chloride." J Neurosci **25**(14): 3601-3612.

Markram, H., M. Toledo-Rodriguez, Y. Wang, A. Gupta, G. Silberberg and C. Wu (2004). "Interneurons of the neocortical inhibitory system." Nat Rev Neurosci **5**(10): 793-807.

Marshall, J. D., J. Z. Li, Y. Zhang, Y. Gong, F. St-Pierre, M. Z. Lin and M. J. Schnitzer (2016). "Cell-Type-Specific Optical Recording of Membrane Voltage Dynamics in Freely Moving Mice." Cell **167**(6): 1650-1662 e1615.

Martin Miguel Mdel, C., J. J. Garcia Seoane, A. Valentin, E. Hughes, R. P. Selway, C. E. Polkey and G. Alarcon (2011). "EEG latency analysis for hemispheric lateralisation in Landau-Kleffner syndrome." Clin Neurophysiol **122**(2): 244-252.

Martinet, L. E., G. Fiddyment, J. R. Madsen, E. N. Eskandar, W. Truccolo, U. T. Eden, S. S. Cash and M. A. Kramer (2017). "Human seizures couple across spatial scales through travelling wave dynamics." Nat Commun **8**: 14896.

Matsumoto, H. and C. A. Marsan (1964). "Cortical Cellular Phenomena in Experimental Epilepsy: Interictal Manifestations." Exp Neurol **9**: 286-304.

Mattson, R. H., J. A. Cramer, J. F. Collins, D. B. Smith, A. V. Delgado-Escueta, T. R. Browne, P. D. Williamson, D. M. Treiman, J. O. McNamara, C. B. McCutchen and et al. (1985). "Comparison of carbamazepine, phenobarbital, phenytoin, and primidone in partial and secondarily generalized tonic-clonic seizures." N Engl J Med **313**(3): 145-151.

Mazeh, N., D. E. Haines, M. W. Kay and B. J. Roth (2013). "A Simplified Approach for Simultaneous Measurements of Wavefront Velocity and Curvature in the Heart Using Activation Times." Cardiovasc Eng Technol **4**(4): 520-534.

Mazzoni, A., H. Linden, H. Cuntz, A. Lansner, S. Panzeri and G. T. Einevoll (2015). "Computing the Local Field Potential (LFP) from Integrate-and-Fire Network Models." PLoS Comput Biol **11**(12): e1004584.

Mehta, M. R., C. Dasgupta and G. R. Ullal (1993). "A neural network model for kindling of focal epilepsy: basic mechanism." Biol Cybern **68**(4): 335-340.

Meijer, H. G., T. L. Eissa, B. Kiewiet, J. F. Neuman, C. A. Schevon, R. G. Emerson, R. R. Goodman, G. M. McKhann, Jr., C. J. Marcuccilli, A. K. Tryba, J. D. Cowan, S. A. van Gils and W. van Drongelen (2015). "Modeling focal epileptic activity in the Wilson-cowan model with depolarization block." J Math Neurosci **5**: 7.

Merricks, E. M., E. H. Smith, G. M. McKhann, R. R. Goodman, L. M. Bateman, R. G. Emerson, C. A. Schevon and A. J. Trevelyan (2015). "Single unit action potentials in humans and the effect of seizure activity." Brain **138**(Pt 10): 2891-2906.

Mizuno-Matsumoto, Y., K. Okazaki, A. Kato, T. Yoshimine, Y. Sato, S. Tamura and T. Hayakawa (1999). "Visualization of epileptogenic phenomena using cross-correlation analysis: localization of epileptic foci and propagation of epileptiform discharges." IEEE Trans Biomed Eng **46**(3): 271-279.

Mondragon, S. and M. Lamarche (1990). "Suppression of motor seizures after specific thalamotomy in chronic epileptic monkeys." Epilepsy Res **5**(2): 137-145.

Motelow, J. E., W. Li, Q. Zhan, A. M. Mishra, R. N. Sachdev, G. Liu, A. Gummadavelli, Z. Zayyad, H. S. Lee, V. Chu, J. P. Andrews, D. J. Englot, P. Herman, B. G. Sanganahalli, F. Hyder and H. Blumenfeld (2015). "Decreased subcortical cholinergic arousal in focal seizures." Neuron **85**(3): 561-572.

Muldoon, S. F., V. Villette, T. Tressard, A. Malvache, S. Reichinnek, F. Bartolomei and R. Cossart (2015). "GABAergic inhibition shapes interictal dynamics in awake epileptic mice." Brain **138**(Pt 10): 2875-2890.

Mylvaganam, S., M. Ramani, M. Krawczyk and P. L. Carlen (2014). "Roles of gap junctions, connexins, and pannexins in epilepsy." Front Physiol **5**: 172.

Nariai, H., T. Nagasawa, C. Juhasz, S. Sood, H. T. Chugani and E. Asano (2011). "Statistical mapping of ictal high-frequency oscillations in epileptic spasms." Epilepsia **52**(1): 63-74.

Naze, S., C. Bernard and V. Jirsa (2015). "Computational modeling of seizure dynamics using coupled neuronal networks: factors shaping epileptiform activity." PLoS Comput Biol **11**(5): e1004209.

Neckelmann, D., F. Amzica and M. Steriade (2000). "Changes in neuronal conductance during different components of cortically generated spike-wave seizures." Neuroscience **96**(3): 475-485.

Ni, M. (1995). The Yellow Emperor's classic of medicine: a new translation of the Neijing Suwen with commentary, Shambhala Publications.

Niedermeyer, E. and F. H. Lopes da Silva (1982). Electroencephalography, basic principles, clinical applications, and related fields. Baltimore, Urban & Schwarzenberg.

Noachtar, S. and J. Remi (2009). "The role of EEG in epilepsy: a critical review." Epilepsy Behav **15**(1): 22-33.

Pallud, J., M. Le Van Quyen, F. Bielle, C. Pellegrino, P. Varlet, M. Labussiere, N. Cresto, M. J. Dieme, M. Baulac, C. Duyckaerts, N. Kourdougli, G. Chazal, B. Devaux, C. Rivera, R. Miles, L. Capelle and G. Huberfeld (2014). "Cortical GABAergic excitation contributes to epileptic activities around human glioma." Sci Transl Med **6**(244): 244ra289.

Park, E. H. and D. M. Durand (2006). "Role of potassium lateral diffusion in non-synaptic epilepsy: a computational study." J Theor Biol **238**(3): 666-682.

Park, S. C., S. K. Lee, H. Che and C. K. Chung (2012). "Ictal high-gamma oscillation (60-99 Hz) in intracranial electroencephalography and postoperative seizure outcome in neocortical epilepsy." Clin Neurophysiol **123**(6): 1100-1110.

Pearce, J. M. (1994). "Robert Bentley Todd (1809-60) and Todd's paralysis." J Neurol Neurosurg Psychiatry **57**(3): 315.

Perucca, P., F. Dubeau and J. Gotman (2014). "Intracranial electroencephalographic seizure-onset patterns: effect of underlying pathology." Brain **137**(Pt 1): 183-196.

Pfeffer, C. K., M. Xue, M. He, Z. J. Huang and M. Scanziani (2013). "Inhibition of inhibition in visual cortex: the logic of connections between molecularly distinct interneurons." Nat Neurosci **16**(8): 1068-1076.

Pinto, D. J., S. L. Patrick, W. C. Huang and B. W. Connors (2005). "Initiation, propagation, and termination of epileptiform activity in rodent neocortex in vitro involve distinct mechanisms." J Neurosci **25**(36): 8131-8140.

Pongracz, F. and M. Szente (1979). "Simulation of the ionic mechanisms of molluscan neurons under pentylenetetrazol-induced effects." Acta Physiol Acad Sci Hung **53**(3): 327-336.

Pouille, F., O. Watkinson, M. Scanziani and A. J. Trevelyan (2013). "The contribution of synaptic location to inhibitory gain control in pyramidal cells." Physiol Rep **1**(5): e00067.

Powell, J. L. (1984). "Least absolute deviations estimation for the censored regression model." Journal of Econometrics **25**(3): 303-325.

Prevett, M. C., J. S. Duncan, T. Jones, D. R. Fish and D. J. Brooks (1995). "Demonstration of thalamic activation during typical absence seizures using H2(15)O and PET." Neurology **45**(7): 1396-1402.

Prince, D. A. (1968). "The depolarization shift in "epileptic" neurons." Exp Neurol **21**(4): 467-485.

Prince, D. A. (1971). "Cortical cellular activities during cyclically occurring inter-ictal epileptiform discharges." Electroencephalogr Clin Neurophysiol **31**(5): 469-484.

Pumain, R., C. Menini, U. Heinemann, J. Louvel and C. Silva-Barrat (1985). "Chemical synaptic transmission is not necessary for epileptic seizures to persist in the baboon Papio papio." Exp Neurol **89**(1): 250-258.

Quiroga, R. Q., Z. Nadasdy and Y. Ben-Shaul (2004). "Unsupervised spike detection and sorting with wavelets and superparamagnetic clustering." Neural Comput **16**(8): 1661-1687.

Raimondo, J. V., R. J. Burman, A. A. Katz and C. J. Akerman (2015). "Ion dynamics during seizures." Front Cell Neurosci **9**: 419.

Ray, S. and J. H. Maunsell (2011). "Different origins of gamma rhythm and high-gamma activity in macaque visual cortex." PLoS Biol **9**(4): e1000610.

Redecker, C., C. Bruehl, G. Hagemann, O. Binus and O. W. Witte (1997). "Coupling of cortical and thalamic metabolism in experimentally induced visual and somatosensory focal epilepsy." Epilepsy Res **27**(2): 127-137.

Reid, I. C. and C. A. Stewart (1997). "Seizures, memory and synaptic plasticity." Seizure **6**(5): 351-359.

Rouiller, E. M. and E. Welker (2000). "A comparative analysis of the morphology of corticothalamic projections in mammals." Brain Res Bull **53**(6): 727-741.

Rousche, P. J. and R. A. Normann (1992). "A method for pneumatically inserting an array of penetrating electrodes into cortical tissue." Ann Biomed Eng **20**(4): 413-422.

Rousseeuw, P. J. and A. M. Leroy (2005). Robust regression and outlier detection, John Wiley & Sons.

Rubino, D., K. A. Robbins and N. G. Hatsopoulos (2006). "Propagating waves mediate information transfer in the motor cortex." Nat Neurosci **9**(12): 1549-1557.

Rutecki, P. A., F. J. Lebeda and D. Johnston (1987). "4-Aminopyridine produces epileptiform activity in hippocampus and enhances synaptic excitation and inhibition." J Neurophysiol **57**(6): 1911-1924.

Ryvlin, P., L. Nashef, S. D. Lhatoo, L. M. Bateman, J. Bird, A. Bleasel, P. Boon, A. Crespel, B. A. Dworetzky, H. Hogenhaven, H. Lerche, L. Maillard, M. P. Malter, C. Marchal, J. M. Murthy, M. Nitsche, E. Pataraia, T. Rabben, S. Rheims, B. Sadzot, A. Schulze-Bonhage, M. Seyal, E. L. So, M. Spitz, A. Szucs, M. Tan, J. X. Tao and T. Tomson (2013). "Incidence and mechanisms of cardiorespiratory arrests in epilepsy monitoring units (MORTEMUS): a retrospective study." Lancet Neurol **12**(10): 966-977.

Sacchetti, B., C. A. Lorenzini, E. Baldi, G. Tassoni and C. Bucherelli (1999). "Auditory thalamus, dorsal hippocampus, basolateral amygdala, and perirhinal cortex role in the consolidation of conditioned freezing to context and to acoustic conditioned stimulus in the rat." J Neurosci **19**(21): 9570-9578.

Scanziani, M. (2000). "GABA spillover activates postsynaptic GABA(B) receptors to control rhythmic hippocampal activity." Neuron **25**(3): 673-681.

Scharfman, H. E. (2002). "Epilepsy as an example of neural plasticity." Neuroscientist **8**(2): 154-173.

Schevon, C. A., R. R. Goodman, G. McKhann, Jr. and R. G. Emerson (2010). "Propagation of epileptiform activity on a submillimeter scale." J Clin Neurophysiol **27**(6): 406-411.

Schevon, C. A., A. J. Trevelyan, C. E. Schroeder, R. R. Goodman, G. McKhann, Jr. and R. G. Emerson (2009). "Spatial characterization of interictal high frequency oscillations in epileptic neocortex." Brain **132**(Pt 11): 3047-3059.

Schevon, C. A., S. A. Weiss, G. McKhann, Jr., R. R. Goodman, R. Yuste, R. G. Emerson and A. J. Trevelyan (2012). "Evidence of an inhibitory restraint of seizure activity in humans." Nat Commun **3**: 1060.

Schiff, S. J., T. Sauer, R. Kumar and S. L. Weinstein (2005). "Neuronal spatiotemporal pattern discrimination: the dynamical evolution of seizures." Neuroimage **28**(4): 1043-1055.

Schindler, K., C. E. Elger and K. Lehnertz (2007). "Increasing synchronization may promote seizure termination: evidence from status epilepticus." Clin Neurophysiol **118**(9): 1955-1968.

Schwartz, O., J. W. Pillow, N. C. Rust and E. P. Simoncelli (2006). "Spike-triggered neural characterization." J Vis **6**(4): 484-507.

Selvitelli, M. F., L. M. Walker, D. L. Schomer and B. S. Chang (2010). "The relationship of interictal epileptiform discharges to clinical epilepsy severity: a study of routine electroencephalograms and review of the literature." J Clin Neurophysiol **27**(2): 87-92.

Sessolo, M., I. Marcon, S. Bovetti, G. Losi, M. Cammarota, G. M. Ratto, T. Fellin and G. Carmignoto (2015). "Parvalbumin-Positive Inhibitory Interneurons Oppose Propagation But Favor Generation of Focal Epileptiform Activity." J Neurosci **35**(26): 9544-9557.

Shimazaki, H. and S. Shinomoto (2010). "Kernel bandwidth optimization in spike rate estimation." J Comput Neurosci **29**(1-2): 171-182.

Singh, N. A., P. Westenskow, C. Charlier, C. Pappas, J. Leslie, J. Dillon, V. E. Anderson, M. C. Sanguinetti, M. F. Leppert and B. P. Consortium (2003). "KCNQ2 and KCNQ3 potassium channel genes in benign familial neonatal convulsions: expansion of the functional and mutation spectrum." Brain **126**(Pt 12): 2726-2737.

Smith, E. H., J. Y. Liou, T. S. Davis, E. M. Merricks, S. S. Kellis, S. A. Weiss, B. Greger, P. A. House, G. M. McKhann Ii, R. R. Goodman, R. G. Emerson, L. M. Bateman, A. J. Trevelyan and C. A. Schevon (2016). "The ictal wavefront is the spatiotemporal source of discharges during spontaneous human seizures." Nat Commun **7**: 11098.

Smith, E. H. and C. A. Schevon (2016). "Toward a Mechanistic Understanding of Epileptic Networks." Curr Neurol Neurosci Rep **16**(11): 97.

Smith, S. J. (2005). "EEG in the diagnosis, classification, and management of patients with epilepsy." J Neurol Neurosurg Psychiatry **76 Suppl 2**: ii2-7.

So, N. K. and W. T. Blume (2010). "The postictal EEG." Epilepsy Behav **19**(2): 121-126.

Soltesz, I. and K. Staley (2011). Computational neuroscience in epilepsy, Academic Press.

Song, S., K. D. Miller and L. F. Abbott (2000). "Competitive Hebbian learning through spike-timing-dependent synaptic plasticity." Nat Neurosci **3**(9): 919-926.

Staley, K. J., A. White and F. E. Dudek (2011). "Interictal spikes: harbingers or causes of epilepsy?" Neurosci Lett **497**(3): 247-250.

Stefan, H., S. Schneider, K. Abraham-Fuchs, J. Bauer, H. Feistel, G. Pawlik, U. Neubauer, G. Rohrlein and W. J. Huk (1990). "Magnetic source localization in focal epilepsy. Multichannel magnetoencephalography correlated with magnetic resonance brain imaging." Brain **113 (Pt 5)**: 1347-1359.

Steinhoff, B. J., J. Scholly, C. Dentel and A. M. Staack (2013). "Is routine electroencephalography (EEG) a useful biomarker for pharmacoresistant epilepsy?" Epilepsia **54 Suppl 2**: 63-66.

Steyn-Ross, M. L., D. A. Steyn-Ross, J. W. Sleigh and D. T. Liley (1999). "Theoretical electroencephalogram stationary spectrum for a white-noise-driven cortex: evidence for a general anesthetic-induced phase transition." Phys Rev E Stat Phys Plasmas Fluids Relat Interdisc Topics **60**(6 Pt B): 7299-7311.

Sutherling, W. W. and D. S. Barth (1989). "Neocortical propagation in temporal lobe spike foci on magnetoencephalography and electroencephalography." Ann Neurol **25**(4): 373-381.

Sutherling, W. W., P. H. Crandall, L. D. Cahan and D. S. Barth (1988). "The magnetic field of epileptic spikes agrees with intracranial localizations in complex partial epilepsy." Neurology **38**(5): 778-786.

Sweeney-Reed, C. M., H. Lee, S. Rampp, T. Zaehle, L. Buentjen, J. Voges, M. Holtkamp, H. Hinrichs, H. J. Heinze and F. C. Schmitt (2016). "Thalamic interictal epileptiform discharges in deep brain stimulated epilepsy patients." J Neurol **263**(10): 2120-2126.

Szente, M. and A. Baranyi (1987). "Mechanism of aminopyridine-induced ictal seizure activity in the cat neocortex." Brain Res **413**(2): 368-373.

Szente, M. and F. Pongracz (1979). "Aminopyridine-induced seizure activity." Electroencephalogr Clin Neurophysiol **46**(5): 605-608.

Toyoizumi, T., M. Kaneko, M. P. Stryker and K. D. Miller (2014). "Modeling the dynamic interaction of Hebbian and homeostatic plasticity." Neuron **84**(2): 497-510.

Tracy, J. I., K. Osipowicz, P. Spechler, A. Sharan, C. Skidmore, G. Doucet and M. R. Sperling (2014). "Functional connectivity evidence of cortico-cortico inhibition in temporal lobe epilepsy." Hum Brain Mapp **35**(1): 353-366.

Traub, R. D. and R. K. Wong (1982). "Cellular mechanism of neuronal synchronization in epilepsy." Science **216**(4547): 745-747.

Trevelyan, A. J. (2009). "The direct relationship between inhibitory currents and local field potentials." J Neurosci **29**(48): 15299-15307.

Trevelyan, A. J., T. Baldeweg, W. van Drongelen, R. Yuste and M. Whittington (2007). "The source of afterdischarge activity in neocortical tonic-clonic epilepsy." J Neurosci **27**(49): 13513-13519.

Trevelyan, A. J., D. Sussillo, B. O. Watson and R. Yuste (2006). "Modular propagation of epileptiform activity: evidence for an inhibitory veto in neocortex." J Neurosci **26**(48): 12447-12455.

Trevelyan, A. J., D. Sussillo and R. Yuste (2007). "Feedforward inhibition contributes to the control of epileptiform propagation speed." J Neurosci **27**(13): 3383-3387.

Tripathy, S. J., J. Savitskaya, S. D. Burton, N. N. Urban and R. C. Gerkin (2014). "NeuroElectro: a window to the world's neuron electrophysiology data." Front Neuroinform **8**: 40.

Truccolo, W., J. A. Donoghue, L. R. Hochberg, E. N. Eskandar, J. R. Madsen, W. S. Anderson, E. N. Brown, E. Halgren and S. S. Cash (2011). "Single-neuron dynamics in human focal epilepsy." Nat Neurosci **14**(5): 635-641.

Tzingounis, A. V. and R. A. Nicoll (2008). "Contribution of KCNQ2 and KCNQ3 to the medium and slow afterhyperpolarization currents." Proc Natl Acad Sci U S A **105**(50): 19974-19979.

Ullah, G., J. R. Cressman, Jr., E. Barreto and S. J. Schiff (2009). "The influence of sodium and potassium dynamics on excitability, seizures, and the stability of persistent states. II. Network and glial dynamics." J Comput Neurosci **26**(2): 171-183.

Ursino, M. and G. E. La Cara (2006). "Travelling waves and EEG patterns during epileptic seizure: analysis with an integrate-and-fire neural network." J Theor Biol **242**(1): 171-187.

Uva, L., L. Librizzi, F. Wendling and M. de Curtis (2005). "Propagation dynamics of epileptiform activity acutely induced by bicuculline in the hippocampal-parahippocampal region of the isolated Guinea pig brain." Epilepsia **46**(12): 1914-1925.

Valentin, A., E. Garcia Navarrete, R. Chelvarajah, C. Torres, M. Navas, L. Vico, N. Torres, J. Pastor, R. Selway, R. G. Sola and G. Alarcon (2013). "Deep brain stimulation of the centromedian thalamic nucleus for the treatment of generalized and frontal epilepsies." Epilepsia **54**(10): 1823-1833.

Vanleer, A. C., J. A. Blanco, J. B. Wagenaar, J. Viventi, D. Contreras and B. Litt (2016). "Millimeter-scale epileptiform spike propagation patterns and their relationship to seizures." J Neural Eng **13**(2): 026015.

Vinck, M., R. Oostenveld, M. van Wingerden, F. Battaglia and C. M. Pennartz (2011). "An improved index of phase-synchronization for electrophysiological data in the presence of volume-conduction, noise and sample-size bias." Neuroimage **55**(4): 1548-1565.

Vitantonio, D., W. Xu, X. Geng, B. S. Wolff, K. Takagaki, G. K. Motamedi and J. Y. Wu (2015). "Emergence of dominant initiation sites for interictal spikes in rat neocortex." J Neurophysiol **114**(6): 3315-3325.

Viventi, J., D. H. Kim, L. Vigeland, E. S. Frechette, J. A. Blanco, Y. S. Kim, A. E. Avrin, V. R. Tiruvadi, S. W. Hwang, A. C. Vanleer, D. F. Wulsin, K. Davis, C. E. Gelber, L. Palmer, J. Van der Spiegel, J. Wu, J. Xiao, Y. Huang, D. Contreras, J. A. Rogers and B. Litt (2011). "Flexible, foldable, actively multiplexed, high-density electrode array for mapping brain activity in vivo." Nat Neurosci **14**(12): 1599-1605.

Vladimirski, B. B., J. Tabak, M. J. O'Donovan and J. Rinzel (2008). "Episodic activity in a heterogeneous excitatory network, from spiking neurons to mean field." J Comput Neurosci **25**(1): 39-63.

Wadman, W. J. and M. J. Gutnick (1993). "Non-uniform propagation of epileptiform discharge in brain slices of rat neocortex." Neuroscience **52**(2): 255-262.

Waziri, A., C. A. Schevon, J. Cappell, R. G. Emerson, G. M. McKhann, 2nd and R. R. Goodman (2009). "Initial surgical experience with a dense cortical microarray in epileptic patients undergoing craniotomy for subdural electrode implantation." Neurosurgery **64**(3): 540-545; discussion 545.

Weiss, S. A., C. Alvarado-Rojas, A. Bragin, E. Behnke, T. Fields, I. Fried, J. Engel, Jr. and R. Staba (2016). "Ictal onset patterns of local field potentials, high frequency oscillations, and unit activity in human mesial temporal lobe epilepsy." Epilepsia **57**(1): 111-121.

Weiss, S. A., G. P. Banks, G. M. McKhann, Jr., R. R. Goodman, R. G. Emerson, A. J. Trevelyan and C. A. Schevon (2013). "Ictal high frequency oscillations distinguish two types of seizure territories in humans." Brain **136**(Pt 12): 3796-3808.

Wendling, F. (2008). "Computational models of epileptic activity: a bridge between observation and pathophysiological interpretation." Expert Rev Neurother **8**(6): 889-896.

White, B. R., A. Q. Bauer, A. Z. Snyder, B. L. Schlaggar, J. M. Lee and J. P. Culver (2011). "Imaging of functional connectivity in the mouse brain." PLoS One **6**(1): e16322.

Wirrell, E. C. (2010). "Prognostic significance of interictal epileptiform discharges in newly diagnosed seizure disorders." J Clin Neurophysiol **27**(4): 239-248.

Wolters, C. and J. C. de Munck (2007). "Volume conduction." Scholarpedia **2**(3): 1738.

Wong, B. Y. and D. A. Prince (1990). "The lateral spread of ictal discharges in neocortical brain slices." Epilepsy Res **7**(1): 29-39.

Wong, M. and P. B. Crino (2012). mTOR and Epileptogenesis in Developmental Brain Malformations. Jasper's Basic Mechanisms of the Epilepsies. J. L. Noebels, M. Avoli, M. A. Rogawski, R. W. Olsen and A. V. Delgado-Escueta. Bethesda (MD).

Worthington, M. (2007). "Diagnoses in Assyrian and Babylonian medicine: ancient sources, translations, and modern medical analyses." Medical History **51**(2): 269-271.

Wyler, A. R. (1982). "Neuronal activity during seizures in monkeys." Exp Neurol **76**(3): 574-585.

Yang, K. H., P. J. Franaszczuk and G. K. Bergey (2005). "Inhibition modifies the effects of slow calcium-activated potassium channels on epileptiform activity in a neuronal network model." Biol Cybern **92**(2): 71-81.

Yoo, J. Y., P. Farooque, W. C. Chen, M. W. Youngblood, H. P. Zaveri, J. L. Gerrard, D. D. Spencer, L. J. Hirsch and H. Blumenfeld (2014). "Ictal spread of medial temporal lobe seizures with and without secondary generalization: an intracranial electroencephalography analysis." Epilepsia **55**(2): 289-295.

York, G. K., 3rd and D. A. Steinberg (2011). "Hughlings Jackson's neurological ideas." Brain **134**(Pt 10): 3106-3113.

Zhang, M., T. P. Ladas, C. Qiu, R. S. Shivacharan, L. E. Gonzalez-Reyes and D. M. Durand (2014). "Propagation of epileptiform activity can be independent of synaptic transmission, gap junctions, or diffusion and is consistent with electrical field transmission." J Neurosci **34**(4): 1409-1419.

Zhao, M., H. Ma, M. Suh and T. H. Schwartz (2009). "Spatiotemporal dynamics of perfusion and oximetry during ictal discharges in the rat neocortex." J Neurosci **29**(9): 2814-2823.

Zhao, M., L. M. McGarry, H. Ma, S. Harris, J. Berwick, R. Yuste and T. H. Schwartz (2015). "Optical triggered seizures using a caged 4-Aminopyridine." Front Neurosci **9**: 25.

Zhao, M., J. Nguyen, H. Ma, N. Nishimura, C. B. Schaffer and T. H. Schwartz (2011). "Preictal and ictal neurovascular and metabolic coupling surrounding a seizure focus." J Neurosci **31**(37): 13292-13300.

Zhu, L., D. Lovinger and E. Delpire (2005). "Cortical neurons lacking KCC2 expression show impaired regulation of intracellular chloride." J Neurophysiol **93**(3): 1557-1568.

Ziburkus, J., J. R. Cressman, E. Barreto and S. J. Schiff (2006). "Interneuron and pyramidal cell interplay during in vitro seizure-like events." J Neurophysiol **95**(6): 3948-3954.